# Time-of-Flight Ion and Electron Spectroscopy: Applications and Challenges at Storage Ring Light Sources

Stråhlman, Christian

2016

# Time–of–flight ion and electron spectroscopy: Applications and challenges at storage ring light sources

Christian Stråhlman

Doctoral Thesis
2016


Lund University

TIME–OF–FLIGHT ION AND ELECTRON SPECTROSCOPY:
APPLICATIONS AND CHALLENGES AT STORAGE RING LIGHT SOURCES



Printed in Sweden by Media-Tryck, Lund, 2016

MAX IV Laboratory, Lund University
P.O. Box 118
SE–221 00 Lund
Sweden

http://www.maxlab.lu.se/

ISBN 978-91-7623-648-2 (PRINT)
ISBN 978-91-7623-649-9 (PDF)

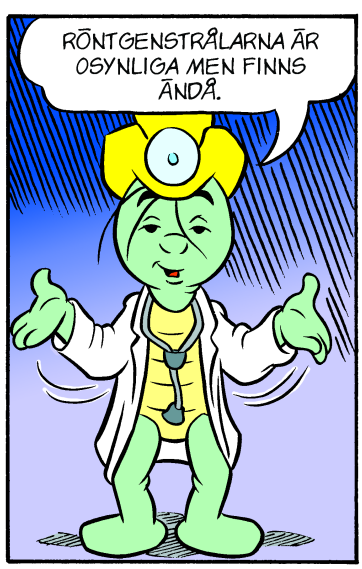


*X-rays are invisible but exist anyway.*
Skalman (from BAMSE, n:o 12/2000)

# CONTENTS

## Papers

# ABSTRACT

This dissertation contains seven studies exploring novel instrumentation for ion and electron spectroscopy, including their applicability at storage ring light sources. The studies focus on instrumentation to study decay, dynamics and dissociation of photoexcited molecules, and the possibility to host such instruments at MAX IV.

Commissioning of an instrument for negative–ion/positive–ion coincidence spectroscopy is reported and its design considerations are discussed. The instrument allows detection of coincidences between mass-resolved negative and (multiple) positive ions, which is demonstrated in a study on the water molecule. Coincidence yields were measured following soft x-ray excitation below and above the O 1s ionization threshold of $H_2O$. Analysis of such yields enhances the present understanding of the dissociation process of the water molecule and allows, for example, designation of previously unchartered doubly excited states and their decay channels. A second study of energy–resolved Auger electrons and mass–resolved positive ions in coincidence provides new data on the non–radiative decay of core–excited and –ionized water molecules.

A study using a novel instrument for mass–resolved analysis of highly excited neutral molecular fragments is reported. Such "high Rydberg" states are associated with electron recapture above the ionization threshold. They can also be reached following resonant Auger decay from core–excited states below threshold. The instrument is utilized in a study on the methane molecule.

The advent of high–resolution, high–transmission time–of–flight electron spectrometers sets new opportunities for spectroscopy at MAX IV, provided that the timing constraints of such instruments can be met. This dissertation proposes, based on initial experimental studies and theoretical considerations, that an ultra–high resolution electron coincidence experimental station could be constructed at MAX IV. This proposed station combines strengths of hemispherical analysers and time–of–flight instruments. The unique time–structure of the MAX IV storage rings with 10 ns light pulse separation allows for better performance than at other laboratories. Recent developments in chopper technology and so called pseudo single

bunch techniques could open up possibilities to run timing–based instrumentation and experiments with high intensity demands in parallel. This dissertation reviews possible adaptations to MAX IV accelerators and beamlines to allow for future inclusion of timing–based spectroscopic instruments.

# POPULÄRVETENSKAPLIG BESKRIVNING

**Slå vatten i småbitar**

Många av de små molekyler som omger oss kan verka helt alldagliga. Vatten, koldioxid, syre, metan; de bara finns där, i våra kroppar, i våra lungor, överallt. Men så börjar någon tala om klimatförändringar, och att förstå de banala molekylerna blir avgörande för hela vår existens. Koldioxid, metan och vatten är växthusgaser, och det finns idag mer av dem i atmosfären än någonsin. Det är när solljuset interagerar med dessa molekyler som vi får global uppvärmning. Samspelet mellan ljus och partiklar i molekylernas lilla värld får stora konsekvenser för hela mänskligheten. Så vet vi allt vi behöver veta om molekylerna?

Människan har alltid behövt förstå vatten. Vatten har studerats vetenskapligt ända sedan antiken, och ändå är det mycket vi inte förstår. Livet börjar i vatten, ändå vet vi inte hur molekylerna sitter ihop. Den mesta koldioxid som vi släpper ut i atmosfären slukas av havet, ändå vet vi inte hur mycket växthusgaser som vatten kan binda. Isen vid polerna räddar jorden från snabb uppvärmning, ändå vet vi inte hur det går till när is fryser.

Detta är frågor som berör hela vår värld. Ska vi rädda jorden från snabba klimatförändringar och förstå livet på jorden så måste vi förstå mer om jordens vanligaste molekyler.

Vattenmolekylen ser enkel ut. Oftast avbildas den som ett stort rött klot med två vita Musse Pigg-öron fastklistrade ovanpå. Den är dock inte enkel. Vattenmolekylen kan sönderdelas i en mängd mindre bitar. Molekylen består av tre atomer, och runt atomkärnorna kretsar tio elektroner. Det är elektronerna som håller ihop molekylen genom så kallad kemisk bindning. Elektronernas värld är kvantmekanisk; den går inte att se med mikroskop. Men det går att flytta runt elektronerna inne i molekylen med hjälp av en ljusstråle. Att flytta en elektron från en elektronbana till en annan kan göra så att hela molekylen faller sönder. Resultatet kan bli en mängd olika partiklar - elektriskt laddade atomer (joner), fria elektroner, ljuspartiklar (fotoner) och elektriskt neutrala atomer. Var och en bär med sig lite information om den vattenmolekyl som de en gång var en del av. Att

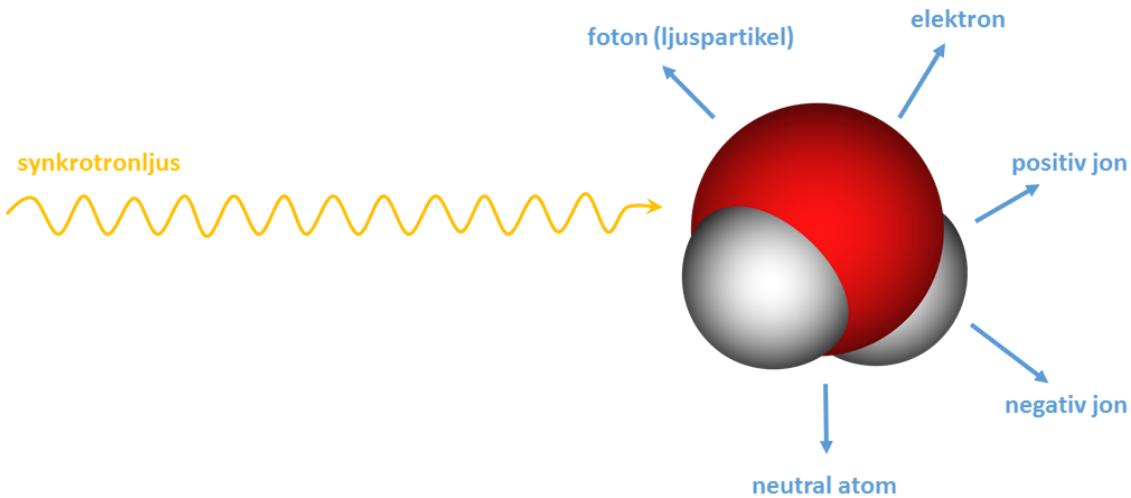


**Figure 1.** *En ljusstråle från en synkrotron – till exempel MAX IV – kan få en vattenmolekyl att falla sönder och skicka ut olika slags partiklar. Att fånga och analysera dessa partiklar är grunden till att förstå molekylens kemi.*

fånga och analysera dessa olika partiklar är därför ett sätt att blicka in i molekylens innersta.

Mitt arbete har varit att bygga mätinstrument för att analysera de olika partiklarna så effektivt som möjligt. Min särskilda utmaning har varit att bygga instrument som kan analysera flera olika partiklar samtidigt, så kallad koincidens. De studier jag gjort kan sammanfattas ungefär såhär: jag använder en stark ljusstråle för att flytta en viss elektron i molekylen från en elektronbana till en annan. När molekylen faller sönder fångar jag upp partiklarna med olika mätinstrument. Ju fler partiklar från samma molekyl, desto bättre resultat. Att fånga flera olika partiklar från samma sönderfall ger oftast en mycket bättre bild av processen än en enstaka partikel. Det är ju lättare för en arkeolog att pussla ihop ett skelett desto fler ben hen har hittat. På samma sätt är det lättare för en fysiker att förstå en molekyl ju fler partiklar hen har fångat.

Utmaningen i att bygga koincidensexperiment är att alla partiklar inte låter sig fångas i samma fälla. Beroende på om partiklarna är lätta eller tunga, positivt eller negativt laddade, reagerar de olika på försöken att styra dem.

Detta faktum använde jag för att bygga ett instrument för att fånga negativa och positiva joner i koincidens. Negativa joner bildas ibland vid molekylsönderfall, men är inte alls lika vanliga som positiva joner. Det går ungefär en negativ jon på tusen positiva. Därför har bildandet av negativa joner inte studerats alls lika mycket. Det är synd eftersom negativa joner produceras i ovanliga sönderfallspro-

cesser som man helt missar om man bara studerar positiva joner. Mitt instrument bestod av ett halvmeterlångt rör med en detektor i varje ände. Mitt i röret lät jag ljusstrålen möta vattenmolekylerna. Med hjälp av en elektrisk spänning drogs alla negativa partiklar in i den ena rörhalvan, medan de positiva drogs in i den andra. Positiva och negativa joner träffade var sin detektor, vilket man kunde registrera i datorn. Om det var träff i båda detektorerna nästan samtidigt så visste jag att ett jonpar hade fångats. Eftersom tunga joner är långsammare än lätta så tar det längre tid för dem att ta sig genom röret fram till detektorn. Om den negativa jonen kommer fram till detektorn innan den positiva jonen når sin detektor så betyder det att den negativa jonen är lätt och den positiva är tung. På så sätt kunde jag få reda på exakt vilka joner som har bildats.

I ett annat experiment ville jag mäta positiva joner i koincidens med elektroner. Elektroner är också negativt laddade, men mycket lättare och snabbare är joner. Då fungerar inte samma teknik som i det första experimentet. Nu måste man istället låta elektronen hitta fram själv till detektorn innan man lägger på den elektriska spänningen och drar ut den positiva jonen. Finessen i detta experiment var att vi kunde mäta elektronens rörelseenergi. Energin är viktig, för den talar om för oss exakt hur mycket av ljusstrålens energi som lämnades kvar i molekylen. Det är den energin som slår sönder molekylen. Det kan berätta inte bara att en jon bildas när man använder ett visst slags ljus, utan exakt hur den bildades. Man kan då se vilka kemiska bindningar som går bra att spräcka, och vilka som är mer robusta.

Ljuset från MAX IV och andra liknande forskningsanläggningar är särskilt lämpligt för dessa experiment. Ljuset är så starkt och så exakt att man kan ”sikta” på en elektron och få den att flytta sig precis till den plats som man vill. Till exempel kan man få den allra innersta elektronen, som är hårt bunden till molekylen, att flytta sig till en ny elektronbana mycket längre ut. Att slå ut en sådan elektron är som att slå ut den understa raden av tegelstenar i en vägg. Den kommer att falla ihop, men kan göra det på ett kontrollerat sätt. Att observerar väggen när den faller avslöjar var dess svaga punkter är. En vattenmolekyl med en utslagen elektron kan falla i bitar på några miljondels miljarddels sekunder. På samma sätt, genom att studera resultatet av sönderfallet kan vi se vilka kemiska bindningar som är molekylens svaga punkter. Man kan också studera exakt vilken energi på ljuset som bryter en viss bindning. Det är genom att styra kemin i detalj på detta sätt som vi har möjligheter att skapa nya intressanta molekyler som kan användas i industrin.

Molekylernas lilla värld är märklig och svår för människan att förstå. Men det är i den lilla världen som hela vår vardagliga stora värld byggs upp. I molekylernas värld vilar svaren några av vår tids stora frågor: klimatförändringar, människors hälsa och förutsättningarna för liv. Det är i det perspektivet som man kan fortsätta slå vatten i småbitar.

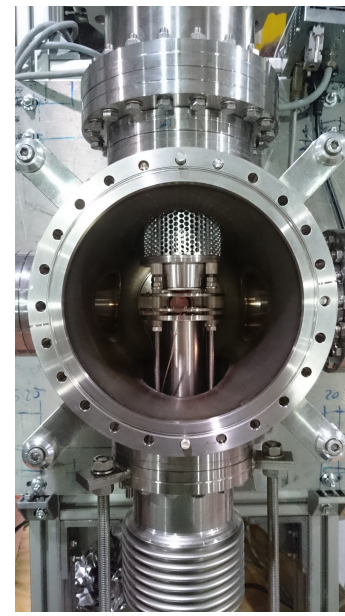

**Figure 2.** *Instrumentet som jag byggde för att mäta negativa och positiva joner i koincidens. Ljuset kommer in från vänster. Precis mitt i instrumentet möter det stråle med vattenmolekyler (ånga) som vi sprutar in genom en nål. Ett elektiskt fält drar negativa joner in i det övre röret och positiva joner in i det nedre. Detektorerna finns i slutet av rören och syns inte på bilden.*

# ACKNOWLEDGMENTS

As a doctoral student at MAX IV and Lund University I have had the opportunity to work with some great people. To those who have helped me, guided me and believed in me, I would like to express my deepest gratitude.

First and foremost, I would like to express my most sincere gratitude to my supervisor Rami Sankari. You have been the best support I could imagine. We have been in this together, and your firm guidance, good advice, deep knowledge and helping hand has been crucial to the success of the projects we have taken on. *Det blev bättre än hundra hare (och ibland var det roligt nästan jämt).* I would also like to thank my assistant supervisor Ralf Nyholm who has supported me and advised me in all stages of this work.

Antti Kivimäki, Robert Richer and Marcello Coreno are acknowledged for their contributions to the NIPICO project. Also, I wish to thank them for welcoming me to Elettra, for their great company during long beamtime shifts, and for sharing their extensive knowledge with me.

El Sayed El Afifi is acknowledged for his substantial contributions to the design of *ChristianTOF* . I want to thank all the people working at the MAX IV mechanical workshop for realizing my ideas into a well working instrument, and also the most beautiful spectrometer I have seen.

My thanks also go to Torsten Leitner, Ruslan Ovsyannikov, Svante Svensson, Nils Mårtensson, Andreas Lindblad, Mihaela Gorgoi and Melanie Mucke who worked with me in the ARTOF gating project. I especially want to thank them for teaching me a lot of practical skills related to beamline instrumentation.

Working with timing at MAX IV has not only been interesting, but also great fun. This is in many regards thanks to my collaborators Teresia Olsson, Stacey Sörensen and Simon Leemann. Thank you for helping me aligning my beamline thinking to the realities of accelerator physics and user needs.

I want to thank Anna Sankari for her many contributions and our good collaboration on PEPICO experiments. We started this already in my Master's Thesis, and I am happy we could complete it together.

I would also like to thank Antti Kettunen and Esko Kokkonen for their kind help during the MAX II beamtime.

The ee-coincidence experiments would not have happened without the equipment and help provided by the Nano and molecular systems group (Nanomo) at the Centre for Molecular Materials Research, University of Oulu, Finland. Marko Huttula, Lauri Hautala, Esko Kokkonen, Ari Mäkinen and Paavo Turunen are gratefully acknowledged. Joakim Laksman and Mihai Pop are acknowledged for their participation in the preparations for the experiments. Uwe Hergenhahn has been a valuable and knowledgeable resource in the discussions leading up to the instrument proposal.

*VG Scienta AB* has kindly provided me with relevant data on the ARTOF lens and figures for this dissertation. Johan Winqvist is acknowledged for his contributions to the graphics.

My PhD studies were funded by the Faculty of Science, Lund University, within the *Max 4 Lund* project. Funding for travels to BESSY was provided by *Ångpanneföreningens forskningsstiftelse*, *Westlings minnesfond*, and *Bokelunds resestipendiefond*. Funding for travels to Elettra was provided by the European Community's Seventh Framework Programme (FP7/2007-2013) under grant agreement n:o 312284, and by the *Royal Physiographic Society of Lund*. I acknowledge Elettra–Sincrotrone for providing beamtime for the NIPICO and high–Rydberg projects (proposal numbers 20135361, 20145053 and 20150229) and MAX IV Laboratory for providing beamtime for the electron/electron coincidence project (proposal number 20140069). The Nanomo group at University of Oulu is acknowledged for allowing electron/ion coincidence experiments to be carried out as part of their beamtime at MAX II.

I have been lucky to have very nice people as fellow doctoral students. First and foremost my colleague and friend Walan Grizolli, with whom I have shared supervisors, offices, successes, drawbacks and many cups of coff(ee) since Day One. Teresia, Jonas, Olivia, Alan, Joel and Galina: You have been good discussion partners and lightened up my days at the lab.

My life and research would not have been the same if I had never met the Student Union. I am very grateful to all the students who entrusted me to represent them in different fora over the course of ten years. It was a great experience, and I hope I served you well.

Lastly, I want to extend my gratitude to my family. *Tack mamma Ellika och pappa Owe för att ni alltid finns när jag behöver er. Tack Staffan och Miriam för att ni hejar på mig och är mina bästaste småsyskon. Tack farmor Marianne och farfar Tage för att ni alltid stödjer mig. Utan er hade denna avhandling inte funnits.*

# LIST OF PUBLICATIONS

The thesis is based on the following papers, which will be referred to by their Roman numerals in the text.

I **A tandem time–of–flight spectrometer for negative–ion/positive–ion coincidence measurements with soft x-ray excitation**
Christian Stråhlman, Rami Sankari, Antti Kivimäki, Robert Richter, Marcello Coreno, Ralf Nyholm.
*Review of Scientific Instruments* **87**, 013109 (2016).

II **Negative–ion/positive–ion coincidence yields of core–excited water**
Christian Stråhlman, Antti Kivimäki, Robert Richter, Rami Sankari.
*manuscript*, in preparation.

III **Non-radiative decay and fragmentation in water after O 1s ionization and O 1s $\rightarrow 4a_1$ excitation studied by electron-energy resolved electron-ion coincidences and ab initio calculations**
Anna Sankari, Christian Stråhlman, J. Antti Kettunen, Rami Sankari, Leena Partanen, Joakim Laksman, Ignacio Fernández Galván, Roland Lindh, Per–Åke Malmqvist, Stacey L. Sörensen.
*manuscript*, in preparation.

IV **Field ionization of high–Rydberg fragments produced after inner–shell photoexcitation and photoionization of the methane molecule**
Antti Kivimäki, Anna Sankari, J. Antti Kettunen, Christian Stråhlman, Jesús Álvarez Ruiz, Robert Richter.
*The Journal of Chemical Physics* **143**, 114305 (2015).

V **Preparing the MAX IV Storage Rings for Timing–based Experiments**
Christian Stråhlman, Teresia Olsson, Simon C. Leemann, Rami Sankari, Stacey L. Sörensen.
*AIP Conference Series* **in press**, (2016).

VI **Using Detector Gating to Operate an ArTOF Time-of-Flight Electron Spectrometer in Hybrid Mode at Storage Ring SR-Facilities**
Torsten Leitner, Christian Stråhlman, Ruslan Ovsyannikov, Patrik Karlsson, Måns Lundqvist, Mihaela Gorgoi, Rami Sankari, Svante Svensson, Nils Mårtensson, Alexander Föhlisch.
*submitted to Journal of Electron Spectroscopy and Related Phenomena*, (2015).

VII **Angle-resolved time-of-fight spectroscopy applied to multi-bunch operation at MAX-lab: a design study**
Christian Stråhlman, Rami Sankari, Måns Lundqvist, Gunnar Öhrwall, Ruslan Ovsyannikov, Svante Svensson, Nils Mårtensson, Ralf Nyholm.
*Journal of Physics: Conference Series* **425**, 092011 (2013).

# ADDITIONAL PUBLICATIONS

In addition to the papers presented in this thesis, the author's doctoral studies resulted in the following publications.

1 **The multielectron character of the S 2p → 4e$_g$ shape resonance in $SF_6$ molecule studied via detection of soft x-ray emission and neutral high-Rydberg fragments**
Antti Kivimäki, Marcello Coreno, Paolo Miotti, Fabio Frassetto, Luca Poletto, Christian Stråhlman, Robert Richter.
*Journal of Electron Spectroscopy and Related Phenomena* **in press**, (2016).

2 **Working together for enhancement-led and voluntary institutional quality audit**
Christian Stråhlman, Bengt–Ove Boström.
*Proceedings of the 8$^{th}$ European Quality Assurance Forum, Gothenburg, Sweden*, (2013).

3 **Student participation in developing student feedback**
Kristina Josefson, Jenny Pobiega, Christian Stråhlman.
*Quality in Higher Education* **17(2)**, 257–262 (2011).

4 **Meeting Report: Workshop on Timing Modes for Low-Emittance Storage Rings**
Stacey L. Sörensen, Teresia Olsson, Christian Stråhlman, Simon C. Leemann.
*Synchrotron Radiation News* **28(5)**, 12–15 (2015).

CHAPTER 1

# INTRODUCTION

On June 21st, 2016, MAX IV will be inaugurated and becomes the brightest storage ring light source in the world. With its two storage rings (Figure 1.1), MAX IV will cover a wide range of photon energies, from ultraviolet to hard x-rays, with outstanding beam properties. The larger 3 GeV ring will have an emittance below 0.3 nm rad, while the smaller 1.5 GeV ring reaches approximately 6 nm rad [1]. The ultra–low emittance of the 3 GeV ring is possible due to several novel features of the accelerator: A multi-bend achromat lattice, very narrow vacuum chambers and damping through harmonic Landau cavities. These accelerator features are aimed at creating very high brilliance light with stable machine operation. All-in-all, MAX IV will be a world–leading research facility for x-ray science in the years to

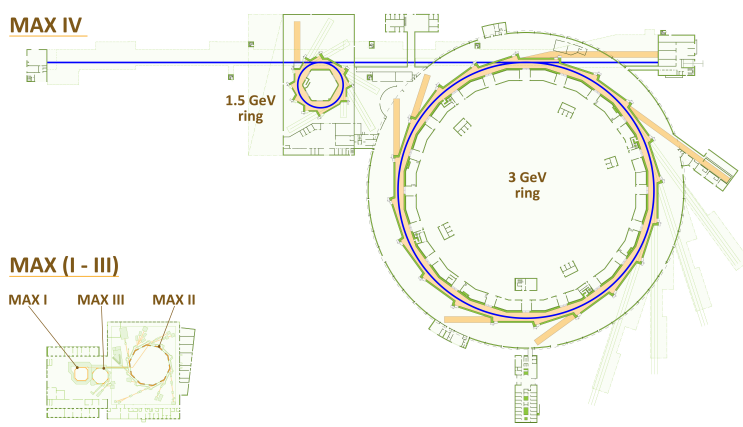


**Figure 1.1.** *The storage rings at the MAX IV Laboratory. The decommissioned MAX I–III rings are drawn for comparison.*

come.

Electron and ion spectroscopy have been a cornerstone of the scientific programme at the MAX Laboratory (MAX–lab) for decades. Photoelectron spectroscopy was one of the first science cases developed for the MAX I storage ring, and many different spectroscopic techniques have thrived at the MAX I, II and III storage rings during their thirty years of operation. MAX–lab has continuously extended and developed its pool of spectroscopic instrumentation, guided by the users' needs and contributions. As the Laboratory now enters into a new era with the MAX IV rings, it is crucial that the world's brightest light source becomes equipped with some high–performance instrumentation to continue into a bright spectroscopic future.

This dissertation contains seven papers that treats spectroscopic instruments, their operational prerequisites and applications. The papers are the result of three (intertwined) research projects that I have pursued since 2011. The first is the design, commissioning and scientific application of a negative–ion time–of–flight spectrometer, *ChristianTOF*, which was developed into a negative–ion/positive–ion coincidence setup. Work with this instrument resulted in Paper **I** which describes the instrument, and Paper **II** where the instrument is used to measure coincidence yields of the water molecule. My participation in Paper **III** and Paper **IV** is associated to the main *ChristianTOF* project. The Auger–electron/positive–ion coincidence study on water originates partly from my Master's thesis [2] where Anna Sankari and I performed the initial experimental and theoretical analysis. The project continued in 2012 and resulted in our joint Paper **III**. The measurements of high–Rydberg fragments from methane in Paper **IV** took place in parallel with work on *ChristianTOF* design.

The second project is studies and preparations for timing–based instrumentation at MAX IV, which resulted in Paper **V** and the studies on high–resolution electron/electron coincidence in Chapter 6. This project has primarily been directed towards collecting user demands for timing, collecting experiences from other facilities and finding viable solutions for MAX IV. It has been a close collaboration between the accelerator, instrumentation and user communities and has resulted in a science case for timing at MAX IV.

Thirdly, Papers **VI** and **VII** concern gating of an ARTOF angle–resolved electron time–of–flight spectrometer. This project was carried out at BESSY between 2011 and 2013. Some parts of this project, especially the use of time–of–flight electron spectrometers, is intertwined with the project on timing–based instrumentation.

The extended summary intends to give a comprehensive background and additional considerations related to the papers. It also seeks to emphasize the connection between them. Chapter 2 gives an overview of molecular spectroscopy at storage rings from the perspective of the water molecule. Chapters 3 treats ion spectro-

scopic instrumentation and contains a detailed description of the *ChristianTOF* instrument in particular. Chapter 4 treats accelerator and beamline instrumentation used to allow for timing–based spectroscopy at storage rings. Chapters 5 and 6 discusses two instrumental solutions to exploit the time–structure of storage rings: ARTOF gating and high–resolution electron–electron coincidence spectroscopy. The final conclusions focus on future possibilities of these projects.

Parts of this dissertation has been published previously in my Licentiate Thesis [3], namely most of Chapters 4 and 5; small parts of Chapters 6 and 7; and Papers **VI** (with minor revisions) and **VII**.

CHAPTER 2

# DECAY, DYNAMICS AND DISSOCIATION OF PHOTOEXCITED MOLECULES

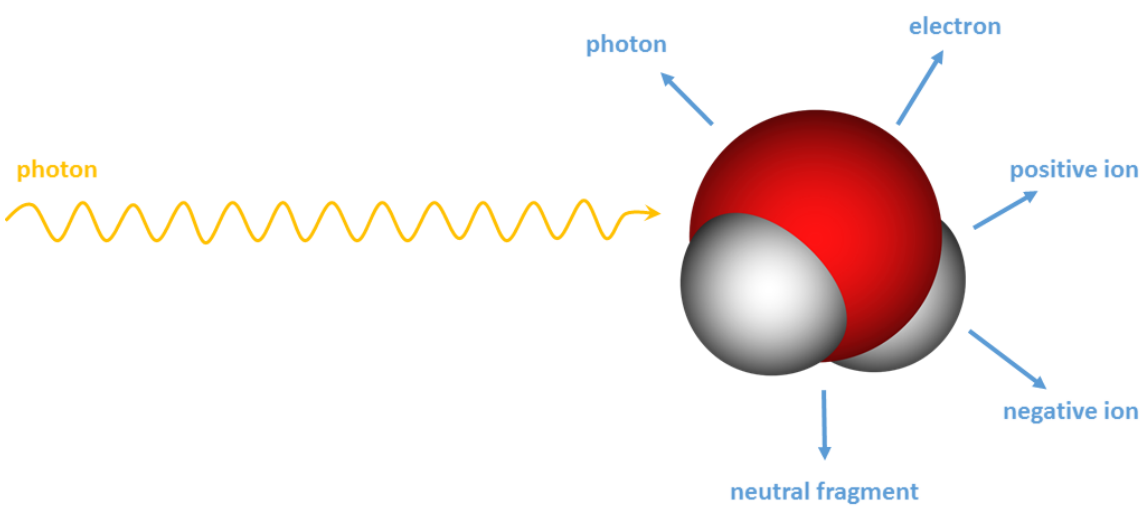


**Figure 2.1.** *Photoexcitation of the water molecule with possible decay and dissociation products.*

Photoinduced electronic transitions provide a wealth of information on the structure and dynamics of molecules. This wealth is extracted by spectroscopic techniques. The general understanding of molecules have increased by the development of spectroscopies designed to monitor outcomes of the excitation, decay and fragmentation of the molecule. A number of particles can be created when a light beam interacts with the sample; each carrying some information about its own origin. The relevant information can be its kinetic

energy, direction of movement, mass, charge, or other property that is an indicator for some aspect of the molecule under study.

In this chapter, I want to describe how proper analysis of these properties can be used to understand the physics of molecules better. I will also make the case that coincidence studies, i.e. detection and analysis of more than one particle simultaneously, further enhances understanding of the physics involved. I have chosen to build this chapter around the water molecule ($H_2O$) with references that exemplify the merits of different spectroscopic techniques. The water molecule features in Papers **II** and **III**. It should be stressed that these molecular properties are general and can be applied to other samples with good results.

The scientific study of water has deep historical roots. When the natural philosophers of ancient Greece, more than two millennia ago, named water one of the four classical elements; fundamental and indivisible; they must have appreciated the curious properties of this remarkable element. What they could not have appreciated fully is its chemical complexity, which stands out from its apparent triatomic simplicity. Water in its ground state carries 10 electrons and has $C_{2v}$ symmetry. The electronic configuration can be written

$$1a_1^2\,2a_1^2\,1b_2^2\,3a_1^2\,1b_1^2\;{}^1\mathrm{A}_1.$$

The $1a_1$ orbital is identified as the O 1s core orbital, $2a_1$ has mostly O $2s$ character, and the non-bonding $1b_1$ is associated with the O $2p_x$ atomic orbital [4]. Unoccupied molecular orbitals are $4a_1$ (LUMO), $2b_2$, $2b_1$; in addition there are so called Rydberg orbitals. Its ground state bond length is 0.958 Å and bond angle is 104.4°[5].

## 2.1 Excitation and identification of electronic states

Photons from various regions of the electromagnetic spectrum interact with molecules in different ways. Starting from the lowest energy photons there are the radiofrequency region (wavelength: 10 m–1 cm) for nuclear magnetic resonance and electron spin resonance, the microwave region (1 cm–100 $\mu$m ) for rotational transitions, the infra-red (IR, 100 $\mu$m –1 $\mu$m ) for vibrational transitions, the visible and ultraviolet (UV, 1$\mu$m –10 nm) for electronic transitions in valence orbitals, x-rays (10 nm–100 pm) for inner electron transitions, and $\gamma$-rays for redistribution of nuclear particles [6, p. 5f]. Storage ring light sources mostly operate in the UV and x-ray region where electronic transitions dominate, with vibrational transitions as an important fine–structure; the following discussion will focus on those regions.

The interaction of light with the water molecule is a quantum mechanical process. Essentially, a beam of photons (UV or x-ray) can interact with the sample by scattering or absorption. Scattering will not be treated here. The absorption of a photon induces transitions, which from a quantum mechanical point of view is the change of the

molecule system from one eigenstate to another. From a spectroscopic point of view, these transitions introduce additional dynamics to the system that can be measured by means of absorption and emission spectroscopy. Spectroscopic investigation relies primarily on energy conservation and mass conservation.

Photoexcitation takes place when an electron is promoted from one molecular orbital to another. An initially electrically neutral molecule has a neutral final state. In contrast, if the photon energy is sufficient to promote the electron to a continuum level, the molecule becomes ionized and the resulting ion has a single positive charge.

The first task of molecular spectroscopy is to identify and quantify electronic states of the molecule. It is understood that electrons reside in orbitals with different symmetry and binding energy. Also unoccupied orbitals, which electrons can be promoted to, have binding energies. A direct probe of occupied orbitals is photoelectron spectroscopy, which provides information on the electronic states themselves. The photoelectric effect, first described by Einstein in 1905 [7], says that a photon energy quantum $h\nu$ can ionize a molecule if its energy exceeds an electron's binding energy $U_B$. Energy conservation dictates that the kinetic energy of the emitted electron, $U_{\text{kin}}$, must be $U_{\text{kin}} = h\nu - U_B$. The energy of the photoelectron thus becomes a probe of the binding energy of the orbitals. Brundle and Turner [8] measured the photoelectron spectrum of water by using UV (584 Å; 21.2 eV), and they determined the adiabatic ionization potentials[1] of the three highest orbitals (12.6 eV, 13.7 eV and 17.2 eV) of water. The UV photoemission spectrum (UPS) shows prominent vibrational fine–structure which belongs to the resulting singly charged ion[2]. An x-ray photoemission spectrum gives the binding energy of the O 1s core electron (539.9 eV) [9]. Also the O 1s photoelectron line has vibrational fine-structure [10], but less pronounced due to the large linewidth.

Direct probing of unoccupied states can be performed with absorption spectroscopy, in particular X-ray absorption near edge structure spectroscopy (XANES). The absorption of a beam by the sample can be determined by measuring the intensity of the beam before and after it passes through it. The absorption probability increases at resonances when the transition energy equals the photon energy. Close to the ionization potential, i.e. at photon energies similar to the O 1s electron binding energy, absorption maxima are reached when the photon energy correspond to the promotion of an electron from the O 1s orbital to the unoccupied orbitals O 1s$\rightarrow 4a_1$, $2b_2$, $2b_1$, or to the Rydberg orbitals. Unoccupied states can be mapped by scanning the photon energy over a wide photon energy range [11].

[1] The minimum energy required to remove the electron.

[2] Vibrational spectroscopy with microwaves give the fine-structure for the neutral molecule.

The XANES study by Myneni *et al.* [11] is also illustrative for the power of absorption spectroscopy to probe changes in unoccupied states as molecular bonds are altered. They measured absorption for all aggregation states of water (vapour, liquid and ice) and deduced features of the local geometry of the hydrogen bond network. The structure and dynamics of solid [12, 13] and liquid water [14, 15] is still a mystery, and still more research attention could go into exploring it. It has not been possible to adequately describe the properties of liquid water, and recent research suggest that its structure is strongly temperature dependent [15]. For ice, one of the many remaining questions is how the freezing process takes place.

So far, the picture has been one photon acting on one electron to form an excited or ionized state. Double excitations, where two electrons are promoted by one photon has been observed in water for photon energies just above the ionization threshold [16]. In Paper **II** we show that doubly excited states contribute to the negative ion production. The x-ray photoemission spectrum shows so called shake–up satellites at binding energies close above the main photoline [17]. These states arise when valence electrons are promoted from one orbital to another as a secondary result of the promotion of the core electron from the O 1s orbital to the continuum state. The shake–up lines thereby carries information about the redistribution of orbitals in the resulting ion. Even more exotic one–photon—two–electron processes exist. Mucke *et al.* [18] has observed the creation of a double core hole $H_2O$ (O $1s^{-2}$) state from a single photon at 1300 eV energy by measuring the subsequently emitted electrons in coincidence.

## 2.2 Decay

Highly excited molecules will eventually decay by electron or photon emission. The core excited $H_2O$ (O $1s^{-1}\,virt^1$) or core–ionized $H_2O$ (O $1s^{-1}$) molecule[3] predominately decays by electron emission, so called Auger decay. The normal Auger spectrum, i.e. electrons emitted from core–ionized water, was measured by Siegbahn, Asplund, and Kelfve [19]. The energy of the emitted electron is determined by (i) which electron was removed by photoemission, (ii) which electron took its place, and (iii) which electron was emitted as a result. Normal Auger decay leaves the molecule in a doubly charged and possibly excited state $H_2O^{2+}$ ($val_1^{-1}\,val_2^{-1}$). The Auger electron kinetic energy equals the energy difference between the core–ionized state and the resulting doubly charged state[4]. Resonant Auger de-

[3] "val" denotes a valence orbital and "virt" a virtual (unoccupied in the ground state) orbital. Orbitals with subscript (e.g. $val_1$, $val_2$) can be identical unless otherwise stated.

[4] More precisely, the sum of the Auger electron energy and the photoelectron energy equals the photon energy minus the energy difference between the doubly charged state and the ground state, which will be important in Chapter 6.

cay [20, 21] involves a core–excited $H_2O$ (O $1s^{-1}$ $virt^1$) state, which eventually decays and emits a resonant Auger electron. One can distinguish between participator decay, where the initially promoted electron is emitted and creates a $H_2O^+$ ($val^{-1}$) state, and spectator decay, where another valence electron is emitted and creates a $H_2O^+$ ($val_1^{-1}$ $val_2^{-1}$ $virt^1$) state. Shake-up and shake-down processes can contribute to the final result. Spectator decay, and its subsequent dissociation, is treated in Paper **III**.

Radiative decay, i.e. emission of a fluorescence photon, is a minority decay channel. Both non-resonant [22, 23] and resonant [23, 24] x-ray emission has been recorded. X-ray emission probes transitions between electronic states where the charge of the molecule is not changed. The final state of a non-resonant x-ray emission is a singly charged molecule with a valence hole. X-ray emission in the resonant case has been shown to lead mainly to $H_2O$ ($val^{-1}$ $virt^1$) states, so called spectator emission [24].

The photoelectron and/or Auger line shape can also be distorted by so called post-collision interaction (PCI) where the (fast) Auger electron interacts with the emitted (slow) photoelectron. PCI effects are visible in the O 1s photoelectron spectrum [10]. The extreme case for PCI is the complete recapture of the photoelectron by the Auger-emitting molecule. It has been observed that such processes takes place in water, where the photoelectron is captured into a high–Rydberg (HR) orbital [25]. The recapture probability falls exponentially above threshold [26]. Recapture is a prominent phenomenon in the study on HR fragments (of methane) in Paper **IV**, where we observed a large increase of HR fragments just above threshold. The HR states created from recapture can also be created from shake–up processes [27]. Recapture is thought to contribute the the production of $O^-$ fragments just above threshold, as observed in Paper **II**.

## 2.3 Dissociation

Dissociation and fragmentation of the water molecule has been extensively studied, both theoretically and experimentally. Partial positive ion yields [28] and negative ion yields [29] have been measured in the valence region. Similarly, partial positive [30] and negative ion yields [31] was measured close to the O 1s ionization threshold. The direct detection of ionic fragments is a gauge of the bond breaking processes. It is clear from studies that fragmentation is strongly dependent on the photoexcited state. Potential surfaces along which the dissociation takes place change bond lengths and the bond angle from the ground state [32]. While it is possible to extract a lot of information on the bonding from pure fragment detection, it must be recognized that the interplay between decay and dissociation, even for a simple molecule, is complicated and different processes are competing. Still the number of possible outcomes of fragmentation is lim-

ited. Combination principles gives at hand that only five fragments – $H_2O$, OH, O, $H_2$ and H – can be created. Electronic state configurations and decay of the oxygen and hydrogen atom has been studied extensively by the atomic spectroscopy community. This is beneficial since it is expected that fragments can be formed in excited states which subsequently decays and emits an electron or photon. The detection and identification of such emission indirectly identify the fragment species.

For core excited species, dissociation and electronic Auger decay can compete on a femtosecond time–scale. Vibrational fine–structure in the resonant Auger spectrum has revealed so called ultra–fast dissociation both of the $H_2O$ (O $1s^{-1}\,4a_1^1$) state and a doubly excited state $H_2O$ (O $1s^{-1}$ $val^{-1}$ $virt_1^1$ $virt_2^1$) at 550 eV photon energy (above threshold) [5, 33]. Features related to the fragmentation was deduced from the electron spectrum, where Auger electrons that could only be emitted by a neutral OH fragment was observed. Therefore, the dissociation must precede the Auger emission. The energy of these electrons could also reveal the final state of the decaying OH fragment.

Fluorescence emission has been employed to distinguish between different excited fragments. Wavelength–resolved photons in the Balmer and Lyman series can identify excited H species [34]. By measuring the photon yield for a range of photon energies in the valence region, they could identify dissociative doubly excited states and chart the rearrangement of electrons at dissociation. Similar techniques have been used to identify core–hole double excitations $H_2O$ (O $1s^{-1}$ $val^{-1}$ $virt_1^1$ $virt_2^1$) [16]. The technique is not limited to hydrogen species. Rather, signature emission lines can be identified for several fragments, including ionic species [35].

Fragmentation studies such as that by Laksman *et al.* [36] highlights the quite rapid rearrangement that can precede dissociation. The most obvious example is the emergence of a $H_2^+$ fragment from core–excited species (also observed in Refs. [30, 31]) which signifies a narrowing of the H–O–H bond angle and subsequent ion pair formation. The study also shows clearly the large kinetic energy releases involved in fragmentation of core–excited species, especially dissociation of doubly ionized water molecules. Kinetic energy release can signify that the exited states are on strongly dissociative potential surfaces. Such dissociation paths are treated in Paper **III**, where also calculations are provided.

Neutral fragments can be directly measured if they are produced with sufficent kinetic energies to be read by a MCP detector, or when they can be field–ionized, see Ref. [26] and Paper **IV**. The latter case has one electron placed in a HR orbital and results in a long-lived, metastable state. Such states can remain excited even following dissociation. For water, these states have been identified and measured both for the H fragment by means of direct detection [26] and the O fragment by means of electron auto–ionization [25, 27]. That HR

electrons remain apparently unaffected by dissociation is a possible mechanism for anion formation, since it is expected that both ionic and neutral fragments can capture a HR electron [27]. This observation mandates a close examination of the negative–ion yields close to the O 1s threshold in Paper **II**.

## 2.4 Coincidence

The reader should now appreciate that the several decay and dissociation processes in the water molecule can be monitored by a multitude of possible particle emissions and fragmentations. Processes that are not distinguishable with one technique can be readily measured with another. In addition, most processes will result in more than one fragment and/or emission. For example, positive ions are accompanied by electrons, negative ions are always accompanied by positive ions, photons are often accompanied by both electrons and ions, and so on. This observation suggests the use of coincidence measurements to gain additional information about the water molecule.[5]

**Electron/electron coincidence** comes in several flavours. A study on the *oxygen molecule* by Arion *et al.* [38] illustrates the added benefit of coincident detection for separation of contributions in the Auger spectrum from different core–ionized states. Auger spectra have mostly broad overlapping features which could be separated into components by means of coincident detection with photoelectrons. If the resolution of the instrumentation is sufficient, sub-natural linewidths can even be achieved. This topic is further discussed in Chapter 6. Coincidences between two electrons can also be employed in double valence ionization, where the ionization energy is distributed among two electrons. Collecting both electrons from the process can chart the ionization processes with higher reliability than non-coincident spectroscopy [39]. Energy–resolved coincidence detection of Auger electrons and photoelectrons allowed Mucke *et al.* [18] to record the double Auger decay spectrum and find, among other things, the energy of the double core–hole state of the water molecule.

**Electron/ion coincidence** is intuitively straightforward for positive ions since the ionization process always creates these two constituents. The coincident detection of an electron together with an ion can be simply a spectroscopic aid for measuring partial ion yields [28]. However, coincident detection of energy-resolved electrons with mass-resolved ions can disentangle relationships between fragmentation paths and decay

[5] The different flavours of coincidence spectroscopy has recently been reviewed by Arion and Hergenhahn [37].

channels. In Paper **III** this technique is used to assign fragmentation paths to resonant and normal Auger emission channels. The energy of the electron gives information about the final state of the Auger decay, from which the fragmentation path can be elucidated. It is possible to gauge the competing ultrafast dissociation channel and fast Auger decay in the $H_2O$ (O $1s^{-1}\,4a_1^1$) state.

Electron/negative-ion coincidence studies are not conceptually different, and could be performed using the same principles as outlined in Paper **III**. Such studies would likewise show relationships between anionic fragmentation paths and decay channels. However, it is technically much more complicated. This idea has been considered in this thesis which will be discussed in Chapter 3 and Chapter 7.

**Ion/ion coincidence** involves the detection of all ions (or a subset thereof) created in an ionization and fragmentation process. Piancastelli *et al.* [30] measured positive–ion/positive–ion coincidences close to the O 1s ionization threshold. Their study charted fragmentation pathways which would not be visible in single-ion yields. In particular, comparisons between coincident and non-coincident yields are a gauge for neutral particle emission. The coincidence yields are also a good indicator for secondary effects, such as PCI, close to the O 1s threshold.

In Paper **II** we study the negative–ion/positive–ion coincidence from core–excited water. Non–coincident negative–ion yields had been measured by Stolte *et al.* [31]. Compared to their measurement, we were able to assign fragmentation pathways involving several ions and chart the neutral particle contribution to the three-body breakup. This is particularly relevant for negative–ion production, since neutral fragments can be an indirect gauge for fluorescent decay. We were able to show that fluorescence contributes to the negative–ion yield above the O 1s IP for water. The results also hints towards radiative contribution below threshold, which however could not be conclusively determined. We identified an unknown doubly excited state above threshold.

**Positive–ion/neutral coincidence** is not a common technique, but has been employed for a few studies. For the water molecule, the study of Harries *et al.* [26] is illustrative. H(HR) fragments[6] were detected after core-excitation in coincidence with mass-resolved positive ions. While the H(HR) non–coincident yields had been measured in the same paper, the coincidence detection allowed them to attribute them (broadly) to different fragmentation channels.

[6] H(HR) denotes a hydrogen atom in a high–Rydberg state.

**Photon/ion coincidence** resembles the Auger–electron/positive–ion coincidence in that it becomes possible to assign fragmentation pathways to final states of decay. Photon/negative-ion coincidence studies are not conceptually different. This opportunity is intriguing since, as outlined in Paper **II**, the negative-ion production at the core–resonances in water hints towards a contribution from fluorescent decay. X-ray-photon/negative-ion coincidence can verify this assumption and quantify it. This opportunity will be discussed in Chapter 7.

CHAPTER 3

# INSTRUMENTATION FOR TIME–OF–FLIGHT BASED ION SPECTROSCOPY

This chapter provides background on the design of the time–of–flight ion spectrometers used in Papers **I**–**IV**. These spectrometers abide by the same design principles as was described by Wiley and McLaren more than 60 years ago [40]. Particular emphasis will be on the design of the negative–ion spectrometer – *ChristianTOF* – presented in Paper **I**. The design considerations will be applied to the electron–ion coincidence instrument (Paper **III**) and the instrument for field–ionization of high–Rydberg fragments (Paper **IV**).

## 3.1 Principles of ion time–of–flight mass spectrometry

The prime objective for ion time–of–flight (TOF) mass spectroscopy is to determine an ion's mass–to–charge ratio ($m/q$, where $m$ is the mass and $q$ is the charge[1]). The ion TOF spectrometer achieves this goal by temporal dispersion of particles by means of accelerating electric fields. A particle with a kinetic energy $U$ will, according to Newtonian physics, have a speed $v$ which is inversely proportional to the square root of its mass; $v \propto 1/\sqrt{m}$. Consider a particle carrying a charge $q$ which has been brought from rest by an accelerating electric field $E$. The force $F$ acting on the particle is $F = qE$, which gives an acceleration $a = qE/m$ and a resulting kinetic energy $U = qEd$ where $d$ is the distance over which the particle has been accelerated. If the particle subsequently enters a field–free region, its speed $v = \sqrt{2U/m} = \sqrt{2qEd/m}$ will be inversely proportional to the square root of its mass–to–charge ratio $v \propto 1/\sqrt{m/q}$.

[1] For simplicity, the mass is most often given in atomic mass units (u) and the charge in units of the elementary charge ($e$). In these units, an ion's mass–to–charge ratio can be approximated with a rational number.

The time spent in drift becomes $t_D = D/v$, with $D$ denoting the distance the particle has to travel in the field–free region. In the acceleration region, where the particle is accelerated by the uniform electric field, the speed becomes $v = \int qE/m\,\mathrm{d}t = v_0 + (qE/m)t$. Considering that the particle starts from rest, and applying kinematic rules, the time–of–flight is given by $d = (qE/m)t^2/2$. This shows that observed flight times are proportional to the square root of the mass–to–charge ratio both in field-free regions and in regions were a uniform electric field is applied. It implies that one can make a temporally $m/q$–dispersing instrument by means of such fields, and that the flight times of such an instrument would disperse according to $t \propto \sqrt{m/q}$.

If all ions were created in one single point with zero initial velocity, the temporal resolution would only be limited by the timing of the instrument, i.e. the precision by which one can determine the time of ionization and that of the detector. Realistic ion production will always have a spatial distribution and a kinetic energy distribution [40]. In most experiments described in this dissertation, ions are created when molecules are ionized by a light beam. The light beam from a storage ring has a (small) finite size defining the ions' spatial spread. Molecules also have natural kinetic energies, determined by the Boltzmann distribution. Ionization and dissociation of molecules can initiate substantial kinetic energy releases that introduces a time–spread of ions with identical $m/q$. It is necessary for the instrument to reduce both of these contributions to achieve high resolution.

The theory behind a space and energy focusing TOF spectrometer was laid out by Wiley and McLaren in 1955 [40]. They proposed an electrostatic instrument with three regions separated by transmission meshes; a source region[2] with a uniform electric field ($E_s$), a short acceleration region (length $d$) with a stronger uniform field ($E_d$), and a field–free drift region (length $D$). It was later shown that this two–field spectrometer design is the theoretical optimum for a time–independent electrostatic TOF [41]. The total flight time $t(U_0, s)$, where $U_0$ is the initial kinetic energy and $s$ is the initial position of the particle along the spectrometer axis measured as the distance from extractor mesh, is

$$t(U_0, s) = t_s + t_d + t_D \tag{3.1}$$

$$t_s = \frac{\sqrt{2m}}{qE_s}\left(\sqrt{U_0 + qsE_s} \pm \sqrt{U_0}\right) \tag{3.2}$$

$$t_d = \frac{\sqrt{2m}}{qE_d}\left(\sqrt{U_0 + qsE_s + qdE_d} + \sqrt{U_0 + qsE_s}\right) \tag{3.3}$$

$$t_D = \frac{\sqrt{2m}D}{2\sqrt{U_0 + qsE_s + qdE_d}} \tag{3.4}$$

[2] The source region is termed "ionization region" in their paper.

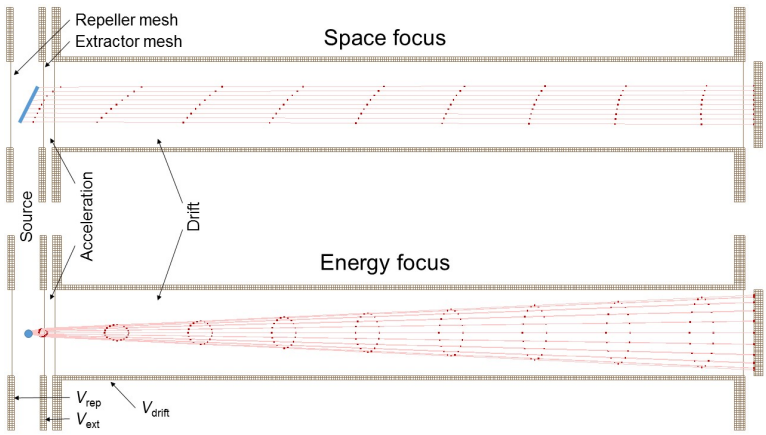


**Figure 3.1.** *The effect of space and energy focusing in a Wiley–McLaren TOF instrument. In the space focus figure, ions are flown from different positions $s$ starting from rest, and are temporally focused to the detector. The energy focus figure depicts ions originating from one point with identical kinetic energies but different directions. Those ions with directions away from the detector arrive late. Ions with directions perpendicular to the spectrometer axis arrive at mean flight times, but at the outer rim of the detector.*

where the ± in equation (3.2) denotes particles with velocities directed towards and away from the detector [40]. $E$–fields are not very practical to work with directly. Rather, potentials are supplied to repeller ($V_{\mathrm{rep}}$) and extractor meshes ($V_{\mathrm{ext}}$), and drift tube ($V_{\mathrm{drift}}$). The instrument is constructed so that the interaction point at distance $s = s_0$ is centred in the source region, and $V_{\mathrm{ext}} = -V_{\mathrm{rep}} = s_0 E_s$. The source point is at zero potential. It is convenient to substitute $V_{\mathrm{ext}} = s_0 E_s$, $V_{\mathrm{drift}} = s_0 E_s + d\,E_d$ and $s = s_0 + \delta s$, which renders the flight time

$$t(U_0, \delta s) = t_s + t_d + t_D \tag{3.5}$$

$$t_s = \frac{\sqrt{2m}\,s_0}{q\,V_{\mathrm{ext}}}\left(\sqrt{U_0 + q\,V_{\mathrm{ext}} \pm \delta U_s} \pm \sqrt{U_0}\right) \tag{3.6}$$

$$t_d = \frac{\sqrt{2m}\,d}{q(V_{\mathrm{drift}} - V_{\mathrm{ext}})}\left(\sqrt{U_0 + q\,V_{\mathrm{drift}} \pm \delta U_s} + \sqrt{U_0 + q\,V_{\mathrm{ext}} \pm \delta U_s}\right) \tag{3.7}$$

$$t_D = \frac{\sqrt{2m}\,D}{2\sqrt{U_0 + q\,V_{\mathrm{drift}} \pm \delta U_s}} \tag{3.8}$$

where $\delta U_s = q\,V_{\mathrm{ext}}\frac{\delta s}{s_0}$ is the small deviation in the ions' initial potential energy introduced by the size of the ion source[3].

[3] It is usually practical to measure particle kinetic energies in eV, masses in atomic mass units, charges in units of the elementary charge, potentials in V and lengths in

To find the space focus condition the dependence on initial position $\delta s$ on the flight time should be minimized. We consider the situation where ions have no initial kinetic energy ($U_0 = 0$) and solve for $\frac{\mathrm{d}t}{\mathrm{d}(\delta s)}|_{\delta s=0} = 0$. It follows that this condition is fulfilled when

$$D = 2s_0 k_0^{3/2}\left(1 - \frac{1}{k_0 + \sqrt{k_0}}\frac{d}{s_0}\right) \tag{3.9}$$

where $k_0 = V_{\mathrm{drift}}/V_{\mathrm{ext}}$. This equation is known as the *Wiley–McLaren condition* [40]. If the lengths $s_0$, $d$ and $D$ are fixed, the ratio $k_0$ is uniquely determined. The resolution $M$ can be defined as the largest $m/q$ that can be completely separated from the adjacent $m/q + 1$. Then it follows that the space–related mass resolution is

$$M_s \approx 16k_0(s_0/\delta s)^2, \tag{3.10}$$

provided that $k_0 \gg 1$ and $k_0 \gg d/s_0$ [40].

Time spread due to initial kinetic energy arises because ions with velocities directed away from the detector will have longer flight times than those directed towards it. The ± in equation (3.2) shows two extreme cases where the difference in flight time is

$$\Delta t_s = \frac{2\sqrt{2mU_0}\cdot s_0}{qV_{\mathrm{ext}}} \tag{3.11}$$

which yields energy–related mass resolution [40]

$$M_U = \frac{1}{4}\sqrt{\frac{qV_{\mathrm{drift}}}{U_0}}\left(\frac{k_0+1}{\sqrt{k_0}} - \frac{\sqrt{k_0}-1}{k_0+\sqrt{k_0}}\frac{d}{s_0}\right) \tag{3.12}$$

The relative contributions of space and energy focusing differ between different instruments. To optimize the design of the instrument it is important to have a general idea of the size of the source ($\delta s$) and expected kinetic energies ($U_0$). The choice of parameters for an instrument design is in practice also limited by other factors, such as the total length of the instrument, the highest potentials that can be used, the size of the detector and the need to have enough room in the source region to insert the sample.

The TOF principles formulated in this section create the foundation for the three TOF based instrumental applications in Papers **I–IV**. In the following sections, these principles will be referred to in order to justify design features and assess the performance of the instruments.

## 3.2 Design of a negative–ion time–of–flight spectrometer – *ChristianTOF*

The negative–ion TOF spectrometer – *ChristianTOF* – is a mass–resolving negative–ion spectrometer aimed for use in two kinds of

mm. Using these units, equation (3.5) should be multiplied by 144 to give the flight time in ns.

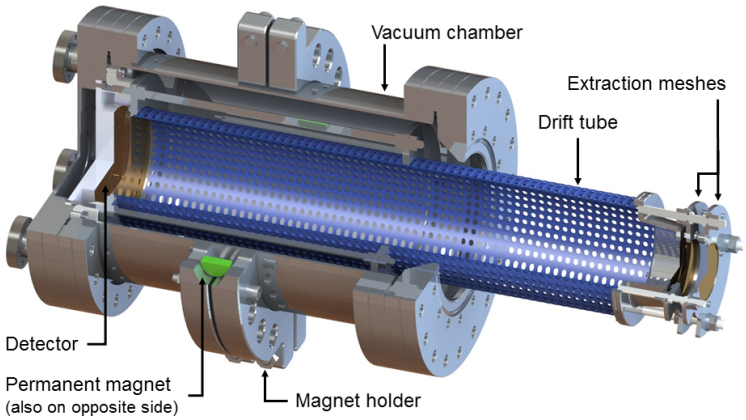


**Figure 3.2.** *Drawing of the negative–ion spectrometer in its stand-alone configuration with a separate interaction region. The different parts and design considerations are discussed in the text.*

coincidence studies; with positive ions and electrons. The stand-alone design, as it was assembled in early 2015, is depicted in Figure 3.2. The design and performance of the instrument in a negative–ion/positive–ion coincidence setup (see Figure 3.3) is the topic of Paper **I**. The instrument is also used in Paper **II**.

### 3.2.1 Design values and dimensions

The principle design constraints were that *ChristianTOF* should be operational together with two existing spectrometers:

The positive–ion spectrometer – *RamiTOF* – belongs to the Gas-phase beamline at Elettra Sincrotrone, Italy, and is in regular use for photoelectron/positive–ion coincidence (PEPICO[4]) studies [42]. This instrument has a $D = 319$ mm long and $W = 40$ mm wide stainless steel drift tube, preceded by two mesh holders. The size of the acceleration region ($d = 5$ mm) and source region ($2s_0 = 15$ mm) is defined by the design and cannot be changed. The parts are mounted on four steel rods, which are fixed to a CF 100 flange. The flange is mounted on a large (∼200 mm long) bellow which can be mounted on a CF 100 opening on the vacuum chamber. The bellow assures that the position of the source region along the spectrometer axis can be adjusted from outside vacuum. The two spectrometers should be mounted in an existing vacuum chamber with two CF 100 openings.

[4]PEPICO is used in the literature as an acronym for photoelectron/photoion coincidence. In this dissertation, PI should always be read as "positive ion", NI as "negative ion" and PE as "photoelectron". Since I am not aware of any studies where PEPICO has involved negative–ion analysis, the risk for confusion should be very low.

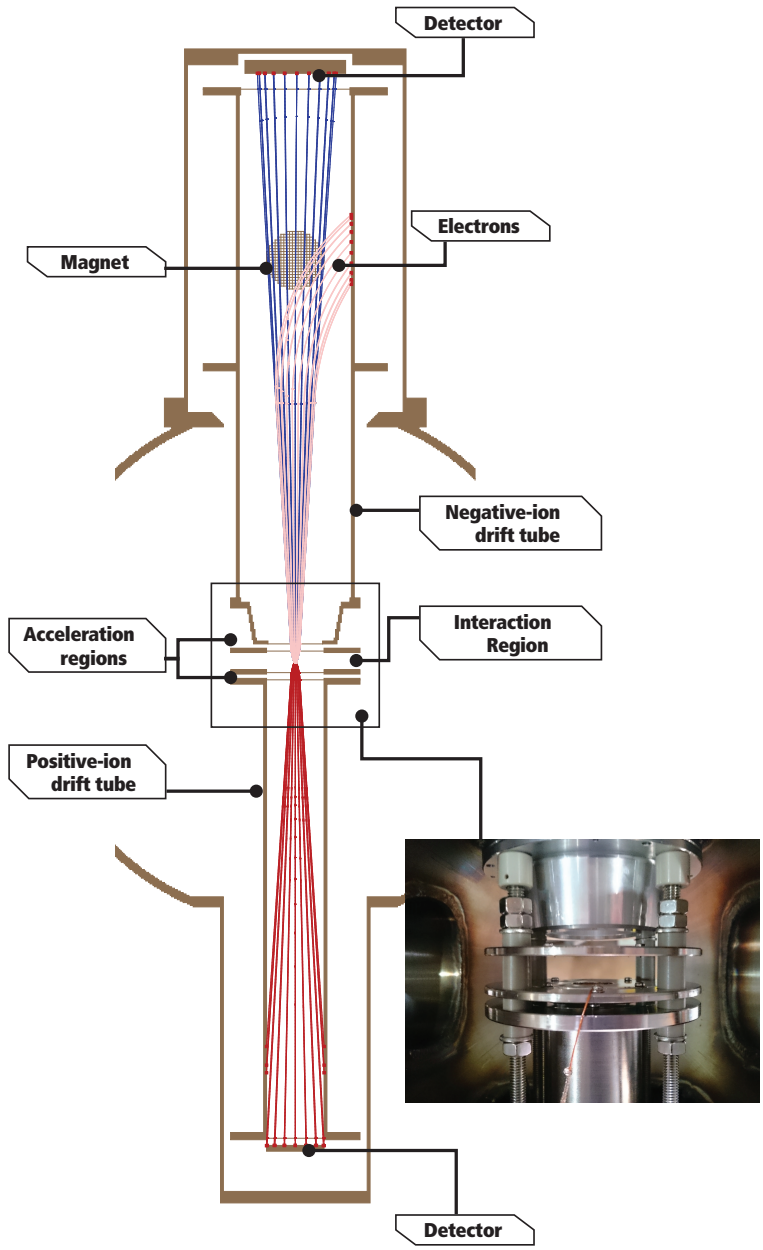


**Figure 3.3.** *Schematic drawing of the instrument setup with ChristianTOF (top) and RamiTOF (bottom). Negative ions, positive ions and electrons are created in the interaction region and accelerated into the spectrometers. The electrons are deflected in the negative–ion spectrometer by a weak magnetic field. The electrostatic simulation shows trajectories of $H^-$ ions (blue), $H^+$ ions (red) and electrons, each with 10 eV initial kinetic energy. It can be clearly seen that the 15 Gauss magnetic field only marginally deflects even the lightest ions. RamiTOF is narrower, and collects fast ion less efficiently. (Figure: J. Winqvist)*

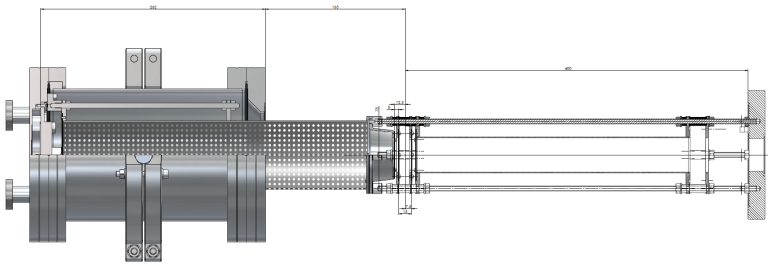

**Figure 3.6.** *Drawing of the negative–ion spectrometer mounted to the positive ion spectrometer. The different parts and design considerations are discussed in the text. (Figure: E.S. El Afifi)*

| *RamiTOF* | | |
|---|---|---|
| Source region width | $2s_0$ | 15 mm |
| Acceleration region width | $d$ | 5 mm |
| Drift tube length | $D$ | 319 mm |
| Detector width | $W$ | 40 mm |
| Repeller potential | $V_{\text{rep}}$ | +285 V |
| Extractor potential | $V_{\text{ext}}$ | −285 V |
| Drift tube potential | $V_{\text{drift}}$ | −2300 V |
| MCP front potential | $V_{\text{MCP}}$ | −2500 V |
| | $k_0$ | 8.1 |

**Table 3.1.** *Design values for RamiTOF. [42, 43]*

**Figure 3.4.** *The ChristianTOF (top) and RamiTOF (bottom) spectrometers mounted on the vacuum chamber. Light enters from the left side and the sample is injected from below. A diode measuring the light flux is mounted downstream the chamber.*

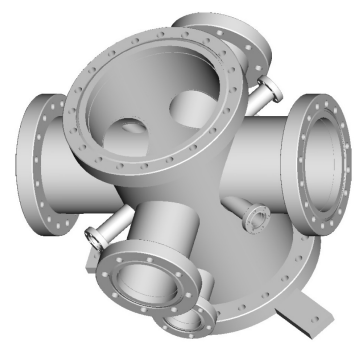

**Figure 3.5.** *The VG chamber. The VG spectrometer and ChristianTOF enter the chamber through the CF 100 openings.*

Figure 3.4 shows the two spectrometers entering the chamber. The light enters the setup from the left side opening and the sample is injected from the back through a needle.

The electron spectrometer is a *VG 220i* hemispherical analyser. The design of a *VG/ChristianTOF* setup was made to allow for detection of energy–resolved electrons and mass–resolved negative ions in coincidence (PENICO). Such a setup would also be able to record energy resolved PEPICO. This setup has not yet (March 2016) been commissioned. However, the design of the *ChristianTOF* was made to accommodate also this option. The *VG* spectrometer is mounted on the so called "VG chamber", shown in Figure 3.5. The opening of the VG spectrometer is situated 17 mm from the source point, which is the focal distance of the electron lens.

Figures 3.6 and 3.7 show the final design of the NIPICO setup with *ChristianTOF* and *RamiTOF* merged into one instrument. *RamiTOF* source region acts as source region also for both instruments, and the acceleration region for *ChristianTOF* is created at the interface between them.

Since the design requires that minimal changes are made to *RamiTOF*, it was necessary to start with its design values (see Ta-

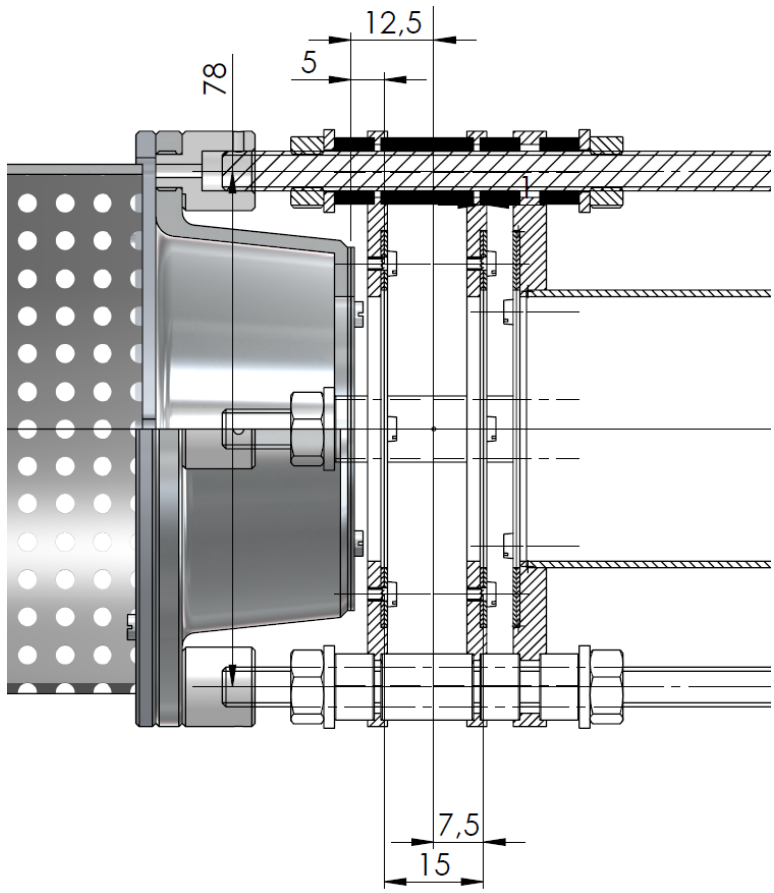


**Figure 3.7.** *Detail from Figure 3.6. The most important performance parameters – $s_0$ =7.5 mm and d =5 mm – are indicated. The width of the detector tube – W =77 mm – is almost equal to the drift tube width. (Figure: E.S. El Afifi)*

| *ChristianTOF* | | |
|---|---|---|
| Source region width | $2s_0$ | 15 mm |
| Acceleration region width | $d$ | 5 mm |
| Drift tube length | $D$ | 402 mm |
| Detector width | $W$ | 77 mm |
| Repeller potential | $V_{\text{rep}}$ | +285 V |
| Extractor potential | $V_{\text{ext}}$ | −285 V |
| Drift tube potential | $V_{\text{drift}}$ | −2650 V |
| | $k_0$ | 9.3 |

**Table 3.2.** *Design values for ChristianTOF.*

ble 3.1). It is clear from equations (3.10) and (3.12) that both space and energy focus gains from a high $k_0$, i.e. a large drift tube potential $V_{\text{drift}}$. The Wiley–McLaren condition (3.9) requires the drift tube $D$ to be long. As can be seen in Figure 3.1, ions with velocities directed perpendicular to the spectrometer axis will diverge and hit the detector at its periphery. A very long spectrometer requires a large detector area, which is in turn strongly limited by the cost of manufacturing large detectors. The maximum kinetic energy for which all ions are accepted can be approximated by the relationship

$$W = \sqrt{U_0}\left(2D\sqrt{\frac{1}{qV_{\text{drift}}}} + 4s_0\sqrt{\frac{1}{qV_{\text{ext}}}}\right), \tag{3.13}$$

assuming that the flight time through the acceleration region is small and the drift tube velocity component perpendicular to the spectrometer axis is small compared to the component parallel to the axis, which can be justified from Figure 3.1. Inserting the design values gives a limit at 7 eV for complete transmission in *RamiTOF*. It was considered necessary for *ChristianTOF* to have a high transmission to allow for detection of light ions (e.g. $H^-$) with high kinetic energies. Electrostatic simulations were performed for $U_0 = 10$ eV ions. It was found that it was not sufficient with a $W = 40$ mm detector if $k_0 > 8$ was to be kept. It was eventually decided to use a commercial *Hamamatsu* detector assembly, model F2226-24S, with $W = 77$ mm active area. This larger sized detector allowed a slightly longer flight tube without loss of transmission. The final design values for *ChristianTOF* is given in Table 3.2. The accelerator region width $d$ was kept to the same value as in *RamiTOF* since a reduction of this value turned out to be technically complicated. The accelerating field between meshes is $\sim 5$ kV/cm. However, at some points the distance between the two potentials is closer to 2 mm (see Figure 3.7).

Applying *ChristianTOF* design values to equation (3.13) shows that the instrument has full transmission at 15 eV. The energy–related mass resolution $M_U$ (equation (3.12)) at 15 eV is however only 11. This is a lesser problem since only light fragments are expected to carry these high kinetic energies. *RamiTOF* has been calculated

to have a space–related mass resolution $M_s = 200$ [43]; *ChristianTOF* should be slightly better due to higher $k_0$.

The standalone version of *ChristianTOF* was, for simplicity, developed with identical design values as the ion/ion coincidence version. The additional parts required for this version was made to resemble the *RamiTOF* as much as possible.

### 3.2.2 Physical design

The essential parts of an ion TOF is the detector, the drift tube and four transmission meshes (repeller, extractor, and drift tube entrance and exit). The physical design concerns how these elements are mounted and electrically isolated from each other, how the electric potentials are supplied, the connection to the vacuum chamber, alignment, behaviour under vacuum conditions and how the sample is injected to the source region.

The outer size of the detector assembly (Ø123 mm) implies that it cannot be mounted on a CF 100 flange. Rather, a CF 150 flange is needed. However, the front of the instrument must still fit the CF 100 opening. This necessitated the construction of a chamber seen in Figure 3.6 which has an adapter for the CF 100 flange. The length of the vacuum chamber was adapted to the 163 mm distance between the centre of the main vacuum chamber and the CF 100 opening. The Ø77 mm drift tube inhibits mounting on rods as in *RamiTOF*; there is not enough space for the (grounded) rods to extend into the main chamber. The solution was to mount the drift tube on the flange, and the extractor and repeller mesh holders on the drift tube.

All metal parts except the transmission meshes are made from aluminium. This material was chosen partly because aluminium is non-magnetic, which is beneficial when a magnetic field is introduced, and partly because the lower cost and ease of manufacturing. The drawback is oxide layers that form on its surface which can cause local charging during heavy bombardment of charged particles.

Isolating parts are made from PEEK (polyether ether ketone), a thermoplastic material often employed in high–vacuum applications. PEEK has low outgassing compared to other plastics and can be put in the vacuum chamber without destroying high–vacuum conditions [44, p. 117]. PEEK is used to mount the drift tube to the flange and, in the stand-alone version, to mount the extractor and repeller meshes.

Transmission meshes were bought from *Precision Eforming Llc*. The 70 wires-per-inch gold mesh had a transmission of 90 %, as specified by the manufacturer[5]. The standalone instrument uses four meshes. The mesh holders for the repeller, attractor and drift tube entrance meshes were designed as an exact replica of *RamiTOF* so that the same mesh–mounting equipment could be used. The drift

[5] The ion passes through three meshes, which gives a total transmission of ∼70%.

| | | *RamiTOF* | *ChristianTOF* |
|---|---|---|---|
| Extractor/repeller potential | $V_{\text{ext}}$ | −92 V | +92 V |
| Drift tube potential | $V_{\text{drift}}$ | −740 V | +854 V |
| MCP front potential | $V_{\text{MCPfront}}$ | −2500 V | +900 V |
| MCP back potential | $V_{\text{MCPback}}$ | | +2600 V |
| Anode potential | $V_{\text{anode}}$ | ground | +2700 V |
| Energy acceptance | eqn. (3.13) | ∼2 eV | ∼6 eV |

**Table 3.3.** *Low field settings for the ChristianTOF/RamiTOF assembly.*

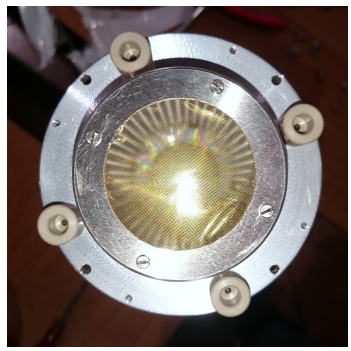

**Figure 3.8.** *The drift tube entrance mesh mounted to the ChristianTOF in its coincidence configuration. The PEEK docking for the rods of RamiTOF can also be seen (compare to Figure 3.4).*

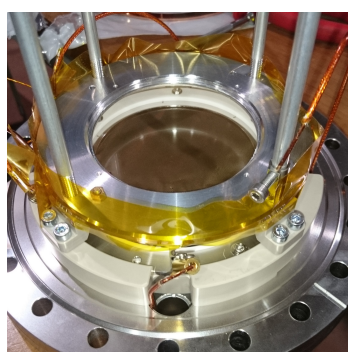

**Figure 3.9.** *The drift tube exit mesh mounted before the detector. The drift tube itself is not mounted in this picture. The PEEK mounting of the drift tube supporting rods can also be seen.*

tube exit mesh, which is a shield for the detector front, was the same size as the detector (Ø77 mm).

The four isolated docking points, seen in Figure 3.8, ensures that *RamiTOF* can be properly aligned to *ChristianTOF*. Since the rods on *RamiTOF* and the *ChristianTOF* drift tube are at different potentials, the connection had to be isolated. When docked, the tandem spectrometer assembly becomes one rigid structure. For alignment purposes, this means that the assembly must be treated as one single piece mounted on two flanges. *RamiTOF* can be laterally aligned due to its bellow mounting, while *ChristianTOF* has a rotatable flange. The mounting procedure is (1) mounting the *RamiTOF* flange, (2) releasing the bellow, (3) inserting *ChristianTOF* and rotate the flange to match the positions of *RamiTOF* rods, (4) fixing the *ChristianTOF* flange, and (5) fixing the bellow. The assembly should then be more or less centred in the chamber. If not, the final alignment is made by moving the chamber relative to the light beam when assembled at the beamline.

### 3.2.3 Detector and signal handling

The detector is a double Chevron–stacked MCP with $W = 77$ mm active area and single–anode readout. A constraint set by the detector manufacturer is that the potential difference between anode and base plate cannot exceed 2500 V. The original design of the instrument had the detector base plate directly mounted on the grounded flange. This limited the anode potential $V_{\text{anode}}$ to +2500V, though we deemed that it could be stretched to +2700V without risk to the detector. This mounting was used for the measurements presented in Papers **I** and **II**. The risk of too high potentials is that sparking occurs and destroys the detector. For positive–ion detection, the MCP front has a high negative potential. In *RamiTOF*, the anode could be grounded while the MCP front was set to −2700 V. For *ChristianTOF* the potential gain is required to add to an already high positive potential on MCP front, i.e. $V_{\text{drift}} \leq V_{\text{MCPfront}} \ll V_{\text{MCPback}} < V_{\text{anode}}$, which makes $V_{\text{drift}}$ restricted by the gain potential. The low–field settings used is listed in Table 3.3. It's clear from equation (3.13) that the new settings drastically reduces the kinetic energy acceptance of the instrument. Also, a reduction of $V_{\text{MCPfront}}$ reduces the detection effi-

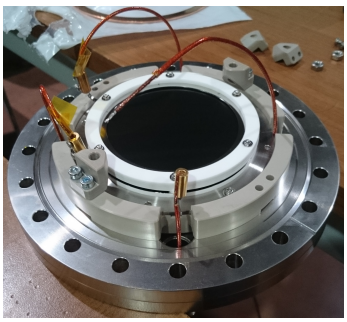

**Figure 3.10.** *The MCP stack detector assembly mounted on the end flange of ChristianTOF with the detector isolator and cable connections to SHV feedthroughs.*

ciency of negative ions while electron detection efficiency increases. Data provided by the manufacturer lists the maximum electron detection efficiency 85% at 500 eV kinetic energy while it is below 50% at 2650 eV (the *ChristianTOF* design value). Detection efficiencies for ions depend on their mass as well as kinetic energy, but are claimed to be between 60 and 85% for kinetic energies above 2000 eV, and between 5 and 60% for kinetic energies between 500 eV and 2000 eV.

As this problem became obvious during commissioning in March 2015, a detector isolator was constructed. Figure 3.10 depicts the detector mounted in the large isolating PEEK part which was commissioned to isolate the substrate from the flange. The substrate, now on floating potential, was connected directly to the MCP back, thereby reducing the potential drop between the anode and substrate to 100 V. This allowed for operation with the original design values, including the optimal MCP gain ($V_{\mathrm{MCPback}} - V_{\mathrm{MCPfront}}$) which was found by trial to be 1850 V.

The three pins on the detector and the drift tube were connected with short cables to SHV feedthroughs on CF 16 flanges. They were in turn connected to HV power supplies. The detector signal is taken from the anode and led via a capacitor close to the SHV pin to a preamplifier. The amplified signal is passed through a discriminator and then read by a time-to-digital converter (TDC, model AM-GPX, manufactured by *ACAM Messelectronic*) with 80 ps time resolution. The signal from the detector in *RamiTOF* is treated the same way. The signal handling system has been in use for several years at the Gasphase beamline [42].

### 3.2.4 The negative particle momentum filter

A negative–ion instrument must effectively suppress the unwanted detection of electrons. Electrostatic instruments, i.e. where only time–independent electric fields are used to steer particles, make *spatial* dispersion based on the charge–to–energy ratio [45]. Two particles with the same charge, kinetic energy and direction of movement will travel on identical paths, independent of their mass[6]. This means that an electrostatic instrument optimized for singly charged ions will steer also electrons to the detector. A magnetic field, on the other hand, makes spatial dispersion based on charge–to–momentum ratio. Electrons, which carry 44 times less momentum than the lightest ion at equal energy, are easy to deflect in a magnetic field. An early version of an electron–deflecting filter by Schermann *et al.* [46] consisted of a small dipole electromagnet in a $\mu$-metal[7] casing. TOF–based negative–ion spectrometers have used similar solutions either with permanent magnets or electromagnets [48–50].

[6] In contrast to the *temporal* dispersion, which is based on mass–to–charge ratio

[7] $\mu$-metal is a nickel-iron alloys used to shield components from magnetic fields. [47, p. 359f]

Two permanent neodymium magnets were acquired and a holder for them was constructed for mounting outside vacuum (Figure 3.2). Having the permanent magnets mounted outside vacuum made it possible to quickly remove the magnetic field for tests of the spectrometer performance. Simulations were performed in the SIMION software [51] to ensure that the deflection would prevent electrons reaching the detector while not disturbing the ion TOFs (Figure 3.3).

Electrons emitted by photoionization from valence shells have energies close to the photon energy. In addition, they are accelerated by the drift potential to several keVs. Simulations were performed for electrons with kinetic energies up to 3000 eV. It was found that two magnets mounted directly against the vacuum chamber, facing each other, required 15 Gauss magnetic field to deflect all electrons, independent on their start position in the source region and their direction of travel. Hydrogen ions were only marginally deflected and their flight times deviated $< 2$ ns from the non–deflecting case.

The perforated drift tube was designed to allow the deflected electrons to escape the drift tube. The argument was that electrons with kinetic energies in the order of several keV will create secondary electrons when hitting the inside of the drift tube. If the electrons instead escape the drift tube, they will be decelerated by the grounded vacuum chamber and eventually hit it with lower energy. However, simulations showed that the drift tube and chamber can mimic a reflectron; there is a non-negligible probability that deflected electrons are focused back into the perforated drift tube and subsequently hit the detector. Some electrons were indeed recorded in all acquisitions. The positions of the permanent magnets was therefore optimized to reduce the electron count. It was found that reduction of electron signal was most effective when the magnets were positioned very close to the interaction region. Also, contrary to simulations, the most efficient reduction of electrons occurred when the magnets were positioned on the same side of the drift tube. It can be speculated that the magnetic field from two small magnets causes the electrons to spiral towards the magnet, hindering the ”reflectron mechanism” to refocus the electrons to the detector.

### 3.2.5 Pulsed and continuous extraction

The choice between pulsed and continuous extraction is dictated by the need for any TOF–based experiment to have a start signal which is correlated to the true start of the ion's flight. There are a number of ways in which a start signal can be provided. This topic is treated in detail in Chapter 4 and in the popular scientific summary in the author's Licentiate thesis [3]. In short, the start can be initiated by an internal trigger or an external trigger. An internal trigger is provided by the detection of the ionisation event directly. In PEPICO, the start trigger is given by an electron detection while the ion de-

tection provides the stop. Since an electron is much faster than an ion, its detection can be considered to be immediate and the time between the two detections is the ion flight time. To use an external trigger means that the actual flight is induced by an event created by the user. In this application, the external trigger is a pulsed electric field in the source region. The created ions are considered to remain at rest in the source region until they are accelerated by the pulsed field.

Paper **I** introduces the two acquisition modes, pulsed mode and constant extraction mode, but focuses on the latter. This section provides additional background on the pulsed mode performance. The experimental conditions were the same as in Paper **I** and the sample is sulphur hexafluoride ($SF_6$). In the *pulsed extraction mode* an extraction field is produced by a pulsed high-voltage supply. We used an instrument from *Directed Energy Inc.*, model PVM 4210, controlled by a pulse generator (*Stanford Research* DG535) to produce two identical square pulses of opposite polarity with 92 V amplitude, 22 $\mu$s length and 10 kHz repetition rate. The pulse trigger signal is used as the start trigger for the time–of–flight measurement. This mode produces positive and negative TOF spectra independently, and can therefore be used to measure the flight times of individual fragments.

Figure 3.11 (a) and (b) show positive–ion mass spectra measured with both spectrometers. The positive–ion spectrum measured by *ChristianTOF* was acquired by changing the polarity of all electrostatic potentials. The flight times of positive ions are identical to those of negative ions for opposite polarities. We also measured a negative–ion spectrum with *ChristianTOF*. This spectrum was dominated by electron–triggered events even when the magnetic field was applied. Nevertheless, the $F^-$ peak could be identified, and its flight time was verified to match that of the $F^+$ peak in the positive–ion spectrum (a). All measured flight times have an excellent match with SIMION simulations. The PEPICO spectrum in Figure 3.11 (c) illustrate the effect of the line broadening and changes in branching ratios. Here, *ChristianTOF* is used as an electron detector without magnetic deflection, and provides the start signal while *RamiTOF* provides the stop.

While it is in principle possible to deduce NIPICO events with pulsed extraction, in practice the efficiency of the instrument is too low for this to be a feasible method. The comparison of spectra (b) and (c) highlight some of the limitations of the pulsed method. Because the pulse is not correlated to the ionization process, many ions, even with low kinetic energies, have sufficient time to escape the interaction region before the pulse is applied. The pulsed mode therefore favours the detection of slow and heavy ions. In addition, due to the movements of the ions, the effective source size seen by the spectrometer spans the whole source region. Using the notation in Section 3.1 this implies $\delta s / s_0 = 1$. This causes a significant broadening

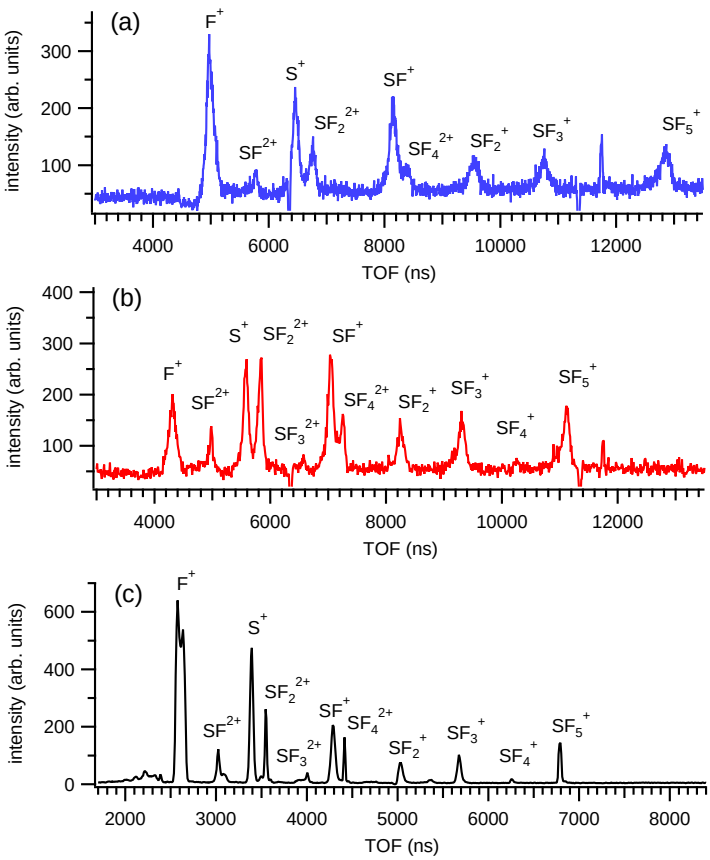


**Figure 3.11.** *A TOF spectrum of positive ions obtained with (a) ChristianTOF and (b) RamiTOF in pulsed mode with low–field settings. (c) A (non–pulsed) PEPICO spectrum with ChristianTOF collecting electrons without magnetic deflection. The spectrum in (c) was collected with extractor meshes at ±240 V constant extraction and the positive-ion drift tube at −2000 V. All spectra were measured at the S $2p_{1/2} \rightarrow a_{1g}$ resonance (173.8 eV) for 900 seconds each. The peak at ∼11700 ns is an artefact.*

| Ion | | | $H^+$ | $H_2^+$ | $O^{2+}$ | $O^+$ | $OH^+$ | $H_2O^+$ |
|---|---|---|---|---|---|---|---|---|
| | $m/q$ | | 1 | 2 | 8 | 16 | 17 | 18 |
| | | TOF | 1056 | 1494 | 2988 | 4222 | 4351 | 4476 |
| $e^-$ | | 0 | 1056 | 1494 | 2988 | 4222 | 4351 | 4476 |
| $H^-$ | 1 | 1149 | -93 | | 1839 | 3073 | 3202 | |
| $H_2^-$ | 2 | 1623 | -567 | | 1365 | 2599 | | |
| $O^-$ | 16 | 4592 | -3536 | -3098 | | | | |
| $OH^-$ | 17 | 4734 | -3678 | | | | | |

**Table 3.4.** *Simulations of flight times for NIPICO from* $H_2O$ *, as it was simulated for Paper* ***II****. The times measured in the experiment are* $t_{\mathrm{meas}} = t_{\mathrm{RTOF}} - t_{\mathrm{CTOF}}$.

of mass peaks (several 100 ns) compared to a PEPICO measurement where the ion is extracted immediately following its creation. This is particularly true with the low-voltage settings in Table 3.3.

The positive–ion spectrum (b) shows different branching ratios compared to (a) and (c). *RamiTOF* has a narrower drift tube and smaller detector than *ChristianTOF*. Therefore it is expected to detect fewer fast (light) fragments. This is seen clearly when comparing the $F^+$ peak in (a) and (b). In (c), the PEPICO measurement, the branching ratio of $F^+$ is similar to (a). In addition, doubly charged ions have a higher detection probability in *RamiTOF* since the total energy of the detector hit is much higher than in *ChristianTOF* [52]. This can explain their relatively higher abundance in (b) and (c).

The efficiency of the instrument is significantly increased by continuous extraction of positive and negative ions. Static electric fields are used to extract ions from the interaction region. Flight–time differences of two fragments can be constructed from the hits of ions on the two detectors. Combined with flight times measured in the pulsed mode and aided by simulations of flight times for all possible negative and positive ionic fragments, each flight–time difference can be assigned to a coincidence between a specific negative ion and a specific positive ion.

In simple molecules with few possible fragments this is straightforward since the possible combinations of positive and negative ions are few. In more complicated molecules there are more combinations, and also an increasing risk for a temporal overlap between several pairs. In addition, since electron counts cannot be completely avoided, there is also a risk of a temporal overlap between electron/positive–ion and negative–ion/positive–ion coincidences.

Electrostatic simulations are used to adapt the flight times of all possible ion and electron combinations in order to minimise overlaps. Table 3.4 show how expected peak positions for NIPICO events are calculated for the $H_2O$ molecule. Figure 3.12 translates simulated times to peaks in the TOF spectrum.

As the complexity of the molecule increases, it is valuable to use the drift tube potentials to temporally shift the peaks in order to iden-

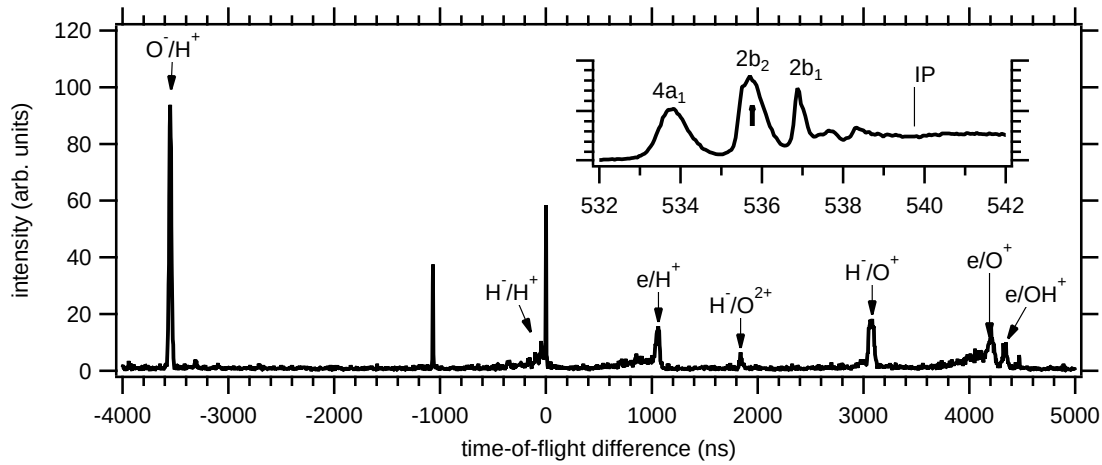


**Figure 3.12.** *NIPICO TOF spectrum recorded for 40 minutes at the* O $1s \rightarrow 2b_2$ *resonance (*535.8 eV*) with assignments of the major NIPICO and PEPICO channels. The sharp features at* $\Delta t = 0$ ns *and* $\Delta t = -1100$ ns *are artefacts arising from hardware (see Paper* **I** *for details). The* $H^-/H^+$ *peak is situated just to the left of the* $\Delta t = 0$ ns *feature. The inset shows the total positive ion yield at the O 1s edge of water.*

tify them. Since all detected peaks include one negative and one positive species, they should respond to an increased acceleration in either TOF instrument. If the drift potential $V_{\text{drift}}$ is increased in *ChristianTOF*, the flight times of negative ions should become shorter and the measured time–of–flight differences for those coincidences should be longer. The change should be large for heavy negative ions and small for light ions. All NIPICO peaks involving the same negative ion should shift with equal magnitude. PEPICO peaks should not shift, as the electron flight time is only marginally decreased. Similarly, if the $V_{\text{drift}}$ is increased in *RamiTOF*, the flight times of positive ions should become shorter and the measured time–of–flight differences for those coincidences should be shorter. NIPICO peaks and PEPICO peaks should shift equally. Figure 3.13 shows three NIPICO spectra measured at the O $1s \rightarrow \pi^*$(C−O) resonance (540.5 eV) of formic acid (HCOOH). Here, the drift potential in *ChristianTOF* and *RamiTOF*, respectively, has been increased by 100 V. It can be clearly seen that NIPICO peaks shift in both cases, while PEPICO peaks only shift in the latter. This technique can help to identify anomalies, such as the peaks between $O^-/H^+$ and $C^-/H^+$ . At first glance these could be deemed to belong to $CH^-/H^+$ and similar channels. Figure 3.13 reveals that they shifts much less than $CH^-$ in the negative channel and almost nothing in the positive channel. This is inconsistent with any NIPICO channel. The origin of these peaks are yet not known.

NIPIPICO channels are present when two positive ions come in

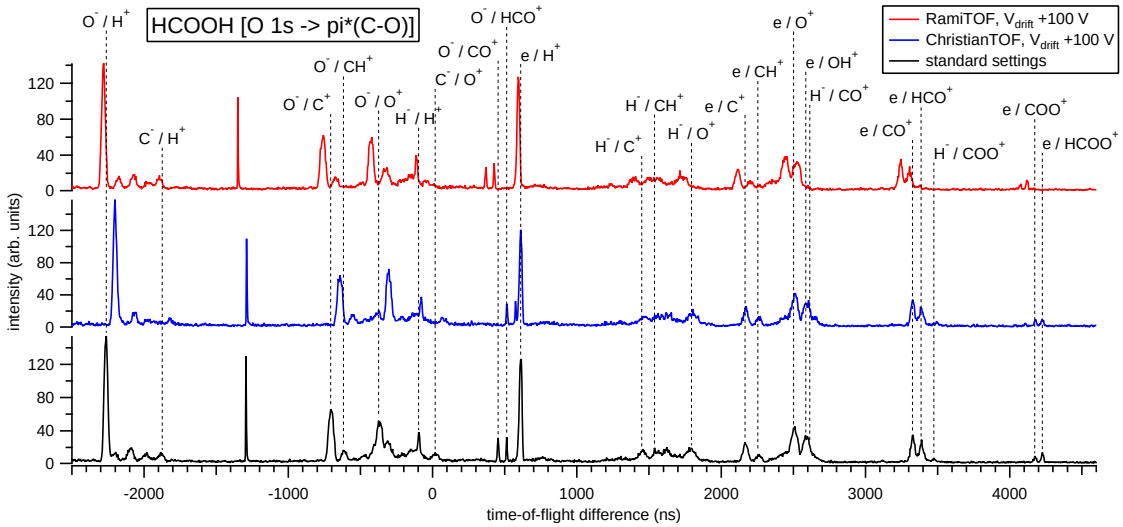


**Figure 3.13.** *NIPICO spectra measured at the* O 1$s \rightarrow \pi^*$(C−O) *resonance (540.5 eV) of formic acid (HCOOH). Each spectrum was measured for 80 minutes. The change in peak positions was created by increasing* $V_{\text{drift}}$ *on ChristianTOF (middle) and RamiTOF (top). The vertical lines indicating NIPICO channels are centred on the peaks in standard settings.*

coincidence with one negative ion. Since the instrument can record signals continuously, it is possible to correlate coincidences with several fragments. Figure 3.14 show parts of the NIPIPICO map of the same resonance. It is possible to identify several NIPIPICO channels with $O^-$ and one with $C^-$. Not seen in this map is the several NIPIPICO channels with $H^-$, which arrive at longer flight times.

Peak shapes both in NIPICO and NIPIPICO carry information about the kinetic energies of the fragments. Broad NIPICO peaks, sometimes with a clear split structure (see Figure 3 in Paper **I**), indicate large kinetic energy release. In the NIPIPICO map this can be seen as narrow and tilting islands, such as $O^-/C^+/O^+$ in Figure 3.14. It was shown by Rühl and Flesch [50] that the tilt of the island in NIPIPICO can be used to estimate the kinetic energy of the fragments and to determine if the dissociation process is sequential.

### 3.2.6 Collecting data

The experimental conditions at the Gasphase beamline has been treated in Papers **I** and **II**, respectively.

Yields of negative ions are generally low following x-ray excitation. Although the NIPICO instrument has been proven to be efficient, any experiment trying to collect negative ions is time-consuming. Positive ions outnumber the negative ions by several or-

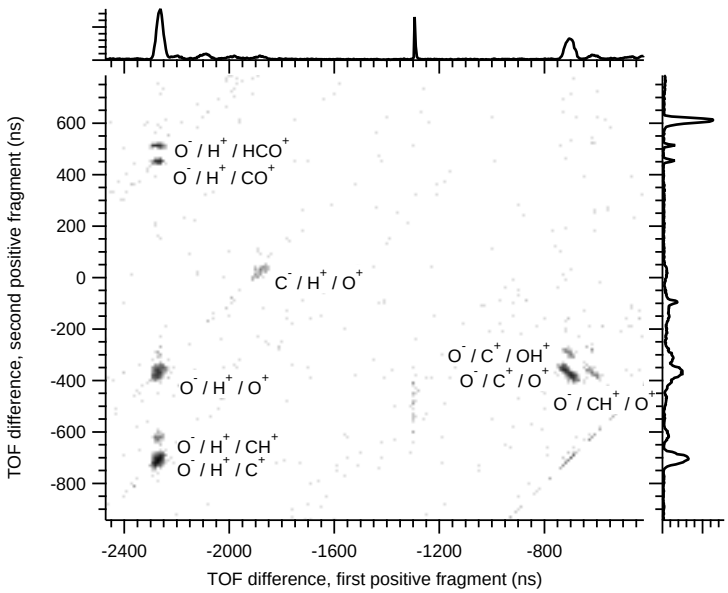


**Figure 3.14.** *Detail from a NIPIPICO map measured at the* O 1$s \rightarrow \pi^*$(C−O) *resonance (540.5 eV) of formic acid (HCOOH). The map was measured during 60 minutes. Each island on the map correspond to a triple coincidence channel.*

ders of magnitude. The limiting factor for the speed of acquisition is therefore the maximum count–rate in *RamiTOF* which is limited to 10000–20000 Hz in order to increase the lifetime of the MCP detector. *ChristianTOF* count–rate was found to be roughly 100 times less. Stray electrons are a significant fraction of the counts.

The aim of the experiments carried out so far has been to chart fragmentation channels of all negative and positive ionic products at the resonances close to an ionization edge. The measurements have required between 20 and 60 minutes per photon energy in order to be able to clearly distinguish several NIPIPICO channels. It is common practice in fragmentation studies to scan the photon energy in fixed energy steps with equal amounts of time spent on each step. With this approach, the O and C edges of methanol ($H_3COH$) and formic acid (HCOOH) were measured. To scan one edge required between 12 and 20 hours of beamtime.

## 3.3 Instrumentation for energy–resolved photoelectron/positive–ion coincidence

The energy–resolved photoelectron/positive–ion coincidence spectrometer setup used for experiments in Paper **III** follows a design

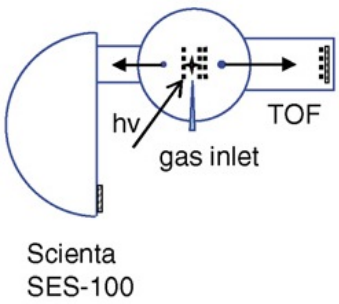


**Figure 3.15.** *Schematic drawing of the PEPICO setup. [53]*

idea which has been employed in several earlier studies. This particular setup has been used at MAX II several times and is well described in Ref. [53], with the exception of the ion–TOF which is described in Ref. [54]. Only some features will be discussed here.

Energy–resolved PEPICO differs from "normal" PEPICO encountered in Section 3.2. In those experiments, the electron was simply used as a by-product of ionization. In energy–resolved PEPICO, the electron has to be be detected with high energy resolution, and its low momentum compared to the ion becomes a hurdle. That is why a coincidence event in a hemispherical–analyser/ion–TOF setup should be recorded sequentially; first the electron, then the ion. The particularities of electron spectroscopy will be treated in subsequent chapters; a few features should nevertheless be noted here: The analyser works with a field–free source region. There is no field to guide the electrons towards the detector. As a result, the overall efficiency of the instrument is low. The hemispherical analyser and the ion TOF are mounted along the same axis and perpendicular to the light beam (see Figure 3.15). Following photoionization, the electron can escape the source region of the ion TOF, enter the hemispherical analyser and become detected. At that instant, a signal is transmitted to a pulse generator which provides an electric potential to the extractor and repeller mesh of the ion–TOF. It is expected that heavy ions move only a short distance during the electron's flight time. Light ions, which can carry significant kinetic energies, escape detection more easily. Ion–TOF performance in pulsed mode was discussed in section 3.2, the difference being that the ion creation in this case is correlated to the pulse, which increases space–related mass resolution.

Compared to *ChristianTOF*, the ion-TOF employed in this setup is narrower with a detector size $W = 25$ mm, but still with a quite long drift tube $D = 320$ mm. The full kinetic energy acceptance (equation (3.13)) is below 3 eV, and one should be reminded that this is an estimate for ions which do not move in the source region before the extraction, which is obviously not the case here. A significant share of the ions created will thus never be detected. Transmission is limited in both the ion and the electron instrument, which inevitably leads to accidental coincidences, i.e. when two apparently coincident detections originate from different ionization processes. They are unavoidable and cannot be separated from true coincidences on an event-by-event basis [55]. Rather, the subtraction of background has to be treated by statistical methods [53]. Ions are measured both in coincidence with electrons and non–coincident with an external trigger. A "true" electron–ion coincidence spectrum is obtained by subtracting the random spectrum from the coincident spectrum. This can be applied to situations where one of several ions are detected in coincidence. In Paper **III** the analysis is restricted to single positive ions.

An additional feature of random event subtraction is the estima-

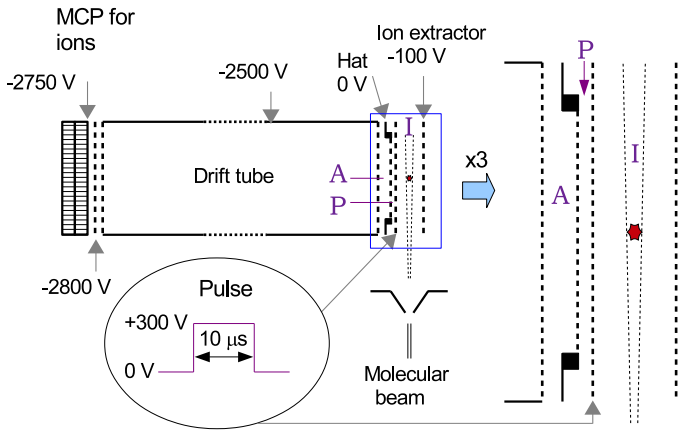


**Figure 3.16.** *Schematic of the experimental setup. HR fragments created in the interaction region (I) can enter the time-of-flight spectrometer. A positive pulsed potential is applied to the electrode on the left side of interaction region. Ions are prevented from entering the instrument by a suitable arrangement of potentials. (©AIP Publishing LLC)*

tion of relative escape probabilities of ions at different electron energies by comparing the coincident and non–coincident electron spectrum. Since a free electron is only emitted in an ionization event, at least one ion should always be present. Since ions are often lost – in Paper **III** about one in fifty electron detections was followed by an ion detection – the coincident and non–coincident spectrum cannot be compared directly. However, the ratios between them at different energies can give an indication of a high proportion of lost ions. In Paper **III**, this feature is used to gauge an increase in fast $H^+$ production at certain Auger electron energies.

## 3.4 Instrumentation for field ionization of high-Rydberg fragments

Since the experimental setup is well described in Paper **IV**, only some features will be discussed here. The experimental setup, including the spectrometer, is shown in Figure 3.16. High–Rydberg (HR) fragments are created in the interaction region (I) where the light crosses the molecular beam. A suitable arrangement of potentials make sure that positive ions, negative ions and electrons are deflected. Some HR fragments enter the ionization region (P) where they can be field ionized as a positive pulsed potential is applied to the mesh separat-

| *HR TOF* | | |
|---|---|---|
| Interaction region width | | 11 mm |
| Ionization region width | $2s_0$ | 2 mm |
| Acceleration region width | $d$ | 5 mm |
| Drift tube length | $D$ | 203 mm |
| Detector width | $W$ | 40 mm |
| Pulse potential | $V_{\text{pulse}}$ | +300 V |
| Extractor potential | $V_{\text{ext}}$ | ground |
| Drift tube potential | $V_{\text{drift}}$ | −2500 V |
| | $k_0$ | 17.7 |

**Table 3.5.** *Dimensions and potentials for the HR setup. See also Paper **IV** and Ref. [56]*

ing the interaction and source regions. The field ionized fragments are accelerated into the acceleration region (A), further accelerated into the drift tube and eventually detected at the MCP. The pulse is provided by an external trigger (10 kHz) which also acts as the start trigger for the flight time measurement.

It should be noted that the setup, if the interaction region is disregarded, works similar to *ChristianTOF* in pulsed mode. We can recognize the drift tube and acceleration region (A) directly. The ionization region (I) acts as source region. The operating values in Paper **IV** are given in Table 3.5. Similar to *ChristianTOF* in pulsed mode, the effective source size seen by the spectrometer is expected to span the whole ionization (source) region ($\delta s/s_0 = 1$) which would be expected to give rise to broad peaks. However, the HR setup differ from *ChristianTOF* in that $s_0$ is smaller than $d$. Also the extraction field in the HR setup ($\sim$ 1.5 kV/cm) is higher than for *ChristianTOF* (0.2 kV/cm), and the space–related mass resolution equation (3.10) is not valid for this case. For the HR setup, the best value for $s_0$ is the centre of the ionization region. We recall that the space focus condition (equation (3.9)) was found by solving equation (3.5) for $\frac{\mathrm{d}t}{\mathrm{d}(\delta s)}|_{\delta s=0} = 0$. The solution to the differential equation finds potentials which allow two fragments that are created at small distances from $s_0$ to arrive to the detector simultaneously. However, as can be seen from the curious behaviour in Figure 3.17, ions created at the edges of the ionization region can deviate considerably from this ideal flight time. At the space focus condition, ions created very close to the mesh separating the ionization and acceleration regions reach the detector fast. The flight time of these ions are independent of $V_{\text{pulse}}$ since they are always created close to the ground potential. All other ions become faster when $V_{\text{pulse}}$ increases. The ions created at the far edge of the ionization region, bordering the source region, gain most kinetic energy. It appears that the space focus condition is not suitable for this situation. Figure 3.17 shows temporal dispersion for three $V_{\text{pulse}}$ potentials, with and without initial kinetic energies of the field ionized fragments. $V_{\text{pulse}} = +230$ V correspond to the space

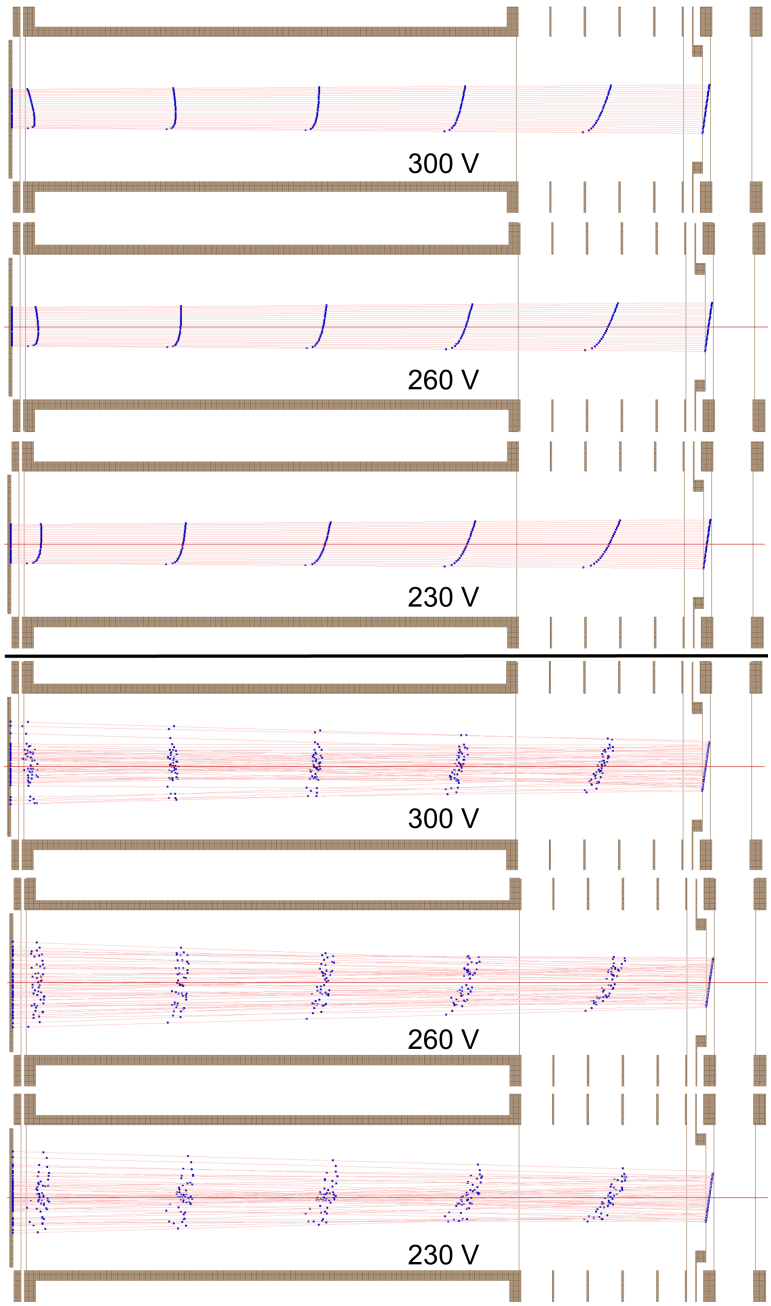


**Figure 3.17.** *Electrostatic simulation of field–ionized C(HR) fragments for three values of the $V_{\text{pulse}}$ potential. Blue dots show a snapshot of the ions' positions every 200 ns following creation. To simplify the reading of the trajectories, all ions are created along a line which spans the diagonal of the ionization region. In reality, and in the simulations referenced in the text, ions are created in the entire ionization region. The HR fragments in the top three simulations have no initial kinetic energy, in order to illustrate the space focus. Fragments in the bottom three have initial kinetic energies in a Gaussian distribution centred at* 4 eV *($\sigma = 1$ eV).*

focus condition. The simulations indicate that a higher pulse potential focuses ions better. However, it is not obvious which value produces the best focus conditions. Therefore numerical simulations were performed[8] using an iterative script where different sets of electrode potentials were simulated for a set of fragments with different kinetic energies and start positions in the entire ionization region. It was found that the electric fields in the acceleration region and ionization region should have a ratio of $\sim 8.3$, which was also used in experiments.

The pulse potential $V_{\text{pulse}}$ does not only determine the space focus, but also which fragments can be field ionized. As noted in Paper **IV**, an electric field $E$ lowers the ionisation potential of the fragment by $\Delta U \approx 6\sqrt{E}$, where $E$ is measured in V/cm and $\Delta U$ in cm$^{-1}$ [57]. For $E = 1500$ V/cm, we get $\Delta U = 232$ cm$^{-1} = 0.029$ eV. With the members of a Rydberg series converging to the ionization limit according to $U_{nlm} = -R_M/(n-\delta_l)^2$, where $R_M$ is the Rydberg constant and $\delta_l$ the quantum defect [58], that higher fields can ionize HR fragments with lower $n$. The choice of $V_{\text{pulse}}$ thus become also a selection of the Rydberg–level threshold. We found in Paper **IV** that $E = 1500$ V/cm was sufficient to ionize hydrogen HR-states with $n \geq 22$ and carbon atoms with $n \geq 20$.

[8] These simulations were performed by J. Antti Kettunen.

CHAPTER 4

# MAKING TIMING–BASED INSTRUMENTATION USEABLE AT STORAGE RINGS

This chapter will provide an overview on solutions currently sought to overcome the timing restrictions of storage rings. The solutions are related to accelerators and beamlines i.e. modifying the time structure of the light *before* it reaches the sample. Two particular opportunities related to endstation instrumentation adaptation will be discussed in detail in subsequent chapters: Gating of an ARTOF electron spectrometer in Chapter 5, and a high–resolution high–transmission electron–electron coincidence experiment in Chapter 6. The chapter concludes with a short discussion on how combinations of different approaches can be successfully utilised and how the electron spectroscopy community can benefit from the strengths of new timing–based spectroscopic techniques. A longer discussion on particular opportunities for the MAX IV Laboratory will be raised in Chapter 7. These topics are also treated in Paper **V**, which I have authored together with members of a working group exploring possibilities of timing-based experiments at the MAX IV storage rings.

## 4.1 Temporal properties of storage ring light sources

Light emitted from a storage ring has a temporal profile which is a replica of the electron bunch structure. The duration of the light pulses scales with the spatial length of the electron bunch (bunch–length divided by the speed of light), and the intensity of each light pulse is proportional to the stored charge. Electron bunches follow the design orbit, which is divided into a fixed number of evenly spaced "buckets". Those are volumes where electron bunches can re-

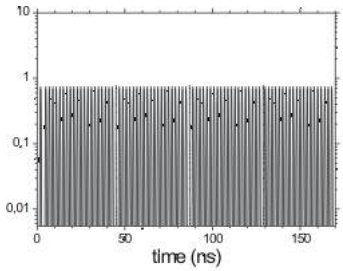


**Figure 4.1.** *Multi–bunch mode.*

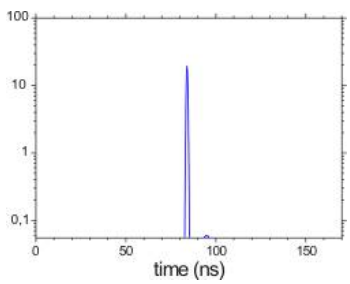


**Figure 4.2.** *Single–bunch mode.*

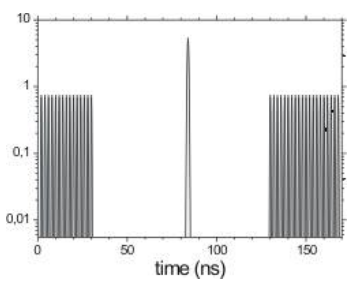


**Figure 4.3.** *Hybrid mode.*

side. Their spacing is determined by the frequency of the RF system [59]. Two temporal properties of the light source have to be considered in timing–based spectroscopies: The length of the light pulse (pulse length) and the frequency of the pulses (repetition rate).

The overall bunch structure can be manipulated by different filling patterns, where one can distinguish between multi–bunch modes (Figure 4.1), single–bunch (Figure 4.2) and hybrid modes (Figure 4.3). The most straight–forward way to store electrons in the storage ring is to fill each bucket with equally large numbers of electrons (the multi–bunch mode)[1]. For most users, multi–bunch light is perceived as continuous (and is often referred to as quasi-continuous). Multi–bunch modes provide the highest intensity and shortest pulse separation achievable for a storage ring. Modern storage rings optimized for high intensity therefore favour multi–bunch operation. Another cause for multi–bunch operation is the use of Landau cavities at storage rings optimized for low–emittance. These cavities primarily increase stability of the electron beam as well as elongating the bunches [62, 63]. The latter effect increases the lifetime of the beam due to a reduction of Touschek scattering[2]. Since the cavities in the storage ring lattice are driven, partly or fully, by the current passing through them, uneven filling patterns reduce the stabilizing effect of the Landau cavities [64]. Also, the reduced bunch lengthening shortens the life–time of the electron beam.

RF systems with 500 MHz frequency are used at a majority of synchrotron radiation storage rings, giving 2 ns bunch separation in multi–bunch mode. The exceptions include the storage rings at the MAX IV Laboratory in Lund, Sweden [1], the ASTRID2 ring in Aarhus, Denmark [65], and the Solaris-ring in Krakow, Poland [66], where 100 MHz and 105 MHz RF are utilized, providing 10 ns and 9.5 ns pulse separation respectively.

While the multi–bunch mode is optimized for high intensity, the achievable temporal information in experiments is very limited. In current practice, no instrumentation using the timing of the light can be operated successfully in multi–bunch. Only timing–based instrumentation with external timing (such as pulsed extraction fields) can be operated.

The opposite approach to multi–bunch mode is to fill only one single bucket with electrons, which is referred to as single–bunch operation. In this mode the total intensity of the light is reduced because of the much lower ring current. This can be exemplified by the single–bunch mode at BESSY II in Berlin, Germany, which yields a total current of 20 mA, while the multi–bunch mode is run with ∼300 mA current [67]. Single–bunch operation is thus not attrac-

[1] This has been the standard operating mode for the MAX II [60] and MAX III [61] storage rings.

[2] The Touschek effect describes loss of electrons in the storage ring due to particle scattering. It is the major effect limiting lifetime of stored beams in typical modern storage rings [59].

| | Circumference [m] | Revolution period [ns] | Bucket separation [ns] | |
|---|---|---|---|---|
| MAX IV (3 GeV ring) | 528 | 1760 | 10.00 | [1] |
| MAX IV (1.5 GeV ring) | 96 | 320 | 10.00 | [1] |
| BESSY II | 240 | 800 | 2.00 | [68] |
| ALS | 196.8 | 656 | 2.00 | [69] |
| ASTRID2 | 45.7 | 152 | 9.52 | [65] |
| ESRF | 844.4 | 2817 | 2.82 | [70] |
| SOLEIL | 354.1 | 1181 | 2.84 | [71] |
| Spring-8 | 1436 | 4790 | 1.97 | [72] |
| SLS | 288 | 961 | 2.00 | [73] |

**Table 4.1.** *Relevant properties of some of the storage rings referred to in the text.*

tive for experiments where intensity is crucial. The temporal separation of light pulses is however much increased in single–bunch operation, as the repetition rate equals the revolution frequency of the electron bunch (large rings give low repetition rates, and vice versa). Where multi–bunch light had 2–10 ns between pulses, single–bunch increases spacing to hundreds of ns, or even several $\mu$s.

Some facilities do not use a single–bunch mode directly, but rather a "few–bunches" mode. For example the Advanced Light Source (ALS) at Berkeley, USA, regularly uses a two–bunch mode with 328 ns pulse separation. The European Synchrotron Radiation Facility (ESRF) in Grenoble, France, has opted for four–bunch and 16–bunch modes. Since these rings are very large, the few-bunch repetition frequency is still similar to single–bunch operation in smaller rings.

The single–bunch frequency is the hard limit for the lowest achievable repetition rate for a storage ring (provided no manipulation of the design orbit is performed). Instruments requiring repetition rates lower than ∼1 MHz, such as magnetic bottles and some ion–TOF instruments, require further manipulation of the light for their proper functioning. These "sub-single–bunch–requirements" can often be addressed by choppers or by exotic accelerator modes outlined below. The category of instruments benefitting from "single–bunch–requirements" includes most electron–TOF, among which one finds angle–resolved electron TOF instruments. Table 4.1 outlines the most important timing properties for selected storage rings.

There is a conflict between timing–based experiments, where low repetition rate is preferred, and experiments where high photon flux is desirable. In normal operation, it is also not possible to create single–bunch modes with pulse separations longer than the revolution period. Especially for small rings, these separations are often too short for timing–based spectroscopies.

## 4.2 Pseudo single bunch and resonant pulse picking

Operation in pseudo single bunch (PSB) is an attempt to simultaneously address requirements set by "photon–hungry" experiments and timing experiments. PSB has been implemented at the Advanced Light Source (ALS), USA [74–76], and at SOLEIL, France [77, 78]. A different approach has been developed at BESSY, Germany [79]. Both use additional components in the accelerator lattice to displace or excite electrons in one single bunch, causing some light to be emitted spatially or angularly separated from the light emitted by the other bunches. A collimator or aperture in the beamline allows only this intentionally misaligned light to pass.

PSB operation at ALS is based on the hybrid mode where the so called camshaft bunch is isolated from the bunch train by a 100 ns window. The PSB scheme involves a vertical displacement of the camshaft bunch by a fast kicker magnet. Light will be emitted spatially separated from the rest of the beam. The PSB scheme requires a short pulse, high repetition rate kicker magnet in the storage ring lattice. A sudden excitation from the magnet sends the camshaft bunch on a trajectory separated from the design orbit of the machine. The displaced bunch will have a vertical oscillatory motion relative to the design orbit. This implies that the vertical displacement of the camshaft bunch will be different for all insertion devices along the storage ring. The kicker magnet can be tuned to provide the maximum displacement in a specified insertion device, but not all beamlines can be served with PSB simultaneously. ALS has developed a "kick–and–cancel" scheme for PSB with a lower repetition rate than normal single–bunch [74, 76, 80]. In this scheme the camshaft bunch is kicked to a displaced orbit where it remains for some turns before it is kicked back to the design orbit. It is possible to make sure that the displaced bunch only passes the undulator once with a specific displacement. The PSB frequency, as seen by the beamline, can thus be decreased to any fraction of the single–bunch frequency; from hundreds of kHz down to a few Hz. The maximum repetition rate in this scheme is limited by the performance of the kicker magnet, currently 1.5 MHz, which is sufficient to make a kick every revolution at ALS [80]. The ability to create pulsed light with any fraction of the single–bunch frequency is very attractive to instruments with sub-single–bunch requirements. On the other hand, if the repetition rate can be made sufficiently high, it can also be an option for instruments requiring single–bunch light.

The approach implemented at BESSY uses a feature dubbed *pulse picking by resonant excitation* (PPRE) [79]. A single bunch on the design orbit is subject to a quasi–resonant excitation of incoherent betatron oscillations. The kick is provided by a stripline kicker, causing the bunch to increase its emittance. As the excited bunch passes an insertion device, light is emitted with much higher emittance than normal bunches. The outer rim of this beam can be separated with

an aperture. The excitation will be seen in all beamlines each revolution. Resonant pulse picking is thus a global feature, affecting the whole ring, compared to PSB which is localized to some beamlines. Since pulse picking at BESSY uses a stripline kicker similar to stripline kickers in the transverse bunch–by–bunch feedback system, a hybrid mode might not be required for this solution. This possibility has not yet been studied. The limiting factor is the rise and fall times of the stripline kicker and the required excitation magnitude, which is significantly smaller than in PSB operation. However, the ring must have transverse bunch–by–bunch monitoring abilities, i.e. the possibility to act on a single bunch in the bunch train.

The BESSY approach also has some benefits: The vertical dispersion is untouched and the vertical plane can be used as the dispersive plane for monochromatisation. Furthermore, the excited bunch light can be made to follow the beamline's optical axis if a small bump is provided in the accelerator lattice prior to the undulator. However, only a fraction of the light from the excited bunch is collected by the beamline, implying that resonant pulse picking provides much lower intensity than ordinary single–bunch light and it cannot be used in bending magnet beamlines[3].

The particular benefit of any PSB or PPRE operation is the combination of single–bunch–like light for some experiments, while others benefit from (almost) full intensity quasi-continuous light. The exact characteristics of the underlying hybrid mode must be carefully considered. For the ALS approach, a camshaft bunch must be sufficiently separated to allow the kicker magnet to act on it without inflicting on the orbit of other bunches. Both ALS and BESSY operate in hybrid modes where more than 15% of the total multi–bunch intensity is lost by the hybrid window. For small rings, where the single–bunch repetition rate is just a few hundreds of ns, it may not be possible to create a hybrid mode without losing a majority of the intensity.

## 4.3 Short pulses

The duration of a light pulse at a beamline is directly linked to the length of electron bunches in the storage ring. The so called natural bunch length is a property of the lattice parameters and the RF system [81]. The bunch length can be elongated by Landau cavities to increase lifetime and beam stability. In the last few years, however, many synchrotron radiation facilities have investigated and developed operation modes where very short pulses can be created in the storage ring. For timing–based instrumentation the precision by which the times can be determined is a significant contribution to the overall resolution of the instrument. If the light pulse is used as a

[3] Bending magnets emit light all the way along the arc of the bend. Consequently, a horizontal displacement will not be visible.

start trigger, the length of the light pulse translates to achievable resolution. It is thus of interest to keep bunch length limited compared to other sources of error, such as detector resolution and temporal broadening of monoenergetic particles in TOF instruments.

Most third generation storage rings with 500 MHz RF (or similar) have electron bunch lengths ranging from tens up to hundreds of ps (see table in Ref. [82]). At MAX IV, where bunch lengthening is applied in the storage ring to increase beam stability and lifetime [1], the effects of the several hundred picoseconds long bunches must be more carefully considered.

Short pulses are required in many kinds of time–resolved photoelectron spectroscopies (tr-PES). In these applications the short pulses are motivated by the time-scales of the physical and chemical dynamic processes under study. Requirements for time–resolved photoelectron spectroscopy using synchrotron radiation have been covered in a recent review by Yamamoto and Matsuda [82]. Their findings will not be repeated here.

There are different approaches to achieve short pulses in storage rings [83]. Many facilities use so-called "low–alpha optics" [84]. The length of these bunches can typically be reduced from tens of ps down to a few ps [85]. Ultra-short photon pulses in storage rings can also be created with femto–slicing techniques [86, 87]. Other possible solutions include using cavities and higher order RF systems to shorten bunches; a reversed, but similar operation to the bunch elongation performed by Landau cavities. However, such operation often leads to lower intensity of the light pulse. MAX IV Laboratory is currently establishing a so-called Short Pulse Facility [88] which will utilize the short electron bunches from the 3 GeV linear accelerator directly to create short (∼100 fs) hard x-ray light pulses in beamlines separated from the storage rings.

Pulse length in general is not a restriction for proper use of timing–based instrumentation at storage rings. While many attempts to reduce pulse lengths exist at storage rings, they are first and foremost aimed at time-resolved experiments covering short time dynamics, and there is no actual demand from the instrument point of view for shorter pulses. It should be noted however that it is often convenient to use time–of–flight based instrumentation in tr-PES because of their typically high transmission.

## 4.4 Choppers

Choppers are used to physically block or deflect undesired light in the beamline. The aim of a chopper at a storage ring is typically to transmit only one single light pulse[4]. Design of choppers is faced with a number of challenges: Transmission of a single pulse requires

[4] There are also chopper solutions where the aim is to transmit a bunch train of a specified length.

| | Type | Window [ns] | Rep. rate [kHz] | Sync. | |
|---|---|---|---|---|---|
| Plogmaker | Parallel (disc) | 750 | 9.7–78 | Yes | [92] |
| Ito | Perpendicular (hamster wheel) | 350 | 80.1 | No | [93] |
| ESRF | Perpendicular (tunnel) | 200 | 0–3 | Yes | [94] |
| Buffalo-1 | Parallel (disc) | 3520–2110 | 13.6–22.6 | Yes | [95] |
| McPherson | Perpendicular (tunnel) | 2450 | 2.7 | Yes | [96] |
| MHz pulse selector | Parallel (disc) | 141 | 1250 | Yes | [97] |
| DIAMOND | Parallel (disc) | 3700 | 0-0.05 | Yes | [89] |

**Table 4.2.** *Properties of some choppers, including their type (parallel or perpendicular), timing constraints and if they are synchronized to the light pulses.*

the opening time not to exceed twice the temporal distance between two adjacent pulses. If the chopper is used in hybrid modes, the opening time should be shorter than the hybrid window. Transmission of pulses should be repeated with a rate that ranges from single shots delivered on demand up to a few MHz. Another figure of merit for the chopper is its transmission, i.e. how much of the desired light is transmitted through the chopper during operation. To this end one must consider the beam size relative to the openings of the chopper, since transmission increases if the chopper can be placed where the beam is narrow. For efficient use at storage rings it should be possible to synchronize the chopper to the delivery of pulses. Each storage ring references their RF frequency to a timing signal in order to keep the buckets in phase within the ring; the ring (master) clock. A chopper's rotating element(s) can be continuously synchronized to the same reference. Recently developed choppers for storage rings have this ability. However, some jittering of the rotation frequency is always present. Inability to keep very precisely to the reference time hinder good performance.

In general, choppers can be divided into two groups: Those based on rotating absorbers and those based on rotating deflectors [89]. The latter works by means of deflection or diffraction of the beam by a rotating crystal [90] or mirror [91]. During rotation the light is repeatedly reflected onto a slit located at some distance (could be several meters) from the rotation axis. This type of chopper can be optimized for very short time windows (down to tens of nanoseconds). However, this requires a significant distance between rotation axis and the slit. If only one deflecting/diffracting surface is present the repetition rate is equal to the relatively low rotation frequency, which limits their applicability for instruments with single–bunch demands.

Absorption choppers have been enhanced during the last years. Table 4.2 shows performance data for some recent mechanical absorption choppers. These fall into two categories [98]; rotation axes aligned parallel or perpendicular to the beam (see Figure 4.4). The difference in performance was evaluated by Cammarata *et al.* [94]

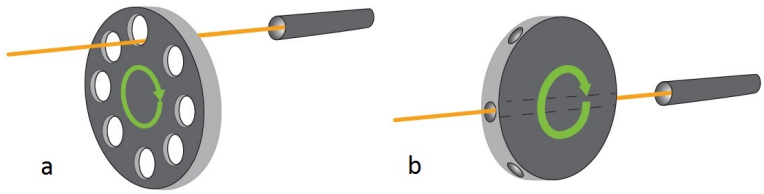


**Figure 4.4.** *Choppers of the (a) parallel and (b) perpendicular type.*

where it is pointed out that the perpendicular tunnel allows for a shorter time window than parallel slots for any given slot size. The limiting factor, both for repetition rate and window time, is the achievable rotation frequency. However, parallel choppers using rotating discs can host a much larger number of slots, increasing the possible repetition rate. The repetition rate for a slotted parallel chopper is given by the number of (equidistant) slots times the rotation frequency. The time window is limited by the width of the slots and achievable rotation frequency, while repetition rate is only limited by the number of slots.

A very favourable situation for synchrotron users would be if beamlines hosted a chopper capable of isolating one light pulse from an accelerator mode optimized for high–intensity light; hybrid or multi–bunch mode. Timing experiments could then be run in parallel with high–intensity–experiments. At present, no chopper can isolate one single bunch from a 500 MHz (or even 100 MHz) bunch train. However, some solutions exist where choppers are used to isolate camshaft bunches [94, 97]:

A chopper system for the beamline ID09B at ESRF was developed by Cammarata *et al.* [94]. ID09B is a hard x-ray beamline for time-resolved experiments in macromolecular crystallography and liquids. The system consists of three parts: A heat–load chopper, a millisecond shutter and a high–speed chopper. The high–speed chopper has a 300 ns opening window with 3 kHz repetition frequency, which is sufficient to isolate the camshaft bunch in ESRF's most common hybrid mode (the so–called "7/8+1") where one camshaft bunch resides within a 352 ns window in the multi–bunch train. Although this setup creates a single light pulse usable for sub-single–bunch instrumentation, 1 ms or more between pulses is far too long for efficient operation of electron spectroscopy instrumentation. To increase the pulse frequency to 100 kHz or more would not be possible with the used design due to mechanical restrictions of the rotating chopper.

The *MHz pulse selector* is to this day the only chopper capable to a repetition rate in the MHz range. The parallel slotted disc chopper was constructed for the BESSY storage ring to extract single bunches

from the hybrid mode at BESSY [97]; a camshaft bunch residing in a 200 ns window which is repeated every 800 ns (1.25 MHz) [99]. The chopper consists of a slotted disc, 338 mm in diameter, rotating at ∼1 kHz. The 1252 slots are 0.070 mm wide, allowing for a 70 ns window at the desired 1.25 MHz repetition rate. The chopper has ring clock synchronization. To withstand the large rotation speed, the outer edge of the disc is only 0.5 mm thick. This limits the chopper to soft x-ray and VUV, since the x-ray attenuation otherwise would be too small. The MHz pulse selector also is the chopper with the shortest time window.

Choppers are only a possible solution to single–bunch or sub-single–bunch instrumentation if a hybrid mode exists. Many larger storage rings have hybrid modes, but smaller storage rings with large hybrid windows would significantly loose intensity. Beside hybrid mode extraction, many choppers have been developed for simply lowering the single–bunch (or few–bunch) frequencies to better suit sub-single–bunch instrumentation. These choppers have lower requirements both concerning window opening and repetition rate, and simpler designs can be utilized. One chopper scheme for sub-single–bunch use has been designed by Plogmaker *et al.* [92] and is currently in use at BESSY. The principal design aim of this chopper is to decrease the pulse frequency from 1.25 MHz in BESSY single–bunch mode to 10–100 kHz, a frequency suitable for the magnetic bottle spectrometer. They utilized a solution with two spinning discs mounted on a joint axis. Each disc has a set of equally spaced apertures along the periphery of the disc. The discs can be rotated relative to one-another and thus the effective opening, as defined by the overlap of the apertures, can be changed. From this setup they managed to extract a single light pulse at 9.7 kHz and 78 kHz respectively while BESSY operated in single–bunch mode. The authors also report that they have created $\mu$s bunch trains from a multi–bunch source, and point to the future possibility to use the chopper in hybrid–bunch extraction at BESSY, although this would require an opening window smaller than 200 ns.

## 4.5 Opportunities

High–brilliance storage rings offer new opportunities for the spectroscopy user communities. While many new technologies exploit timing–based instrumentation at storage rings, the challenge remains how to combine these developments into useful solutions. Great over-all benefits can be achieved if high intensity experiments and timing–based instrumentation can be run in parallel. Single–bunch modes are successfully implemented at many storage rings but constitute a great intrusion to other types of experiments. Single–bunch modes also differ in usability depending on the size of the storage ring. The greatest opportunity for timing–based instrumen-

tation at storage rings are those accelerator and chopper schemes which allow the storage ring to be run with high current and deliver high intensity light at the same time as single–bunch light can be delivered on demand at certain experiments. The recent development of a MHz chopper which allows picking a single–bunch pattern from a hybrid mode is a significant achievement. The MHz pulse picker is limited only by the availability of a suitable hybrid mode. Current MHz chopper reports a window limit below 100 ns, which excludes its use with hybrid modes at very small rings. However, schemes to reduce the repetition rate of single–bunch modes at these rings can be useful for some instrumentation.

PSB and resonant pulse picking holds similar promises as MHz choppers; the possibility to create simultaneously single–bunch operation for some beamlines and high intensity for others. The work done at BESSY and ALS show that different approaches exist and have proven successful. Depending on chosen solution, it can to some extent be adapted to single–bunch or sub-single–bunch requirements. The approach is however more intrusive on the machine, and disturbances to beam stability must be carefully considered. The necessity of a hybrid mode and the size of the hybrid window is determined by the mode of excitation and the kicker performance.

Recent theoretical and experimental investigations at MAX IV Laboratory has highlighted how the use of passive Landau cavities in the ring lattice hinders, or at least complicates, the use of single–bunch modes and hybrid modes. As Landau cavities are an integral and essential part of the MAX IV accelerator concept, and many existing laboratories with timing capabilities has opted to implement similar lattices in order to reach low–emittance, there is a potential risk that such modes may suffer from the lattice upgrade. In this regard, PSB and resonant pulse picking have a particular advantage since they involve displacement or excitation of charged bunches rather than making a gap in the filling pattern. These potential benefits and threats should be carefully considered at MAX IV, as well as other facilities undergoing lattice upgrade.

CHAPTER 5

# GATING AN ANGLE–RESOLVED ELECTRON TIME–OF–FLIGHT SPECTROMETER

## 5.1 Electron time–of–flight spectrometers and their requirements for timing

Two types of electron spectrometers dominate at brilliant VUV and X-ray light sources: Hemispherical deflector electrostatic analysers (HDA) and time-of-flight (TOF) based analysers [100]. The fundamental difference is their means to analyse the energy of the electron. The hemispherical analyser records the *spatial* dispersion of electrons with different energies traveling through an electrostatic field. The TOF–system on the other hand measures the *time* it takes for the electron to travel from the sample to the detector, i.e. the electron speed. Both TOF and hemispherical analysers become more sophisticated by the introduction of imaging detectors which provide information on the position where the electron hits the detector plane; this is in addition to the detection of the time [100]. Introducing an imaging detector in the field-free TOF–system gives the possibility to record directions of movement as a function of hit positions. Angular directions $[\theta, \phi]$ (see Figure 5.1) can be uniquely determined from detector positions $[x_{\text{det}}, y_{\text{det}}]$. This feature is exploited e.g. in COLTRIMS [101].

Electron TOF (eTOF) was first developed and used by Bachrach *et al.* at SPEAR [102]. An important eTOF instrument was later developed by Hemmers *et al.* [103] which has served as a model for many types of eTOF currently in use at storage rings and free electron lasers (see e.g. Refs. [104, 105]). These eTOFs use a compact design where electrons fly through a field–free tube, preceded by a short electrostatic lens. The energy resolution is limited by the use of a field–free drift region, but the concept has often been applied in coincidence setups due to its relatively high transmission. Several types of eTOF

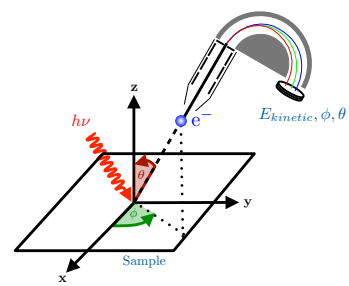


**Figure 5.1.** *Angles of emission from a sample as they are defined in an ARPES experiment. $(x, y, z)$ in this case is the Cartesian coordinate system with reference to the sample and should not be confused with the detector coordinates defined with reference to the detector surface.*

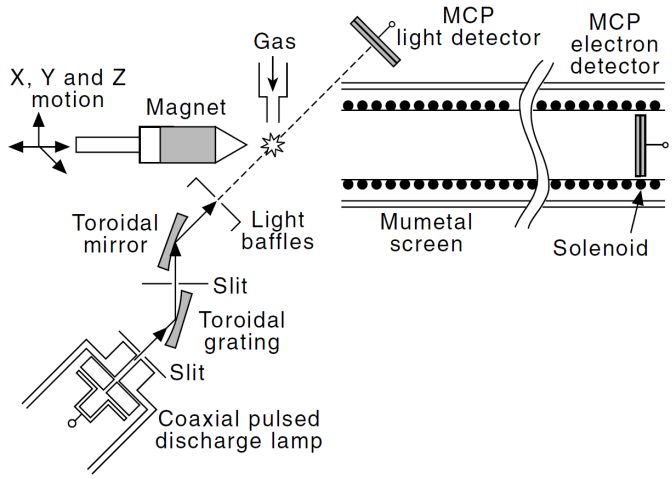


**Figure 5.2.** *Schematic drawing of the magnetic bottle spectrometer developed by Eland et al. [109]. The prolonged flight time and high collection efficiency stems from the solenoid magnet surrounding the drift tube, in combination with the conical permanent magnet placed close to the interaction region. (©John Eland, Department of Chemistry, Physical and Theoretical Chemistry Laboratory, Oxford University. Reproduced with permission.)*

instruments exist on the market today. The instruments manufactured by *VG Scienta AB* – Scienta ARTOF 10k and Scienta ARTOF-2 [106, 107] – are used for the work presented in Papers **VI**, **VII** and in Chapter 5. Since all instruments differ in geometry and properties, only part of the discussion is applicable to other TOF lens solutions such as e.g. the THEMIS spectrometers manufactured by *Specs GmbH* [108]. As flight-times are in the 1 $\mu$s range, light emitted with the single–bunch frequency of many storage rings ($\sim$ 1 MHz) provides in most cases suitable time structure for eTOF–experiments.

There are many practical problems associated with the field–free TOF–system. Electrons are light particles and will reach very high speeds even at modest kinetic energies. Therefore the time-resolution of the light source and the detector must be very high. In addition, with high speed electrons the acceptance of the analyser is reduced to a very small solid angle [100]. To avoid this problem, flight times must be increased; either by increasing the length of the flight path or by reducing the electron speed in a predictable manner. A solution using the former approach is the magnetic bottle spectrometer [109–111] which is a time–of–flight electron spectrometer where electrons are collected by an inhomogeneous magnetic field and their flight–times prolonged by means of a long solenoid magnet.

A schematic picture of a magnetic bottle spectrometer is displayed in Figure 5.2. As the electrons are made to perform helical motion around the magnetic field lines of the solenoid magnet, their travelled distance increases, and therefore also their time–of–flight. That increases energy resolution and collection efficiency. A conical permanent magnet pole close to the interaction region guides electrons into the spectrometer. The magnetic bottle spectrometer is particularly well suited for electron coincidence experiments; recently even for experiments with simultaneous electron and ion detection [112]. However, no position or angular information can be extracted from data. The long flight–times, several $\mu$s [109, 113], put hard restrictions on the repetition rate of the light source. These flight–times are considerably longer than the single–bunch frequency of typical storage rings. A shorter spectrometer can be constructed to reduce the flight–time, at the expense of resolution [114]. For fast electrons the pulse length can become the limiting factor for achievable energy resolution. Eland *et al.* used a 20 ns pulse during home lab experiments and noted that energy resolution was limited by the light pulse for electron energies above 20 eV [109]. Typical pulses from a storage ring are significantly shorter.

## 5.2 The angle–resolved time–of–flight (ARTOF) instrument

It is in principle possible to remove the hemispherical analyser and use the time-of-flight in the lens for energy discrimination. Instead of focusing electrons to a slit, the electrons can be focused on a detector surface. Wannberg [100] shows that for angle-resolving lens, there is a correlation between measured time-of-flight ($t$) and detector position ($x_{\mathrm{det}}, y_{\mathrm{det}}$) on one hand, and electron energy ($E_{\mathrm{kin}}$) and take-off angles ($\theta, \phi$) on the other. One can define a transformation matrix where the conversion is a three dimensional function [106][1]

$$E_{\mathrm{kin}} = E_{\mathrm{kin}}(x_{\mathrm{det}}, y_{\mathrm{det}}, t) \quad (5.1)$$

$$\phi = \phi(x_{\mathrm{det}}, y_{\mathrm{det}}) \quad (5.2)$$

$$\theta = \theta(x_{\mathrm{det}}, y_{\mathrm{det}}, t) \quad (5.3)$$

This constitutes the basis for Wannberg's proposal for an angle-resolved time–of–flight system which was realized as the ARTOF spectrometers. The ARTOF instrument is depicted in Figures 5.3 and 5.4. The lens design takes its starting point in the lens used for the hemispherical electron analyser Scienta SES-200 [115]. This lens was cylindrically symmetric and consisted of five lens elements [116]. It could operate in angle–resolved and imaging modes. Figure 5.4 shows a schematic drawing of the five lens elements of the ARTOF lens and a simulation of electrons traveling through the lens

[1] The original article contains a typographical error in this equation.

**Figure 5.3.** *The ARTOF 10k. (©VG Scienta AB. Reproduced with permission.)*

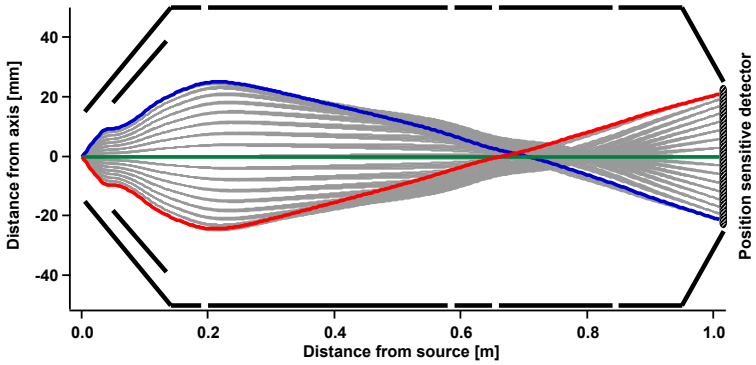


**Figure 5.4.** *Schematic illustration of typical flight paths for electrons through the ARTOF lens. Here, the instrument works in angle–resolved mode (angle–to–point). It is obvious that monoenergetic electrons traveling on the outer paths have longer flight times than on–axis electrons.*

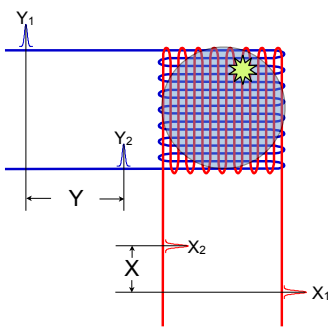


**Figure 5.5.** *Schematic depiction of the delay–line detector from above. Impinging electrons create an MCP avalanche which induces a signal on the delay-lines. The signal travels in both directions through the meandering delay-line and can be picked up by a TDC. The relative timing of the two signals determines the hit position on the detector. Two delay-lines give the position in two dimensions.*

in angle resolving mode. In this mode the electrons are distributed on the detector according to their emission angle. Electrons follow quite complicated trajectories which must be calculated using electrostatic simulations. It should be noted that a parallel–to–point transformation takes place early in the lens and a focal plane is created. This focal plane is imaged to the detector with the remaining part of the lens [100].

The lens accepts electrons in a selected energy window, typically 10% of the centre energy. Due to chromatic aberrations, the resolution of the instrument decreases as energies depart far from the centre energy; the transformation matrix becomes degenerate and an assignment of electron energies is no longer possible. The ARTOF allows detection of electrons within a ±15°emission cone. The transmission of the instrument is thus much higher than for hemispherical analysers at comparable energy resolution. The ratio can be estimated by comparing the area of a circle with diameter equal to the length of the entrance slit to the area of the same slit [107]. For high resolution experiments, where the hemispherical analyser entrance slit would typically have a very narrow width, this can imply up to 300 times increase in transmission. Electrons entering the lens are retarded to prolong flight time, and to increase energy resolution. The lens also acts as an energy filter where low energy electrons are not accepted.

A *RoentDek* position–sensitive delay–line–detector is utilized for time and position detection. A 40 mm Chevron-stacked MCP precedes the delay lines (Figure 5.5). Position is determined by comparing relative times of the signals from the delay–lines. The detection time can be determined either by the MCP-signal or by the mean ar-

rival time of the delay–line pulses. The MCP signal is, however, the most precise due to its short rise time. In total the detector produces five signals which are preamplified outside vacuum. The signals are sent to constant fraction discriminators (CFDs) where they are transformed to NIM-pulses[2]. The pulses are fed into a time-to-digital converter (TDC) from which they can be read by the computer. The timing at the detector is critical for the instrument; energy resolution is related to time resolution in a complicated way, but can be estimated using the formula [107]

$$\Delta E = \sqrt{(\alpha E^{3/2} \Delta t)^2 + (\beta \Delta d^{\gamma} E)^2} \tag{5.4}$$

where $\Delta t$ and $\Delta d$ are the time-resolution for the electronics and the detector, and $\alpha, \beta, \gamma$ are properties of the transformation matrix for the selected centre energy $E$.

To assure ultimate resolution, the sample must be placed in the focal spot of the lens which is situated along the ARTOF axis at a predetermined distance from the first lens element. This implies that the ARTOF axis, the light beam and the sample must coincide in one point in space. The ARTOF must also be calibrated to the timing of the light source. If the ARTOF is used with a suitable pulsed light source (storage ring in single–bunch mode), the acquisition should be synchronized to its internal time reference (ring clock). Scattered photons from the sample or sample holder can be used as an absolute time–stamp.

The high transmission and data acquisition rate gives rise to extensive amounts of data. Each event is stored as a vector with the $x$, $y$ and $t$ coordinates. The analysed data is consequently stored as a vector with $E$, $\phi$ and $\theta$ coordinates. The initial analysis can be performed with software provided by the manufacturer. In addition, we have used a set of scripts developed within the ARTOF project to analyse data, for example, in **k**-space. These extensions provide means of analysis for ARPES and other applications.

For applications in electron spectroscopy, the benefits of ARTOF stem primarily from its high transmission in combination with high energy resolution. A good overview of ARTOF application areas is given in Ref. [107]. The ARTOF allows mapping of the whole momentum space in three dimensions (3D-ARPES). For example, the study by King *et al.* [117] shows 3D-ARPES on $Bi_2Se_3$. In this study, the sample was cleaved and the evolution of band structure was studied in real time. ARTOF also opens up for experiments with very low radiation doses: In single–bunch modes, the sample is irradiated with a much lower mean intensity. This would typically be a drawback since fewer electrons are emitted, but this is rather a benefit for radiation sensitive samples. A study by Vollmer *et al.* presents results

[2] The Nuclear Instrument Module (NIM) is a standard set of specifications for electronic modules. The standard also specifies levels for logic signals and associated equipment.

of low dose spectroscopy on organic crystals (rubrene). Here, photon flux was kept at $10^8$ photons/s, and still the band structure could be obtained in 20 minutes [118]. An ARTOF instrument has also been used for pump–probe experiments together with a laser source [119]. High transmission is beneficial since repetition rates are low for high laser energies.

In summary, ARTOF instruments have in a short time found application areas where hemispherical analysers previously were the only viable alternative. Especially the high transmission compared to other high resolution instruments benefits the whole user community. These two classes of electron analysers are, however, complementary and can both be widely applied at storage rings.

## 5.3 Gating principles

The purpose of an electron gate is to block unwanted electrons from reaching the detector. While the accelerator modes and choppers outlined in Chapter 4 aim to prevent interaction between light and sample, instrument gating affects unwanted electrons *after* the interaction. The goal is to allow only electrons originating from certain interaction events to reach the detector. The benefit of electron gating compared to light choppers is that electrons can be very easily deflected using electric and magnetic fields, as they are light, charged particles. Creating pulsed electromagnetic fields with fast rise times and high repetition rates is much easier than any physical blocking with the same temporal properties. The complication is to create a gate which is efficiently rejecting unwanted electrons while leaving accepted electrons undisturbed. Even slight field errors can introduce large deviations in electron speed and direction. Also, the gating must be introduced when the temporal dispersion of the electrons has not yet exceeded the repetition rate of the incoming light. Otherwise, it will not be possible to distinguish between electrons created in subsequent events. To achieve high selectivity, the gate should be close to the sample. On the other hand, the effect of field errors is minimized if the gate is close to the detector; these conditions are unfortunately contradictory.

Some experiments have been reported where detector gating has been used to study time–resolved effects on semiconductor surfaces [120–123]. In these pump–probe experiments, the detector gate is synchronized with the laser to allow detection of electrons emitted from the relevant probe. In a study by Takahashi *et al.* [123] a detector gate was used in a hemispherical analyser to gate electrons with ∼10 eV kinetic energy. They report using a 5–6 V gating pulse, 50 ns long, applied to the front side of the MCP. They achieve 5 ns opening and closing time of the detector[3]. In a similar experiment,

[3] The total 10 ns gate time makes this a possible solution for 100 MHz storage rings such as MAX IV. The gate time is considerably smaller than chopper opening times.

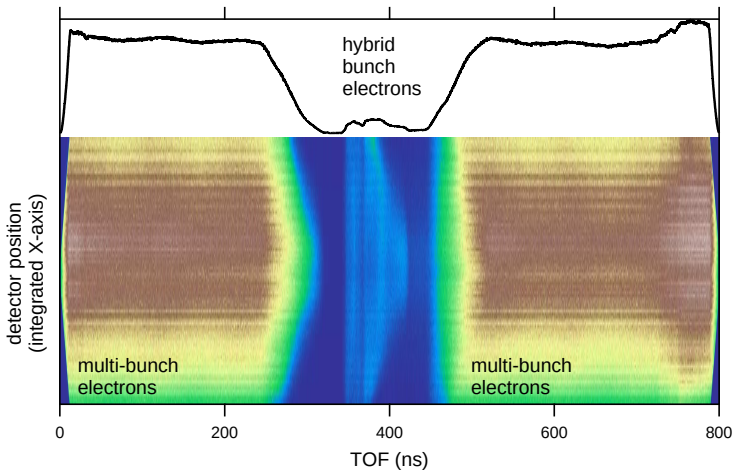


**Figure 5.6.** *Typical time–of–flight spectrum acquired in hybrid mode at BESSY. The graphene valence band is measured with $h\nu = 180$ eV and the instrument optimized for recording $E_{kin} = 175$ eV. Electrons generated by the hybrid bunch are clearly separated from the multi–bunch electrons by the 216 ns hybrid window.*

they applied a gate pulse to the sample area to induce an electric field dependent energy shift to the emitted electrons. Those electrons emitted while the gating pulse was applied will arrive at the detector with lower kinetic energy and become distinguishable from electrons emitted at a different time.

ARTOF gating is proposed as a tool at storage rings lacking the required pulse separation. The ARTOF has flight–times for analysable electrons spanning from a few hundred ns up to 3 $\mu$s [106]. Due to scattered photons and high energy electrons from higher order light, a single light pulse can be expected to give rise to detection signals in a time-range starting from a few ns (photons) up to microseconds.

The temporal properties of the light source determines which gating solutions can be applied. Figure 5.6 shows a TOF spectrum acquired at BESSY when it was operated in hybrid mode. The electrons generated by the hybrid bunch arrive at the detector temporally separated from the electrons generated by the multi–bunch train. Most detections are unresolvable. Under these circumstances, the electron spectrum can be analysed from the hybrid electrons and all other electrons can be disregarded. However, it is disadvantageous to have a large background of undesired electron detections which overload the MCP detector. Hence, the acquisition time for an electron spectrum increases by more than an order of magnitude compared to single–bunch operation. A pulsed electric field can be in-

However, the applied pulse amplitude is low and limits its applicability.

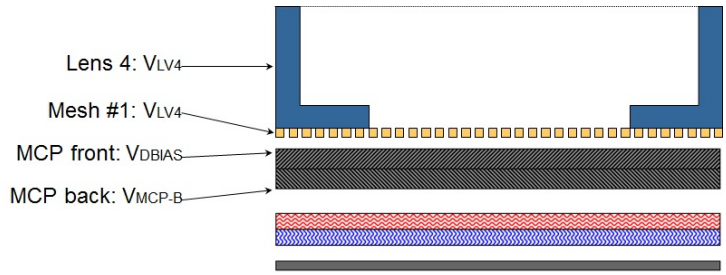


**Figure 5.7.** *Schematic side-view of the delay line detector in its original setup. Electrons impinge on the mesh from above. The lens axis is normal to the mesh.*

troduced close to the detector which rejects the multi–bunch electrons. This forms the basis for the studies on detector gating in Section 5.4 and Paper **VI**. The detector gating scheme is applicable for hybrid modes where the temporal dispersion of hybrid electrons fits within a sufficiently large window. It cannot be applied directly under multi–bunch conditions, or when the temporal dispersion exceeds the hybrid window. The latter problem arises for detection of very slow electrons. Alternatively, gating can be performed prior to the lens. The temporal dispersion increases as an electron travel through the lens; therefore an early gate allows removing electrons originating from light pulses with short temporal separation. This is the basic idea for our studies on front gating in Section 5.5 and Paper **VII**. This is required if gating should be possible in any multi–bunch operation, like the 100 MHz operation at MAX IV.

## 5.4 Detector gating

The detector gating scheme is one of the two realisations of ARTOF gating which have been explored within the ARTOF development project. The detector gate solution, also called the *Gated ARTOF Modular Extension (GAME)*, was developed particularly for BESSY hybrid mode operation. We have presented our successful operation of the GAME in Paper **VI**. The design was made in collaboration with *VG Scienta AB* in 2012 and was implemented and tested at BESSY during 2013 and 2014.

### 5.4.1 Physical design

The ARTOF uses a commercial delay-line detector from *RoentDek GmbH*, consisting of two Chevron stacked MCP plates followed by two delay lines and an anode. As noted previously, an electron hitting the detector generates five signals, one from the MCP stack and

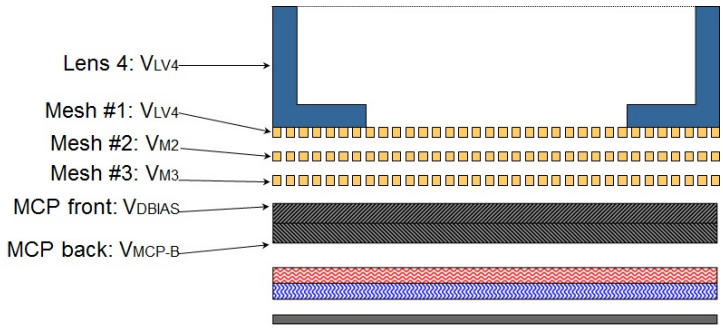


**Figure 5.8.** *Schematic side-view of the delay line detector with added gating meshes. The MCP and delay-lines have been moved 20 mm further away from the lens.*

one signal from each end of the two delay-lines. In non-gated operation, the MCP signal provides the arrival time of the electron, while the hit position is deduced from the delay-line signals. Figure 5.7 shows the non-gated detector where the MCP stack is preceded by a gold mesh kept to the same potential as the last lens element of the electron lens. We introduced two additional meshes between the last lens element of the analyser and the MCP, depicted in Figure 5.8. This operation moved the MCP and delay-lines to a position further away from the source point (where the light interacts with the sample). Both meshes were connected in vacuum to a voltage feed-trough. A high–voltage source, identical to the power supplies commonly used for the lens elements of the ARTOF, feeds the tuneable negative potential $V_{\mathrm{nej}}$ to the M2 mesh that acts as an energy filter and allows passage of only the electrons with kinetic energies higher than $-q\,V_{\mathrm{nej}}$. To achieve gating, a pulsed gating potential $V_{\mathrm{gate}}$ sufficient to deflect all electrons is introduced. The gate characteristics are altered by changing the potential $V_{\mathrm{nej}}$ as well as the gating pulse length, amplitude and repetition rate. For pulse generation we use a ±10 V function generator which is coupled to M2 through a high-capacitance capacitor (Figure 5.9). The circuit acts as a high-pass filter, adding the pulse as a variable signal on top of the constant $V_{\mathrm{nej}}$ potential. Electrons with lower kinetic energies will always be deflected by the gate if a sufficient $V_{\mathrm{nej}}$ potential is applied. By this scheme, the mesh can be made into an efficient gate for electrons with energies between $-q\,V_{\mathrm{nej}}$ and $-q(V_{\mathrm{nej}}+V_{\mathrm{gate}})$. Using a pulse generator with small amplitude makes the instrument simple and limits the effect of the read-out of the detector. Nevertheless, electrons with higher kinetic energies will not be gated by this scheme. These electrons are most often easy to recognise since they are faster and arrive earlier to the detector than electrons within the energy window. A problem with high energy electrons arises when fast electrons from

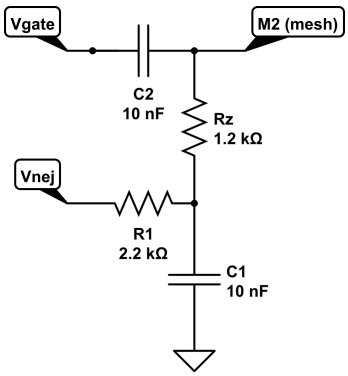


**Figure 5.9.** *Circuit feeding the potential $V_{nej}$ and the gate pulse $V_{gate}$ to the M2 mesh. The signal is transmitted through the C2 capacitor, acting as a high pass filter.*

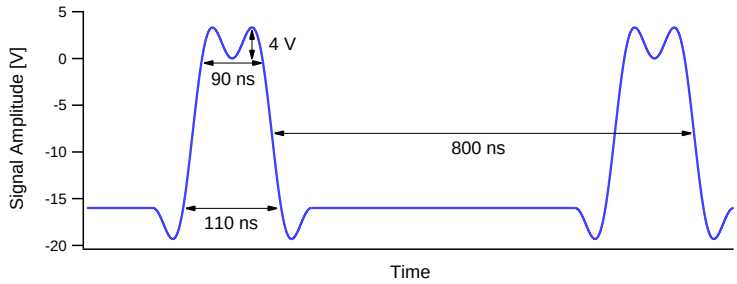


**Figure 5.10.** *Custom made gate pulse with 20 V amplitude as defined in equation (5.5). Each of the pulses is triggered by the 1.25 MHz ring clock signal. Since the full width of the gate pulse is shorter than 800ñs, the intermediate space is filled by a constant negative potential which keeps the gate closed. As indicated, we achieve a 90 ns fully open window with 10 ns rise and fall times. The oscillation of the gate function has 4 V amplitude at 20 V gate potential.*

the multi–bunch train overhauls the preceding electrons before detection[4]. This is a fundamental restriction to the GAME and could only be practically solved by increasing the gate amplitude or making the hybrid window longer in the storage ring.

### 5.4.2 Electronic pulsing

A pulsed electric potential very close to the detector introduces disturbances to the signal readout. In normal operation of the detector, the timing signal is read from the potential drop occurring when an electron impinges on the MCP surface and causes an electron avalanche. The amplitude of this signal is several orders of magnitude lower than the amplitude of the gate pulse. Considering that the mesh assembly acts as a parallel plate capacitor, it is obvious that high frequency signals on M2 will extend to the neighbouring meshes and the MCP. Even if only a fraction of the signal is transmitted, its high amplitude will overshadow the true MCP signal and prevent its use. In some cases false signals could be introduced also at the delay-lines. To circumvent this problem we took a number of steps and precautions:

- The time-of-flight cannot be extracted from the MCP, but could be deduced from the combined detection of four delay line signals. Since the delay lines have a fixed length, the total delay of the two signals in each line is constant. Therefore, the mean arrival time of the four DLD signals has a constant delay to the

[4] In operation at the beamline we always expect higher-order light to create fast electrons.

time of detection. In the present detector setup the timing resolution of the delay lines is slightly worse than the MCP signal (a few hundred ps). However, changing from MCP to DLD timing has implications on the internal logic of the experiment since the MCP signal normally is used as start time trigger for the DLD signals. To facilitate a pure DLD operation, we had to develop MCP-signal-independent data acquisition schemes.

- The M3 mesh was inserted as a shield for the detector. A large grounded element between the pulsed mesh and the MCP avoids extensive transmission of signal to the detector. M3 was grounded through a short in-vacuum coaxial cable connecting the mesh and the grounded vacuum feed–through.

- The gating pulse was shaped to minimize the crosstalk between M2 and neighbouring meshes. Figure 5.10 shows the pulse at its maximum amplitude. The pulse should have few high frequency Fourier components to avoid transmission of signals to the MCP. After a trial including eight Fourier components, a function only including first and third order components was selected for producing the pulse:

$$V(t) = \frac{2V_{\text{gate}}}{\pi}\left(\sin\frac{\pi t}{150\,\text{ns}} + \frac{1}{3}\sin\frac{3\pi t}{150\,\text{ns}}\right) - \frac{V_{\text{gate}}}{2} \tag{5.5}$$

where $t$ is an arbitrary time parameter. The pulse was set to trigger on the signal from the ring and run for one period before settling on a constant negative potential. The signal was repeated with 1.25 MHz repetition rate (the single bunch frequency at BESSY). The highest frequency component in this function is 10 MHz; this was found to allow operation with $V_{\text{gate}} = 20\,\text{V}$ and DLD referencing. The function with eight components can be used for similar operation, but only up to $V_{\text{gate}} < 10\,\text{V}$. The custom-made gate pulse has approximately 10 ns rise and fall time, which is sufficient for most applications.

### 5.4.3 Time-of-flight errors induced by detector gating

Consider an electron emitted from the sample with kinetic energy $U_0$. The sample is grounded, i.e. sample potential $V_{\text{sample}} = 0\,\text{V}$. The electron kinetic energy at any given point with potential $V$ is

$$U_{\text{kin}} = U_0 + qV \tag{5.6}$$

where $q$ is the unit charge[5]. While traveling through the lens, any point with potential $V < U_0/q$ is unreachable for the electron. Thus,

[5] Note that the electron is a negatively charged particle with charge $-q$.

when the detector is surrounded by a volume where $V_{\text{gate}} < U_0/q$, the electron cannot reach the detector.

A schematic picture of the original setup of the detector is given in Figure 5.7. The gold mesh is kept in physical contact with the last lens element of the ARTOF lens, and thus shares the same potential. A potential $V_{\text{LV4}}$ is fed to the last lens element. A strong positive potential $V_{\text{DBIAS}}$ is fed to the MCP. The mesh and the MCP are parallel surfaces, producing a homogeneous electric field

$$\mathbf{E} = -\frac{V_{\text{DBIAS}} - V_{\text{LV4}}}{d_0} \cdot \hat{\mathbf{r}} \tag{5.7}$$

where $d_0$ is the distance between the potential surfaces and $\hat{\mathbf{r}}$ is the spatial unit vector along the lens axis. To determine the electron's time-of-flight through the detector, i.e. from the mesh to the MCP, we have to consider the electron's speed at the mesh

$$v = \sqrt{2U_{\text{kin}}/m} = \sqrt{2(U_0 + qV_{\text{LV4}})/m} \tag{5.8}$$

and the impinging angle $\theta$ relative to the lens axis. The electron will be accelerated by the **E**–field before reaching the MCP. Due to the direction of the field vector along the lens axis, the velocity component $\mathbf{v}_{\parallel}$ parallel to the lens axis will increase while $\mathbf{v}_{\perp}$ remains unchanged.

To find an approximate value of the impinging angle $\theta$ we can consult published particle trajectories [106]. Figure 5.4 suggest that electrons, before reaching the detector, pass through an intermediate focus approximately 200 mm from the detector prior to traveling on almost straight lines to the detector with 20 mm radius. This corresponds to a maximum impinging angle $\theta_{\text{max}} \approx 0.1$ rad. This small angle justifies the approximation $|\mathbf{v}| = |\mathbf{v}_{\parallel}|/\cos\theta \approx |\mathbf{v}_{\parallel}|$. Therefore, for the time-of-flight calculation, we can regard the electron as impinging parallel to the lens axis.

The time-of-flight of a charged particle in a homogeneous electric field is well known [124].

$$t = \frac{\sqrt{2m(U_{\text{kin}} + qEd_0)}}{qE} - \frac{\sqrt{2mU_{\text{kin}}}}{qE}. \tag{5.9}$$

Substituting equation (5.6) and equation (5.7) in equation (5.9), and setting $d = d_0$, the non-gated case becomes

$$t_{\text{nogate}} = \frac{\sqrt{2m(U_0 + qV_{\text{DBIAS}})} \cdot d_0}{q(V_{\text{DBIAS}} - V_{\text{LV4}})} - \frac{\sqrt{2m(U_0 + qV_{\text{LV4}})} \cdot d_0}{q(V_{\text{DBIAS}} - V_{\text{LV4}})}. \tag{5.10}$$

The gated detector, pictured in Figure 5.8, has been extended with two additional meshes. The first mesh (M1) still maintains a physical connection to the last lens element. The MCP has been moved 20 mm back from its original position. Since the length of the flight paths through the detector is increased, and the gate includes decelerating elements, the time-of-flight, $t_{\text{gate}}$, must be larger than

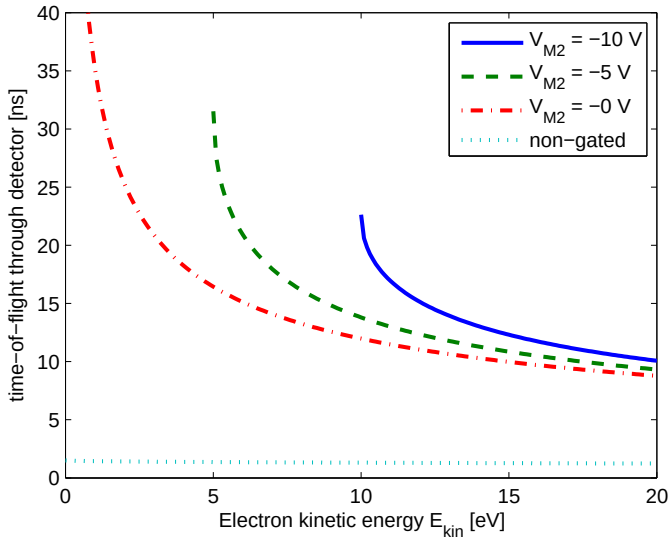


**Figure 5.12.** *Time-of-flight for electrons with a range of kinetic energies $E_{\mathrm{kin}}$ traveling through the gated detector with different gating potentials. $V_{\mathrm{M2}} = 0$ V correspond to the field free case. Note the sharp edges at the cut-off potentials.*

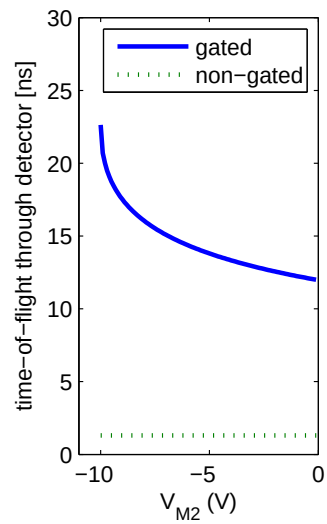


**Figure 5.11.** *Time-of-flight for 10 eV electrons traveling through the gated detector (blue) for different potentials $V_{\mathrm{M2}}$ on the gating mesh M2. The time-of-flight for 10 eV electrons in the non-gated detector is given for reference (green).*

$t_{\mathrm{nogate}}$. This increased flight-time must be considered while processing the measured data.

The gated detector produces three regions of homogeneous electric fields separated by the meshes. We can apply equation (5.9) to each region. Using the notation given in Figure 5.8 we have

$$\begin{aligned} t_{\mathrm{M1-M2}} &= \frac{\sqrt{2m(U_0+qV_{\mathrm{M2}})}\cdot d_1}{q(V_{\mathrm{M2}}-V_{\mathrm{IV4}})} - \frac{\sqrt{2m(U_0+qV_{\mathrm{IV4}})}\cdot d_1}{q(V_{\mathrm{M2}}-V_{\mathrm{IV4}})} \\ t_{\mathrm{M2-M3}} &= \frac{\sqrt{2m(U_0+qV_{\mathrm{M3}})}\cdot d_2}{q(V_{\mathrm{M3}}-V_{\mathrm{M2}})} - \frac{\sqrt{2m(U_0+qV_{\mathrm{M2}})}\cdot d_2}{q(V_{\mathrm{M3}}-V_{\mathrm{M2}})} \\ t_{\mathrm{M3-MCP}} &= \frac{\sqrt{2m(U_0+qV_{\mathrm{DBIAS}})}\cdot d_3}{q(V_{\mathrm{DBIAS}}-V_{\mathrm{M3}})} - \frac{\sqrt{2m(U_0+qV_{\mathrm{M3}})}\cdot d_3}{q(V_{\mathrm{DBIAS}}-V_{\mathrm{M3}})} \end{aligned} \tag{5.11}$$

where $d_1, d_2, d_3$ are the lengths of each of the regions (the distances between the meshes). Summing up the flight times gives the total time-of-flight between the last lens element and the MCP detector.

$$t_{\mathrm{gate}} = t_{\mathrm{M1-M2}} + t_{\mathrm{M2-M3}} + t_{\mathrm{M3-MCP}}. \tag{5.12}$$

To calculate the increase in flight time induced by the gate we need to evaluate the difference $\Delta t \equiv t_{\mathrm{gate}} - t_{\mathrm{nogate}}$. A gate setup with $d_0 = d_1 = d_2 = d_3 = 10$ mm could be used as a benchmark to estimate the magnitude of $\Delta t$. We apply a high positive potential on

the MCP ($V_{\mathrm{DBIAS}} = +500$ V), and keep all other potentials to ground. Then $t_{\mathrm{gate}} = t_{\mathrm{M3-MCP}}$ and the increase in flight-time equals the field-free flight from M1 to M3 in the gated detector.

$$\Delta t = \frac{2d}{\sqrt{2U_{\mathrm{kin}}/m}} \tag{5.13}$$

For $U_{\mathrm{kin}} = 10$ eV, a typical kinetic energy for an electron impinging on M1, we find $\Delta t = 10.6$ ns. This is a significant increase in flight time.

In real gating, one might want to decrease the kinetic energy even further with the gating mesh (M2). A potential $V_{\mathrm{M2}} = -5$ V on M2 adds an additional 2 ns to the flight time. Figure 5.11 illustrates the increasing time-of-flight as a stronger deflection potential on M2 is introduced. As the deflection potential approaches the cut-off potential the increase in time-of-flight rises above 20 ns.

The perpendicular component $\mathbf{v}_{\perp}$ of the electron velocity is not affected by the electric fields. Nevertheless, the final position on the detector is indeed affected due to the increased flight-time. This spatial change is determined by

$$\mathbf{r}_{\mathrm{gate}} - \mathbf{r}_{\mathrm{nogate}} \equiv \Delta\mathbf{r} = \mathbf{v}_{\perp} \cdot \Delta t \tag{5.14}$$

where $\mathbf{r}_{\mathrm{gate}}$ and $\mathbf{r}_{\mathrm{nogate}}$ are the hit positions on the detector in the gated and non-gated case, respectively. Reviewing again the trajectories in Figure 5.4, it can be easily seen that increased flight-time will also increase the spread of electrons on the detector, as the electrons radiate from the intermediate focus. These shifts in positions add an additional complication to the gate. In the non-gated, angular resolved mode of the lens, the electrons originating from the sample are focused parallel-to-point[6] to the detector. When the detector is displaced, it is also positioned out of focus of the lens. This problem should however be circumvented by an adaptation of the lens focus to the new detector position (by changing potentials of the lens elements) and an updated transformation matrix (equation (5.3)). The decelerating potential on the M2 mesh effectively "elongates" the lens by increasing the flight-time. This elongation is dependent on the gating potential, as can be seen in Figure 5.11, but also on the kinetic energies of the electrons. Keeping in mind that a range of electron energies should be readily detected, it must also be noted that the flight-time is not linear with regard to the electron energy. Figure 5.12 reflects this phenomenon.

While $\Delta t$ can be calculated analytically, there is no possibility to analytically determine the position deviation for each combination of electron energy and initial angle. Such analysis must therefore be executed with the aid of simulations performed by the manufacturer.

[6] Monoenergetic electrons emitted with identical angles, but from different sample points, are focused to the same point on the detector.

### 5.4.4 Experimental results

Results are presented in Paper **VI** and will only be discussed briefly here. The main figure of merit for detector gating is the detection efficiency; defined as the number of detected electrons originating from the selected camshaft bunch and arriving within the analysis time window (within the specified energy window). These electrons represent the *effective counts*, which are compared to the *total number of counts*. The detection efficiency is increased in two steps; by introducing the constant potential $V_{\mathrm{nej}}$ and by the gate pulse. To quantify this effect, we made three sets of measurements on a bilayer graphene sample, using 185 eV light and the centre energy of the lens at 175 eV, thus measuring parts of the valence band. The first measurement had no constant voltage applied, resulting in 300 effective counts/s out of a total count rate of 90,000 counts/s (efficiency: 0.3%). The application of a constant potential $V_{\mathrm{nej}} = 164\,\mathrm{eV}$ gives 600 effective counts/s out of a 72,000 counts/s total (efficiency: 0.8%). Finally, the application of the gate pulse at 20 V amplitude gives 5,000 compared to 65,000 counts/s (efficiency: 8%), increasing the efficiency by an order of magnitude. The latter efficiency increase is expected at BESSY, since roughly 10% of the total current in the ring is due to the camshaft bunch. Figure 5.13 shows the full time-of-flight spectrum acquired with and without the gate pulse applied. The energy analysis of the electrons in the analysis window (Figure 5.14) reveal that the kinetic energy spectrum is undisturbed by the gate pulse.

The constant potential $V_{\mathrm{nej}}$ introduces a clear cut-off with a characteristic cone–shape which can be clearly seen even without an applied gate pulse. Figure 5.15 shows flight time vs. detector position for four different deflection potentials. Electrons with longer flight times are accepted at the centre of the detector, while electrons at the periphery have a more restricted acceptance. We would expect the opposite behaviour if the cut–off was uniform with regard to the electron energy. An electron hitting the detector close to its edge has a longer flight time than an equally energetic electron hitting the centre. Therefore, this effect must have a different origin. We have not conclusively established why this phenomenon appears. It is known from the properties of the lens that electrons hitting the detector in the periphery will have smaller impinging angles towards the mesh ensemble. Since electrons with initial kinetic energies close to the cut off potential will be decelerated to very low velocities, it is possible that those with smaller impinging angles are more likely to be deflected by the constant potential. This feature has implications on the energy analysis, since we can see that electrons are deflected even if their kinetic energy should be sufficient to clear the deflection potential. The cone edge has a well-defined shape and magnitude, and moves along the TOF $t$-axis proportionally to the magnitude of the potential. This implies that no effect should be present at a suffi-

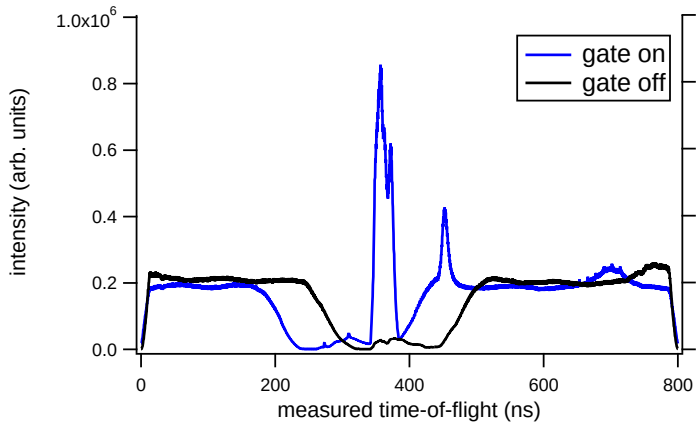


**Figure 5.13.** *Full measured time-of-flight spectrum on graphene valence band with (blue) and without (black) gate enabled. The spectra have been normalised to the (apparent) background level of the bunch train electrons. The gate pulse was delayed to match the desired temporal window for gating the electrons originating from the hybrid bunch. The graph clearly shows how the analysable electrons originating from the camshaft bunch are enhanced.*

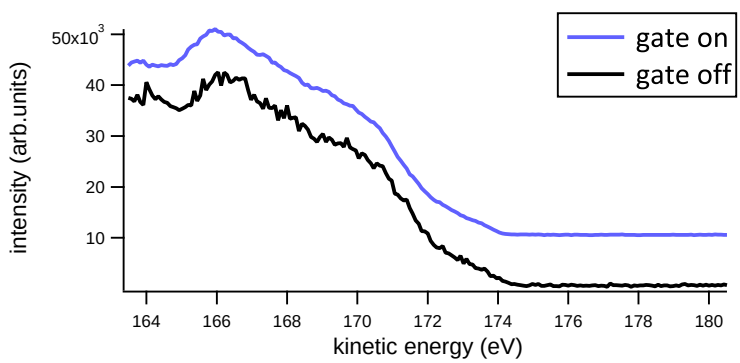


**Figure 5.14.** *The graphene valence band spectrum obtained with and without gating during 10 minutes measurement. The statistics of the former in much higher, although all features of the spectrum are preserved.*

ciently low deflecting potentials.

### 5.4.5 Discussion

We have shown that it is possible to gate an ARTOF spectrometer by using the signal originating from the camshaft pulse(s). The efficiency of the detection has been shown to increase with at least one

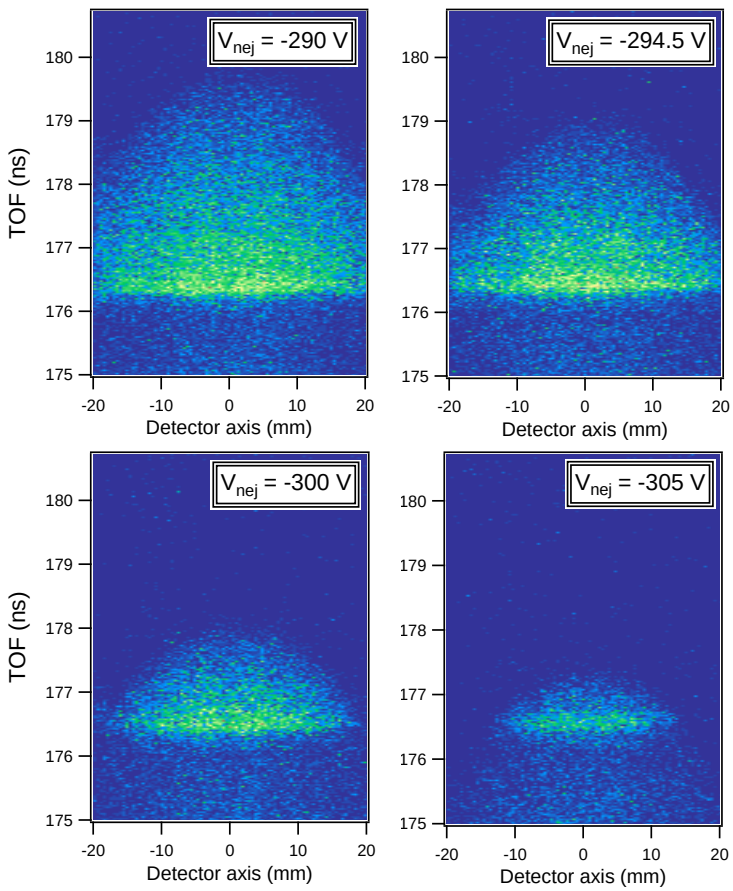


**Figure 5.15.** *Measured graphene valence spectra for four different $V_{\mathrm{nej}}$ deflecting potentials. These spectra were measured with* 320 eV *photon energy and the lens focused at* 310 eV *electron kinetic energy, measured for five minutes each. The analysable window of the spectrometer is 30 eV and extends from 168 ns to 192 ns. The spectra clearly show the cone–shape of the cut-off, and its movement along the time axis as the deflecting potential increases.*

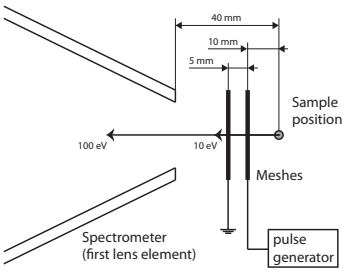


**Figure 5.16.** *The conceptual design of the electronic gate. The mesh closest to the sample is connected to a fast pulse generator. The second mesh shields the entrance to the spectrometer from the gating potential. The annotations refer to the setup intended for the ARTOF 10k, where lens-to-focus distance was 40 mm. The distances travelled by a 10 eV and a 100 eV electron in 10 ns are indicated.*

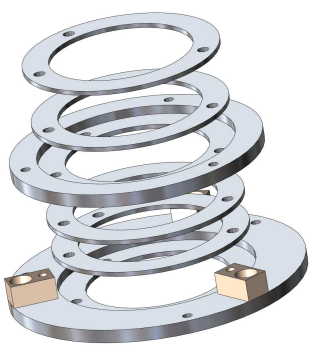

**Figure 5.17.** *Exploded view of the front gate designed for use with ARTOF 10k and ARTOF-2. The meshes were glued between the thinner rings and mounted to the holder. The lower mesh holder was fastened with screws directly on the first lens element.*

order of magnitude. Detector gating is restricted to hybrid modes. This gating scheme should be useful for operation at BESSY together with a mechanical chopper [97] or resonant pulse picking [79]. A plan to utilize this combination is currently pursued at BESSY where both choppers and pulse picking will be commissioned soon.

## 5.5 Front gating

The front gating scheme was developed particularly with operation at MAX IV in mind; namely to multi–bunch operation with 10 ns pulse separation. The theoretical and methodological framework is outlined in Paper **VII**, which was presented at the *Synchrotron Radiation Instrumentation* conference in July 2012. During 2013 and 2014, the front gating scheme was adapted to allow for proof-of-principle tests to be made at BESSY in hybrid mode. Although front gating and detector gating have been developed in parallel, detector gating was prioritised due to its direct applicability to BESSY operation. Initial tests with a mounted front gate were performed at BESSY in March 2014. This chapter presents the current state of front gate development. It shows how the front gate has been realised together with results from initial tests. Although the front gate measurements have not showed conclusive results yet, they can provide a base for further development.

### 5.5.1 Physical design

The original design considerations for the front gate were presented in Paper **VII**. In its most simple form, it consists of two consecutive high transmission meshes placed in front of the first lens element of the ARTOF (see Figure 5.16). A sufficient negative potential is applied to the mesh closest to the sample. The purpose of this gating potential is to deflect all electrons away from the lens when the gate is closed. The second mesh, which is grounded, has two functions: Firstly, it protects the spectrometer from the gating potential, whereas the gating potential otherwise would leak into the lens and obstruct its focusing condition. Secondly, it increases the available ramp–up time for the gating potential. When the gate is closed, no electrons from the interaction region are able to reach the spectrometer. To open the gate, the potential is reduced to zero (ground) allowing for undisturbed passage of electrons.

Since the publication of Paper **VII**, the conceptual design was developed into the front gate seen in Figure 5.17. The gold meshes were fixed between two stainless steel rings with UHV-compatible silver–glue. The meshes were straightened to assure high flatness. Two stainless steel holders were created for the mesh rings. These were separated with isolating spacers made from UHV–compatible PEEK. The inner holder could be mounted directly on the spectrom-

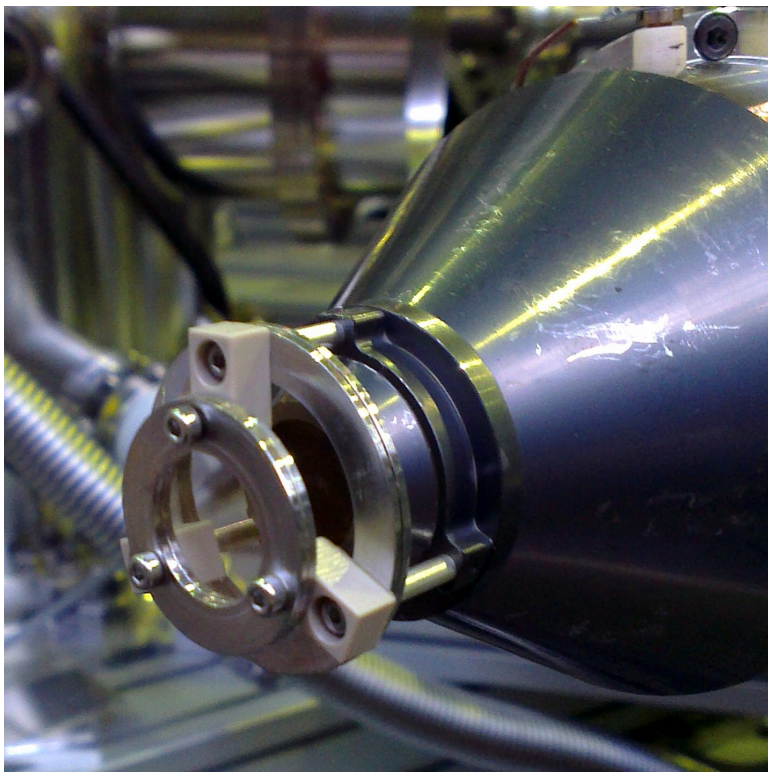

**Figure 5.18.** *Front gate mounted on the pre-lens. The gate was elevated from the lens using aluminium spacers since the lens geometry did not allow a direct contact mount.*

eter nose by removing the nose cap and using existing screws. The design was made to fit both ARTOF 10k and ARTOF2.

The high transmission gold mesh was acquired from *Precision Eforming* (28 wires/cm, 18 $\mu$m wire diameter, and 90 % transmission efficiency). Effective diameter for both meshes was 32 mm. They were mounted with 8 mm separation, which was sufficient to prevent sparks from the high–voltage loads.

A second design was developed for use with the ARTOF 10k pre-lens[7]. Due to the smaller nose and a shorter lens-to-focus distance, it was used without holders. The outer mesh diameter had to be reduced to allow for the light beam to pass the gate without being blocked. Effective diameters were 15 mm and 35 mm. A photograph of the mounted front gate for the pre-lens is seen in Figure 5.18.

[7] This lens was constructed at Uppsala University for use together with the prototype version of the ARTOF 10k. Sone Södergren, Uppsala University, is acknowledged for providing details of the design.

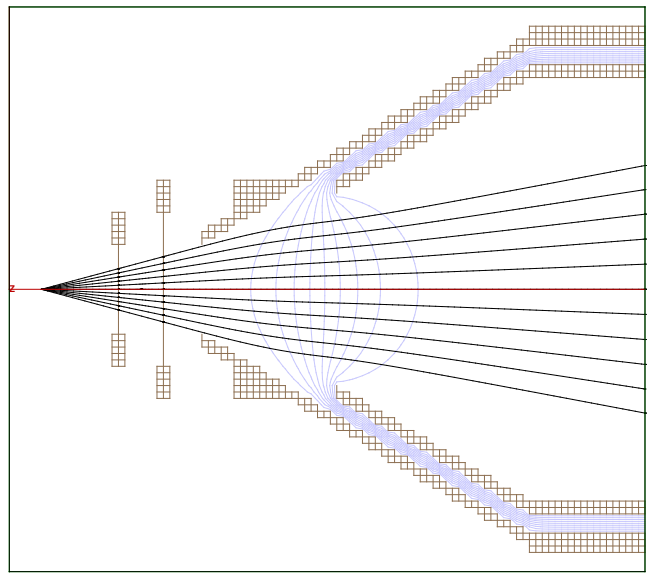

**Figure 5.19.** *Electrostatic simulation of the front gate mounted on the pre-lens. The isolating mounting of the gate is not included as they only have minor effect on potentials. The simulation is cylindrically symmetric. A positive potential equal to the electron kinetic energies is applied to L1. Potential surfaces are shown in blue. An electron fan with ±15° is emitted from the source position 25 mm from the lens front.*

The inclusion of additional electrostatic elements to the lens system will inevitably disturb the trajectories of electrons. Even slight changes in arrival times, arrival positions or focus conditions have substantial effects on resolution. Therefore, precautions must be made to ensure that these disturbances are kept to a minimum and become predictable. Changes of original trajectories can be tolerated if a renewed calculation of lens potentials can account for them. In this respect, front gating constitutes a stronger disturbance to the instrument than detector gating; the reason being that the disturbing element is placed very early in the lens, thus allowing a directional error to propagate over the full flight trajectory.

When no gate is mounted to the spectrometer, the electric field at the nose is determined by shape and applied potential to the first lens element (L1). The front of an electrostatic lens for electron spectroscopy is typically grounded [100]. L1 is located some mm inside the spectrometer opening. Usually an accelerating potential is applied to L1; this potential increases collection efficiency since a larger emission cone can be accepted by the instrument. Figure 5.19 shows an electrostatic simulation of the front gate mounted on the pre-lens (as depicted in Figure 5.18). For this simulation the SIMION soft-

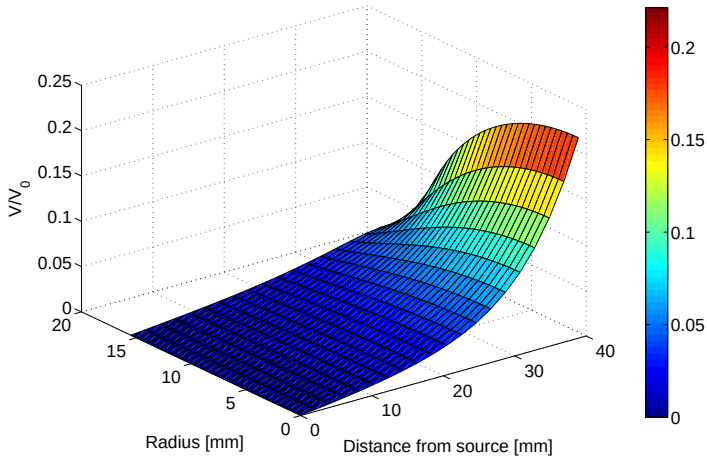


**Figure 5.20.** *Field penetration from ARTOF 10k lens. Source point is at (0,0) and centre of lens opening is 40 mm from source. Potential is given as the fraction of the L1 potential. The lens is cylindrically symmetric. (Data courtesy of VG Scienta AB.)*

ware [51] was utilized. L1 is situated >20 mm from the opening of the lens. The simulation shows that the field penetration through the lens opening is <2%, and we expect that the front gate has only a minor effect on the electron trajectories while all gate components are grounded. As a rule of thumb, the penetration length through a cylindrical aperture equals its diameter [125, p. 201]. Figure 5.20 shows the field penetration from the ARTOF 10k lens [106], as it was simulated by *VG Scienta AB*. In this case there is a non-negligible potential contribution to the source point. In this geometry, inclusion of a gate mesh is possibly a destructive intervention in the lens.

A recent updated design of the ARTOF includes a wide–angle lens. These new lenses will allow for a further increase in transmission and ability to record larger electron emission fans in the angle–resolved mode. These wide–angle lenses are terminated at the nose with a mesh. A future extension of the front gating concept to this lens would mean simply adding an additional mesh with similar dimensions in front of the permanent mesh. In addition, studies with wide angle lenses have shown that spherical and ellipsoidal meshes can be used to further increase acceptance angles [126, 127]. The front gating concept could possibly be extended to these mesh shapes.

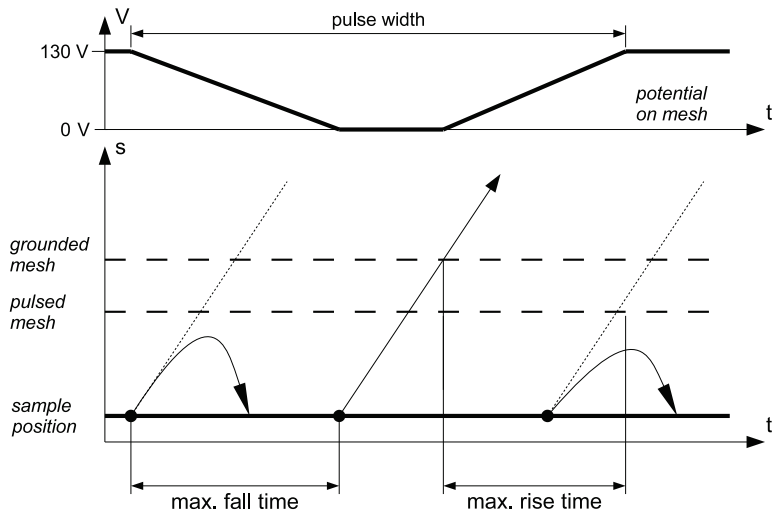


**Figure 5.21.** *Timing principle for the gate in a 2D time–space–diagram together with required gating potential. The tilted lines indicate propagation of mono-energetic electrons through the gate. The first and third electron should be deflected, while the second should pass the gate. Mesh potential is given for 100 eV electrons. The limits for rise time decreases as electrons become slower, while fall times can be constant.*

### 5.5.2 Electronic pulsing

The electronic pulsing requires a pulse generator and a suitable connection to the mesh in vacuum. It was aimed to operate with ∼1 MHz repetition rate, addressing typical flight times in the ARTOF (∼1$\mu$s ), required fall and rise times and the overall pulse width (Figure 5.21). High demands are put on the electronics, but solid-state switches with rise/fall–times down to a few ns sustaining 1 kV and 1 MHz repetition rate are commercially available (see e.g. Refs. [128, 129]). For gating at MAX IV multi–bunch conditions or BESSY hybrid mode the *BEHLKE FSWP 51–02* MOSFET–type solid–state switch [128] was considered. It provides <50 ns pulses (rise–time 6 ns, fall–time 11 ns) with repetition rates up to 3 MHz and 5.4 kV amplitude. For BESSY hybrid mode conditions this is sufficient without adaptations. For MAX IV multi bunch, we require <20 ns pulses, and in Paper **VII** we propose a solution with two switches providing alternating blocking pulses. This would allow for a shorter opening window if the pulse generators have a very precisely determined delay. Each switch must be synchronized to the frequency of the light pulses, which can be extracted with a photo–diode in the experimental chamber, or obtained from the ring clock. The BEHLKE switch requires liquid cooling, which we could not provide for our initial tests of the front gate. Therefore, the tests were performed at BESSY using a DEI PVM-4210

pulse generator module [129], fed by a +24VDC power source and a NIM pulse with variable pulse length and repetition rate produced by a function generator. With this setup ∼100 ns pulses with 100 kHz repetition rate and amplitude just above 100 V could be produced.

To maintain good focus of the lens, it is necessary to avoid disturbances from the gating mesh while the gate is open. Ideally, one would have zero gating potential during the electron pass. The signal from the system must therefore be sufficiently free from ringing[8]. Our calculations show that the capacitance of the gate can be kept below 10 pF when short wiring is used. The internal capacitance of the pulse generator is expected to be larger. Considering a maximum 500 V gating potential achieved in 3 ns, the required peak current is ∼2 A, which allows for a SHV transmission line to be used. In our tests, the gated mesh holder was connected by an impedance matched coaxial cable, while the shielding was connected to the ARTOF nose. A SHV UHV feed–trough provided connection to vacuum.

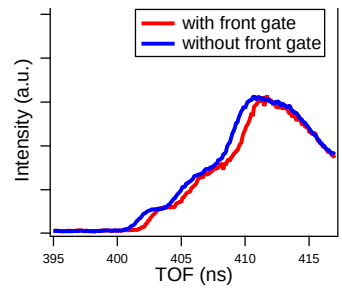


**Figure 5.22.** *Time-of-flight spectrum of the graphene valence bands originating from the hybrid peak. The photon energy was 120 eV. The two bands display a relative shift of 0.8 ns, which can be attributed to an error in the placement of the sample.*

### 5.5.3 Experimental results

The first experimental tests were performed at beamline UE52-SGM at BESSY, with the storage ring running in hybrid mode. The gate was mounted at the pre-lens, as shown in Figure 5.18. A bilayer graphene sample on SiC was mounted on a manipulator arm along the ARTOF axis.

To establish if our mounting of the front gate changes the electron spectrum, we compared two sets of measurements on the valence band with and without the gate meshes mounted. The photon energy was set to 120 eV and all beamline settings were unchanged between the measurements. As the front–gate was installed, the nose-to-sample distance was increased by ∼4 mm to allow enough room for the synchrotron beam to pass[9]. Since the ARTOF was removed and later reinstalled at the chamber, it was not possible to establish the exact change in nose-to-sample distance[10]. Figure 5.22 show measured TOF in the region of interest. The displayed spectra are almost identical apart from a 0.8 ns shift towards longer flight times for the installed front gate (red curve). From electrostatic simulations we find that this is consistent with a sample placement 5 mm further from the nose. When correcting for this temporal shift, we acquired the photoelectron spectra in Figure 5.23. The measured spectra are clearly consistent above 112 eV. Below 112 eV, there is a constant reduction of measured intensity when the front gate was installed. The

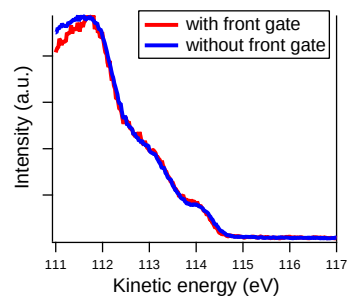


**Figure 5.23.** *The graphene valence bands measured at 120 eV photon energy before and after the installation of the front gate. The temporal shift noted in the previous figure has been corrected prior to energy analysis.*

[8] Ringing occurs in electrical circuits as an unwanted oscillation of a voltage or current, caused by stray capacitances and inductances in the circuit.

[9] As mentioned, the front gate had been mounted 10 mm further from the nose than the design value.

[10] An indirect correction for this change could have been done by a renewed $t_0$ calibration using scattered photons.

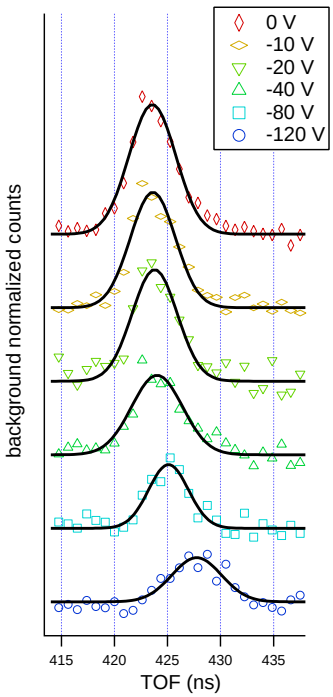


**Figure 5.24.** *Time-of-flight spectrum of the unresolved Si 2p peaks (expected $E_{kin} \approx 105$ eV) with applied constant potentials to the first mesh. The Si 2p peak originates from bulk SiC. The intensities have been normalized to the background level, as described in the text. Background has been subtracted in this spectrum.*

shape of this edge is a consequence of the applied cut–off potential on the detector mesh, which was set to −109.25 V. We know from detector gating that the potential $V_{\mathrm{nej}}$ affects electrons also within the lower end of the energy window due to their transverse momentum components while flying through the instrument. The intensity difference at the edge of the energy window should therefore be disregarded. The disturbing effects of installing the front gate are thus very limited, if any, and a valence spectrum can be completely reproduced.

To establish the effect of the front gate potential, we performed two series of measurements where a constant negative potential was applied to the gating mesh without any gating pulse. The Si 2p doublet–peak was measured with 210 eV photon energy. The doublet structure is expected at 105 eV kinetic energy. A set of measurements with different constant potentials are displayed in Figure 5.24. A similar set of measurements of the graphene valence band is displayed in Figure 5.25. This spectrum was acquired at 90 eV photon energy. All spectra were normalized using a similar method: The background constituted up to 50 % of the total count in the region of interest[11]. We observed during detector gating studies that the background mainly consists of high energy electrons which are emitted due to second order light. These high energy electrons are not hindered by the front gating potential and the background count rate is expected to be constant for all measurements. Therefore, the peaks were normalised to the background level at the position of the peak centre of the undisturbed peak (front gate mesh at ground). For Si 2p we fitted the peaks to a Gaussian line shape.

Both the Si peaks and the graphene band display a gradual reduction of intensity as the potential is increased. We also observe a peak shift towards longer flight times. Although this trend is expected due to the retardation electrons experience at the front gate, it is striking that no clear cut–off is observed. As the potential is raised above the kinetic energy of the electrons, we still observe peaks in the region of interest both for Si 2p and graphene valence. This behaviour could be explained in two ways: Either a large fraction of the electrons manage to pass the gate following trajectories which bypasses the gate, or that a correct potential was not applied or supplied to the mesh. The behaviour of both sets of spectra points towards the latter solution. In particular, the sudden reduction of intensity and shift of peaks for the Si–spectra with –80 V and –120 V applied potential (Figure 5.24) hints that the potential actually applied was close to the electron kinetic energy, but did not exceed it. Such a potential, my simulations show, would cause a fraction of the electrons to follow trajectories which would not be accepted by the instrument, in fact the graphene spectrum (Figure 5.25) displays a shift for –100 V and –

[11] Due to a problem with the BESSY injector during the measurements the relative intensity of the hybrid peak was smaller than under normal hybrid operation.

120 V, while the –140 V spectrum has been shifted towards shorter flight–times. The latter effect may be explained if the applied potential manages to block slow electrons in the measured band, while faster electrons pass through. The experienced potential reduction has to be explained by a faulty potential source or a potential drain in the chamber. Inspection during dismounting of the instrument has given no indication of any direct problem in mounting.

As a final test, we considered the possible disturbances on the detector read–out due to transmission of RF-frequencies. The outcome of our successful detector gating showed that the detector was overloaded when a gate pulse was applied close to the MCP. Tests showed that when the gating pulse contained higher frequency components, the detector tended to be overloaded[12]. The MCP read–out is particularly sensitive, but also the delay–line readings can be affected. A challenge is when noise similar to real signals stall the detector. For the front–gate, there were particular concerns that the hollow ARTOF lens would act as a wave–guide and effectively transport unattenuated RF-signals to the detector. To test this effect, we performed measurements where a sinusoidal signal with 10 V amplitude was fed to the gate mesh. The frequency was increased in steps from 100 MHz to 70 MHz while the responses on the MCP and the delay–lines were monitored. The reference count-rate at zero frequency was 400 kcounts/s in the MCP channel and 60 kcounts/s (complete events) in the DLD-channel. At 60 MHz the MCP count had increased to 600 kcounts/s and DLD-count to 100 kcounts/s. At 68 MHz a sudden detector overload occurred independently in both the MCP and DLD-channel.

We proceeded by applying regular 100 ns long pulses from the DEI pulser to the gating mesh, gradually increasing their amplitude. We could increase the amplitude from zero to 300 V without overloading the detector; higher amplitudes were not permitted by the pulse generator.

The pulse generator used was a severe limitation. Creation of the required pulse frequency could not be achieved when its duration was reduced to 100 ns. Therefore we could not create a pulse with required characteristics for gating. While a 100 ns pulse could be created, it could only be delivered with 50 kHz repetition rate, thus only picking 1 in 25 hybrid pulses. We established through an oscilloscope observation that ring clock synchronization was achieved. We could also create a precisely determined delay to center our pulse to the hybrid window. However, we could not distinguish any "true" spectrum or peak from the comparatively large high–energy electron background presumably created by second and third order light, as

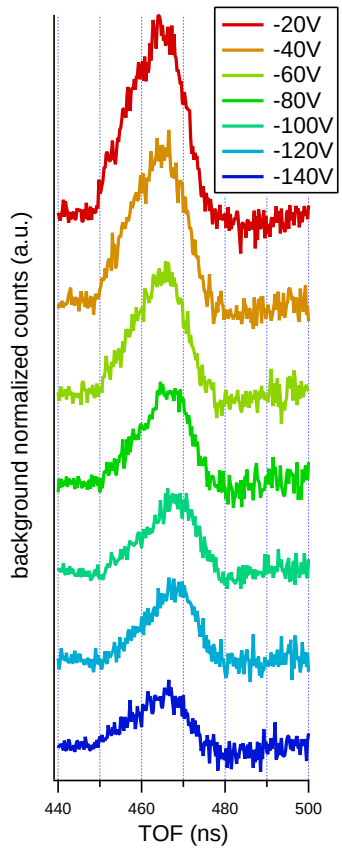


**Figure 5.25.** *Time-of-flight spectrum of the graphene valence band with applied constant potentials to the first mesh. The photon energy was 90 eV. The intensities have been normalized to the background level, as described in the text.*

[12] It should be noted that overload due to stray frequency components is different from overload due to intense electron impact. The latter causes large currents to pass through the MCP which may cause the detector to burn. Frequency overloads cause only signal errors and are not harmful to the detector.

well as scattered photons. Actual gating of the hybrid peak thus remain to be achieved.

### 5.5.4 Discussion

Electrostatic simulations and experimental verification has shown that a front gate can be installed without severe disturbances to electron trajectories at the ARTOF pre–lens. The effects still need to be studied for other lens designs. We also saw that electric pulses of the required length and amplitude could be applied to the gate without overloading the detector.

CHAPTER 6

# ELECTRON/ELECTRON COINCIDENCE SPECTROSCOPY WITH ULTRA-HIGH RESOLUTION AT MAX IV

This chapter outlines an experimental setup which is suggested for MAX IV. The electron/electron coincidence experiment is treated in brief in Paper **V**. Experiments to show proof–of–principle were performed at MAX II, beamline I411, in May 2015. It was possible to show that the hemispherical analyser indeed had the necessary temporal dispersion properties, and that electrons could be recorded with sufficient time–resolution. However, it was found that the transmission of the proof–of–principle setup was not sufficient to record actual coincidences. Nevertheless, first results together with other considerations outlined in this chapter show that the prospect of a ultra–high resolution electron/electron coincidence station at MAX IV is promising. I propose that further studies are carried out at the *FinEstBeaMS* or *FlexPES* beamlines when the MAX IV 1.5 GeV ring becomes operational.

## 6.1 Background

Electron/electron coincidence (ee–coincidence) spectroscopy has been used for many years to disentangle effects in photoemission experiments where more than one electron is emitted. If a sufficient amount of energy is transferred into a system, double ionizations can occur directly or by some subsequent relaxation process. A coincidence spectrum shows the correlation between the two electrons and substantially increases the amount of information drawn from the experiment. Applications for ee-coincidence experiments were

recently reviewed by Arion and Hergenhahn [37], and only those relevant for studies included in this thesis are discussed here.

The prototypical ee–coincidence experiment is Auger/photoelectron coincidence spectroscopy (APECS) [130, 131]. Such experiments have been performed both on solid and gas phase samples with the promise to achieve sub-natural linewidths and to reveal very weak features in the Auger spectrum [132]. A non-coincident Auger spectrum typically displays broad lines where contributions from different electronic states can overlap. Large line-widths in Auger spectra arise from the short lifetime of the excited state, causing a line broadening due to the uncertainty principle. Measuring the sum of the photoelectron and the Auger electron eliminates the dependency on the intermediate excited state. One case is how so called Coster–Kronig lines – radiation-less electronic transitions within an excited atom/molecule – can be resolved by means of ee-coincidence [133]. However, such experiments are only meaningful with spectrometers that have sufficient instrumental resolution to resolve sub-natural linewidths.

A particular issue in ee–coincidence experiments is to achieve reasonable resolution and high transmission simultaneously. Transmission is of particular importance in coincidence experiments since it is necessary to reduce the number of accidental coincidences and improve the signal–to–noise ratio. There are several studies employing high–resolution/low–transmission instruments where the coincidence rates were only a few counts per minute. As noted in Chapter 5, TOF instruments have higher transmission than hemispherical analysers [107]. In recent publications, Lupulescu *et al.* [134] and Arion *et al.* [38] showed how the ARTOF can be used to achieve high transmission in one of the spectrometers, while high energy resolution is retained. The detection of an electron in the hemispherical analyser is used as a start trigger for the ARTOF instrument. The measurement uncertainty is determined by the time-of-flight spread of detected electrons in the hemispherical analyser, which is ∼6 ns for 200 eV pass energy [134]. This *time-reference broadening* accounts for half of the total timing error and becomes even more dominating if the pass energy is reduced. The 500 MHz RF system at BESSY [67] provides no possibility to eliminate this error by assigning electrons to specific light pulses (separated by 2 ns). However, at MAX IV the 100 MHz RF system – corresponding to 10 ns pulse spacing – makes it possible to find the arrival time of the light pulse, and directly use it as a reference for the ARTOF. The instrument resolution then equals the stand–alone resolution at a pulsed (single–bunch) source. It would also be possible to reduce the pass energy of the hemispherical analyser, which enhances energy resolution in this channel. It has been shown that the pass energy can be set below 20 eV before time dispersion exceeds 10 ns [135].

## 6.2 Instrument and signal handling

Several setups for hemispherical–analyser/TOF ee–coincidence experiments have been commissioned in the last decade. Ulrich *et al.* [104, 136, 137] used a *Scienta ES 200* hemispherical analyser [115] and several eTOF spectrometers to achieve high energy resolution at BESSY. At the same facility, an experimental station named *iDEEAA* has been commissioned [38, 134], employing a *Scienta R4000* hemispherical analyser and an ARTOF [106].

The hemispherical analyser exploits the dispersion of electrons in an electric field for energy analysis (Figure 5.1). The electric field between two concentric hemispheres with radii $r_1$ and $r_2$, and charged by potentials $V_1$ and $V_2$ is [100]

$$E_r(r) = -\frac{V_2 - V_1}{r_2 - r_1} \cdot \frac{r_1 r_2}{r^2}. \tag{6.1}$$

This inverse–square–dependent field makes electrons travel on Kepler–like elliptical trajectories from the entrance slit to the detector. The potentials are set to allow for electrons with kinetic energies equal to the so called pass energy $U_0$, which enter the hemisphere parallel to its surface at a radius $r_0$, to travel on a circular orbit and be focused to a point on the detector (also at radius $r_0$). Wannberg [100] calculated that electrons with a different energy, $U_0 + \Delta U$, will move on trajectories that intersect at a point given by

$$r = r_0\left(1 + 2\frac{\Delta U}{U_0} + 4r_0\left(\frac{\Delta U}{U_0}\right)^2 + \cdots\right). \tag{6.2}$$

To first order, the energy disperses linearly with $\mathrm{d}r/\mathrm{d}U = 2r_0/U_0$.

Figure 6.1 (taken from Ref. [104]) shows the temporal performance in a measurement of the Auger spectrum from $O_2$ with a *Scienta R4000* hemispherical analyser at BESSY. Panel (a) displays Auger electron energies vs. time of detection (referenced to the ring clock). BESSY was run in hybrid mode [99]; electrons emitted from the camshaft bunch stand out as (almost) vertical lines separated from those created by the multi–bunch train. Electrons created by a sufficiently separated light pulse can be distinguished in a time-of-flight spectrum; 2 ns, the multi–bunch separation at BESSY, is not sufficient. The map in Panel (c), which zooms in on the hybrid bunch electrons in Panel (a), illustrates the two major broadening effects in the time–of–flight spectrum: the *dispersion*, which causes the slope, and the *spread*, which manifests itself in the vertical size of the feature. The dispersion is energy dependent, arising because high energy electrons have longer flight paths. It can be corrected for in the analysis. Panel (b) shows the size of the time–of–flight spread, which is not resolvable and becomes a measure of how much separation is sufficient to resolve adjacent light pulses in the hemispherical analyser. The full-width half-maximum is 6.2 ns, although the full peak is

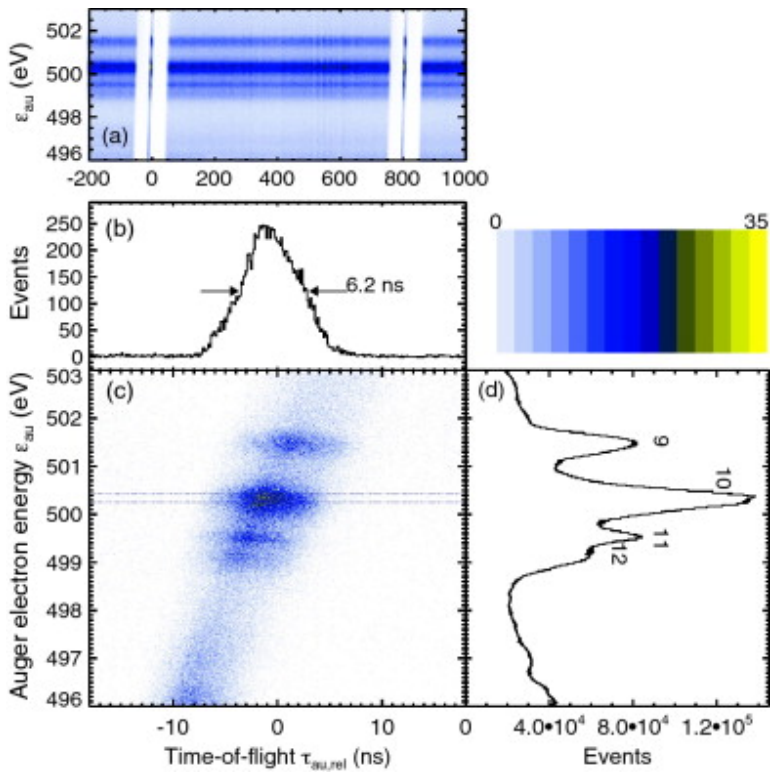


**Figure 6.1.** *Auger spectrum from $O_2$ (y-axis) vs. time-of-flight in the hemispherical analyser (x-axis). The structure in Panel (a) reflects the (then) hybrid mode structure at BESSY [99]. Panel (c) shows a zoom of the electrons emitted from the hybrid bunch, with the integrated Auger spectrum in Panel (d). Panel (b) has the time-spread between the two dotted lines in Panel (c). (Reprinted from Ref. [104] with permission from Elsevier.)*

close to 10 ns in size. A storage ring filling pattern with 10 ns bunch separation would thus render resolved structures in Panels (a) and (c), *all* electrons could be assigned to specific light pulses. In a coincidence experiment it makes a differencewhether a hemispherical analyser detection can be assigned to a light pulse or not. Consider two electrons created in the same ionization process. Since the light pulse is the cause of the ionization process, its time of arrival is the true start of the time–of–flight measurement. If electrons are referenced to a specific light pulse, the precision of the TOF measurement is determined instead by the length of the light pulse, its degree of monochromatisation and the instrumental broadening. When an electron cannot be referenced to a light pulse, it is referenced to the time of detection in the hemispherical analyser. The time–reference broadening was quantised for the iDEEAA station for 10 eV photo-

electrons (measured in ARTOF analyzer) and Auger electrons (measured in R4000 analyser, 5.3±0.3 ns FWHM time-spread) [134]. They found that the time-reference broadening corresponded to 116 meV, to be compared to the ARTOF resolution (36 meV) and the beamline resolution (72 meV). An elimination of this effect, as would be possible at MAX IV, would thus reduce the total energy error from 142 meV to 90 meV with otherwise identical conditions[1].

The time-spread in hemispherical analysers has been discussed in detail by Kugeler, Marburger and Hergenhahn [135]. They present both an analytical expression for the time-of-flight and experimental results for a *Scienta SES 200 ES* spectrometer. It is found that electrons with kinetic energies between 95% and 105% of the pass energy have spreads between 3.0% and 3.8% of the ideal time-of-flight. The ideal time-of-flight for the pass energy can in turn be determined by the radius of the ideal (circular) path ($r_0$ =200 mm) and the electron speed ($v = \sqrt{2U_0/m}$); and

$$\delta t \propto r_0/\sqrt{U_0}.$$

## 6.3 The ee-coincidence test experiment at MAX II

A coincidence setup was constructed at MAX–lab using spectrometers and vacuum equipment provided by the Nano and molecular systems group (Nanomo) at the Centre for Molecular Materials Research, University of Oulu, Finland.[2] The setup consisted of a SES–100 hemispherical analyser and an electron TOF spectrometer (eTOF) mounted on a vacuum chamber with a common source point. The eTOF follows the design by Hemmers *et al.* [103] and was originally developed for analysis of low–energy electrons [138]. Its angular acceptance is low, only 3.4°. The experiments were performed at the one metre section at the I411 beamline at MAX II [139]. A xenon gas sample was let in to the chamber via a custom–made gas needle. Characterization of the hemispherical analyser was made using $N_{4,5}OO$ Auger electrons [140] created by 100 eV photons.

Time–of–flight correlation in the ee–coincidence test setup requires the extraction of four signals:

(i) The time of detection in the hemispherical analyser, extracted from the MCP signal.

(ii) The hit position along the energy dispersion direction on the detector. This could be read as amplitude from the resistive anode detector.

[1] Lupulescu *et al.* found 81 meV total broadening for the single-bunch operation at BESSY. Bunch lengths at MAX IV is expected to be approximately 10 times longer than at BESSY. If a 5.3 ns time-spread corresponds to 116 meV, a 500 ps pulse length should be roughly 1/10 of that value.

[2] Marko Huttula, Lauri Hautala, Esko Kokkonen, Ari Mäkinen and Paavo Turunen, all at University of Oulu, have contributed to commissioning of the ee-coincidence test setup and are gratefully acknowledged.

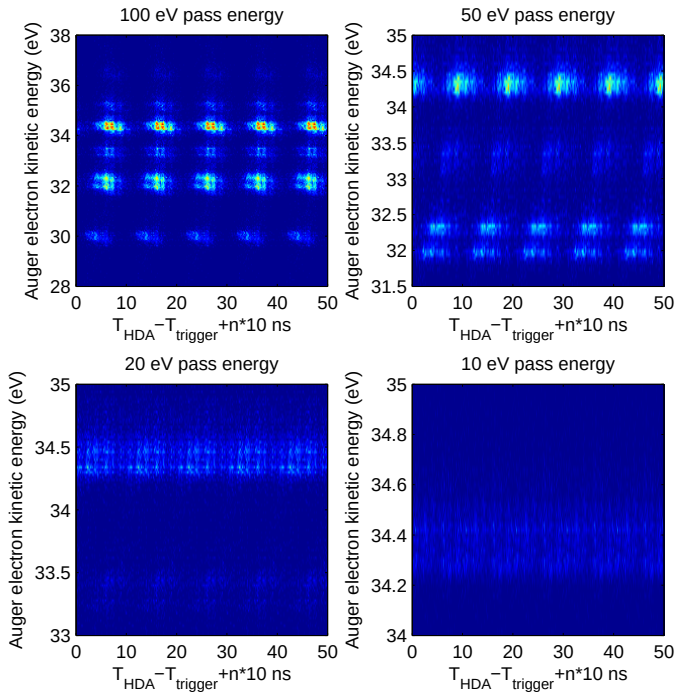


**Figure 6.2.** *Xenon $N_{4,5}OO$ Auger spectrum vs. time–of–flight in the hemispherical analyser referenced to the MAX II bunch marker. Events are artificially repeated every 10 ns to emphasise the separation. Electrons registered within the same vertical group can be assigned to the same light pulse. The kinetic energy scale is approximate.*

(iii) The time of detection in the TOF spectrometer, extracted from the MCP signal.

(iv) The bunch marker, extracted from the storage ring bunch position monitor.

Signals were read and directly analysed by an oscilloscope (*LeCroy WaveRunner 625Zi* 2.5 GHz). It was set to trigger on the hemispherical analyser time signal and measure the time until a subsequent bunch marker and eTOF detection was registered. Also the amplitude of the hit position signal was measured by the oscilloscope. The hemispherical analyser detection signal was preamplified before recording, while the eTOF signal was registered without preamplification. Measured Auger electron energies vs. time–of–flight for four different pass energies are displayed in Figure 6.2. Since the bunch marker from MAX II provides a signal every 10 ns, the hemispherical analyser time-of-flight spectrum is only 10 ns long. In

order for our map to resemble Figure 6.1, where the bunch marker was extracted every second turn (∼2.5 MHz), each event in Figure 6.2 has been plotted every 10 ns in order to see grouping of events clearly. The data shows that events are separable down to 20 eV pass energy for the SES–100 hemispherical analyser, while they are only partly separable at 10 eV. This analyser has $r_0 = 100$ mm, and it is expected that a larger spectrometer has a wider time–of–flight spread.

Figure 6.2 also shows that MAX II 100 MHz conditions differ from BESSY hybrid mode in one more regard. While light pulses are distinguishable in energy vs. time maps such as in Figure 6.1, all features will overlap in pure time–of–flight spectra (i.e., if all events in Figure 6.2 are integrated over the t-axis. This effect is due to the dispersion function. Time-structure will thus only be visible directly in time vs. energy maps. This calls for an analysis scheme where the light pulse allocation is based on both time–of–flight and hit position.

The true time–of–flight in the eTOF ($t_{\mathrm{eTOF}}$) can be found as follows. Define the true time–of–flight in the hemispherical analyser $t_{\mathrm{HA}}$. Define also the true flight time $t_{\mathrm{pass}}$ of a reference electron with the pass energy $U_0$. This ideal flight time is constant for fixed potential settings of the hemispherical analyser. The experiment gives three values: The time–of–flight difference $\Delta t \equiv t_{\mathrm{eTOF}} - t_{\mathrm{HA}}$, the apparent (measured) hemispherical analyser flight time $t_m \equiv t_{\mathrm{HA}} - t_{\mathrm{trigger}}$, and the electron energy $U_m$. Data should be plotted like in Figure 6.2. One group of electrons (the reference group, visible as a almost vertical line) should be identified. The dispersion function $t_{\mathrm{disp}}(U)$ is established by connecting intensity maxima within the group. Each event $(U_m, t_m)$ for which $-5\text{ ns} < t_m - t_{\mathrm{disp}}(U_m) < +5\text{ ns}$ is considered to belong to the reference group. For all other events, find $n \in Z$ such that

$$n \cdot 10\text{ ns} - 5\text{ ns} < t_m - t_{\mathrm{disp}}(U_m) < n \cdot 10\text{ ns} + 5\text{ ns}. \tag{6.3}$$

The apparent flight time $t_m$ can now be corrected by subtracting $n \cdot 10$ ns. The true time–of–flight in the eTOF is calculated as

$$t_{\mathrm{eTOF}} = \Delta t + t_m - n \cdot 10\text{ ns} + C \tag{6.4}$$

where $C$ is a constant determined by instrumental factors such as $t_{\mathrm{pass}}$, the phase difference between the trigger signal and the actual pulse, and delays in the signal processing. This factor $C$ has to be determined experimentally.

Before experiments are attempted at MAX IV, it is necessary to devote some attention and preparation to the treatment of true vs. accidental coincidences. Accidental coincidences, i.e. when two apparently coincident electron detections originate from different ionization processes, are unavoidable and cannot be separated from true coincidences on an event-by-event basis. Accidentally coincident electrons can originate from the same or different light pulses. The

treatment of accidental coincidence subtraction from spectra has been covered in detail by Calicchia *et al.* [141]. They distinguish between three cases at storage rings. The previously discussed BESSY multi–bunch experiments fall under Case III, where the instrument timing resolution ($\tau_e$, here approximately equal to the time spread) is larger than the separation between light pulses ($\tau_{\mathrm{bb}}$). The accidental coincidences in this Case are manifested as a wide triangular shape in the $\Delta t$–spectrum with the true coincidence peaks on top (see e.g. Ref. [104]). At MAX IV, where $\tau_e < \tau_{\mathrm{bb}}$ (Case II) is expected, the accidental spectrum will have a fine–structure which is repeated with the bunch frequency [130, 141]. This can be understood by considering a *true* electron coincidence event with measured $\Delta t \equiv t_{\mathrm{true}}$ where the constituent electrons have measured energies $U_1$ and $U_2$. In general, electrons with these energies will be created by all pulses with equal probability. When two such electrons originate from two different light pulses, but are detected in coincidence, the measured time will be $\Delta t = t_{\mathrm{true}} + p \cdot 10$ ns, where $p \in Z; p \neq 0$. In essence, accidental subtraction in this Case II is made by taking the original $\Delta t$–spectrum, shift it by $p \cdot 10$ ns, where $p \in Z; p \neq 0$, and subtract from the original spectrum. If all bunches in the ring are equal, the choice of $p$ is arbitrary. If they are not equal, it is necessary to use $p$ equal to the harmonic number of the storage ring, i.e. the number of buckets in the ring.

## 6.4 Conclusion

Initial experiments at MAX II show that the 100 MHz time structure at MAX IV can be utilized to construct an ee–coincidence experimental station with higher resolution than similar stations at 500 MHz storage rings. The 10 ns separation between light pulses allows for electrons in a small hemispherical analyser to be assigned to a specific light pulse above 20 eV pass energy, and thereby eliminating the time–reference broadening. The 100 MHz system; unique for MAX IV, the Solaris-ring in Poland and the Astrid-ring in Aarhus; allows a substantial improvement of resolution in both channels, while preserving high transmission. Put into practice, this electron coincidence scheme would provide users at MAX IV with the highest resolution achievable at any storage ring in the world.

CHAPTER 7

# CONCLUSIONS

In this dissertation I have explored time–of–flight based spectroscopies at storage ring light sources. Spectroscopy has many interesting applications and holds promises to further advance the understanding of matter in its many forms. The dissertation highlights, in particular, achievements in terms of storage ring light source developments, beamline instrumentation and spectroscopic techniques. The seven papers seek in different aspects to contribute to the advancement of spectroscopy and spectroscopic techniques.

I discuss in this chapter some possible future directions for the instrumentation projects I have engaged in during my PhD studies. The conclusions also treat particular opportunities for MAX IV to host state-of-the-art timing–based instrumentation, which I hope can be further advanced in the coming years.

## 7.1 Future developments of coincidence experiments with *ChristianTOF*

The instrument for mass–resolved NIPICO (Paper **I**) is now commissioned and in operation at the Gasphase beamline at Elettra. Since the first beamtime, which produced the data in Papers **I** and **II**, the instrument has been used in two additional beamtimes where NIPICO and NIPIPICO yields of several molecules have been measured. Since NIPI(PI)CO at core-edges is mostly uncharted territory, the instrument should deliver new and valuable data for a large set of samples for some time to come. Updates to the detector in December 2015 increased the efficiency and signal–to–noise ratio of the instrument substantially, which allowed us to measure larger samples, i.e. polyatomic molecules with several different atom constituents. The increased efficiency of the instrument offers us the possibility to record even four–body coincidences; a recent re-measurement of $SF_6$ identified several NIPIPIPICO channels in the dataset. As

molecule sizes increase, we reach territories where it might be necessary to include a sample evaporation oven, which the instrument is prepared to host.

Negative–ion production from valence–excited species has attracted some attention in earlier studies. NIPICO, in contrast to single–channel NIY, offers the possibility to chart fragmentation pathways for complicated dissociation in (larger) molecules. We have performed some measurements on valence–excited molecules and have been able to extract NIPICO and NIPIPICO channels also there. This type of experiment is not different from measurements on core–excited species. However, the interpretation of the yields will differ and urges us to gain a deeper theoretical understanding of negative–ion production and fragmentation.

A possible future development of the instrumentation would be to include imaging detectors to gain information on fragment momenta. Such experiments have been performed for positive ions [36, 142], but not for NIPICO. The extraction of momentum information in this case would have to take into account the momenta of ions in both spectrometers, which is not as straightforward. Nevertheless, careful analysis and simulation should be able to alleviate this hurdle.

It was mentioned in Chapter 3 that *ChristianTOF* was designed to work together with a hemispherical electron analyser. The purpose would be to measure energy resolved electron/negative–ion coincidences (PENICO). Such experiments have been considered, but not yet performed. The main obstacle is to achieve a sufficient electron deflection in *ChristianTOF* while not disturbing electron analysis in the electron spectrometer. In present configuration, the magnetic influence of the negative particle momentum filter to the source region is significant. The magnetic field extruded by the filter has to become more localized in the *ChristianTOF* drift tube and properly shielded. I have sketched and made preliminary simulations of a filter design where a small electromagnet is inserted into the *ChristianTOF* drift tube and shielded by $\mu$-metal sheets. The design is similar to that of Schermann [46]. If this filter becomes operational, I expect that energy–resolved PENICO could be performed in a similar fashion to that to PEPICO in Paper **III**. The promises of PENICO is, similar to PEPICO, to assign negative ion production to particular final and intermediate electronic states. Such experiments have, to my knowledge, never been performed.

In was observed in Paper **II** that a portion of the negative–ion production in water is due to radiative decay. However, the magnitude could not be assessed and it could not be verified for resonances below the O 1s ionisation threshold. The indirect methods used to assess fluorescence contributions works reasonably well for water where the number of anionic fragmentation channels is very limited. Nevertheless, the yields can be probed directly by x-ray–emission/negative–ion coincidence (XENICO). A setup will be con-

| | 3 GeV ring | 1.5 GeV ring | SPF |
|---|---|---|---|
| Revolution period | 1760 ns | 320 ns | |
| Bunch separation | 10 ns | 10 ns | 10 ms |
| Natural bunch length (FWHM) | ~70 ps | ~120 ps | ~100 fs |
| Bunch length with maximum elongation (FWHM) | ~520 ps | ~670 ps | |

**Table 7.1.** *Temporal properties of the MAX IV rings. Expected pulse lengths are given both as natural bunch lengths and with maximum elongation due to Landau cavities. The ultimate performance of the ring should be in between these values. Note that bunch lengths have been converted from rms-lengths to FWHM-times. [88, 143–146]*

structed where a MCP detector is mounted close to the source region of *ChristianTOF* (standalone version) with a polyamide filter to block VUV and positive ion detection. Coincidences between (fast) x-ray photons and mass–resolved negative ions can be measured by a start–stop signal handling scheme identical to that in Paper **I**.

## 7.2 Opportunities for timing at MAX IV

MAX IV has some unique temporal properties, summarised in Table 7.1. The large bucket separation (10 ns) has been mentioned in Chapter 4. In addition, MAX IV will have exceptionally long pulses as a consequence of the bunch stretching introduced by Landau cavities. In addition to the two storage rings, MAX IV will include a short pulse facility (SPF), where 100 fs (FWHM) hard X-ray pulses will be created with 100 Hz repetition rate [88].

When comparing the temporal properties of the MAX IV storage rings with 500 MHz facilities, it should be noted that equal current implies five times higher charge per bunch in the MAX IV ring; increasing the intensity of each emitted light pulse. Any isolation of one bunch at MAX IV would therefore yield a high intensity even without increasing the charge in one bucket[1]. MAX IV rings are also planned to run with 500 mA current in top-up mode, which is higher than many comparable storage rings.

Although MAX IV was never intended to be a storage ring for timing–based experiments, its unique temporal characteristics give opportunities to exploit accelerator modes, choppers, gates and coincidence schemes to allow for timing–based instrumentation. The *Strategy Plan MAX IV Laboratory 2013–2026* mentions filling pattern development as a possible direction in a "Phase II accelerator", which will however not be given attention in early stages of operation. Recently, parts of the MAX-lab user community have raised an interest in using timing–based instrumentation at MAX IV. The first community to express an interest in timing capabilities was that of electron

[1]The general approach in single–bunch mode or hybrid mode is to fill the camshaft bunch with a much higher charge than a typical bunch in the bunch train.

and ion spectroscopy[2]. The demands include a wide range of photon energies, repetition rates and pulse lengths; both at the 3 GeV ring and the 1.5 GeV ring. Demands have been collected by a working group consisting of people from the user community and a few MAX IV staff. The group has published a science case for timing at MAX IV and arranged workshops in connection to this. A report from a workshop on timing modes at low-emittance storage rings has been published in *Synchrotron Radiation News* [147].

Taking into consideration the many recent developments presented in Chapter 4, I suggest that some of the following opportunities for timing could be considered at the MAX IV Laboratory[3]:

**Single bunch mode** – The MAX IV Detailed Designed Report [1] did not suggest that other accelerator modes than multi–bunch were considered. The accelerator design is not particularly well suited for single–bunch operation. This is due to the passive Landau cavities used to elongate the bunches[4]. When the number of filled buckets in the filling pattern is reduced, as is necessary for single–bunch operation, the elongating and stabilizing effect is reduced. Consequently, the design value for the single–bunch charge (5 nC, 16 mA) could be harder to sustain.

If a single–bunch mode would be developed at the 1.5 GeV ring, it would have a 320 ns repetition rate (3.1 MHz). Compared to many other rings with dedicated single–bunch modes (see table 4.1), this is quite high. Nevertheless, it is sufficient for many applications of electron time–of–flight [106]. Since transmission of such instruments are significantly higher than that of a hemispherical analyser, a net gain in transmission would be expected even with a lower intensity of the single bunch. Ovsyannikov *et al.* [107] have identified low dose electron spectroscopy as one area where angle-resolved time–of–flight spectrometers are beneficial. Studies of sensitive and fragile systems require very small light intensities and consequently need high transmission instruments for an efficient data collection; such low dose studies using ARTOF has been reported from BESSY [118]. Since single–bunch repetition rate at BESSY is 1.25 MHz, a 3.1 MHz single–bunch rate would theoretically increase the collection efficiency by a factor 2.5, given that the same dose is applied during a shorter time.

Time-resolved photoelectron spectroscopy (tr-PES) has been pointed out as a strong case for the ARTOF. These experiments are of two types: those occurring on a long time-scale

[2] At a later stage, other communities have expressed similar interests.

[3] See also Paper **V**.

[4] "Passive" cavities imply that their properties are dependent on the current passing through them.

(compared to the repetition rate of the light) where the time–evolution is directly observable in the spectra, and pump–probe experiments. The former would benefit from the high single–bunch repetition rate of the MAX IV 1.5 GeV ring, since the repetition rate sets the time resolution. The latter, however, has a severe drawback at MAX IV due to the long bunches.

**Resonant pulse picking** – The outcome of resonant pulse picking [79] is similar to a single–bunch mode. The benefit would be the simultaneous operation of high–intensity experiments and experiments with single–bunch requirements. A particularly intriguing possibility is to operate resonant pulse picking without hybrid mode (in order to run MAX IV in stable operation at full intensity). The 10 ns repetition rate of MAX IV would be an advantage in this regard. Due to the intrinsically lower horizontal emittance of MAX IV 3 GeV ring compared to BESSY, one could possibly expect a more efficient separation of resonantly excited light from the multi–bunch train. Implementation of this scheme at MAX IV has been inhibited by the lack of a bunch–by–bunch feedback system in the accelerator lattice. Resonant pulse picking is probably of larger interest for the 1.5 GeV ring, which is not optimized for low emittance.

**Pseudo single bunch** – The applicability of PSB [76] to MAX IV is largely determined by the highest possible speed of the kicker magnet. In present operation, the PSB scheme demands a hybrid mode, but development of kicker magnets is ongoing, and a pulse length below 20 ns is not unthinkable. A PSB scheme operating on MAX IV multi–bunch filling pattern could have huge benefits for timing–based instrumentation at both rings. A proper PSB is very versatile and could offer differing timing modes for users at different beamlines on demand.

**Choppers** – To allow for instrumentation with sub-single–bunch requirements, MAX IV will have to make use of choppers. All choppers currently in use at storage rings require dedicated single–bunch or hybrid modes. Two choppers have reported window times below 320 ns: The ESRF chopper [94] and the MHz pulse selector [97]. The former is a hard X-ray chopper and offer features which are not necessary at the small ring, which is intended for soft X-rays/VUV. It also shows a repetition rate which is at least one order of magnitude lower than optimum for any magnetic bottle spectrometer. However, would low frequency requirements arise at the large ring, this chopper paired with a hybrid or single–bunch mode would be a viable alternative. Using a modified version of the MHz pulse selector could satisfy the users of sub-single–bunch instrumentation at the large or small ring, given that a single–bunch mode is available. It would require either that the present disc

is run at a slightly lower frequency[5] or that a new disc is fabricated with slot positions tailored for MAX IV. The latter would allow use of long magnetic–bottle–type instruments.

A MHz pulse selector could decrease the required hybrid window close to 70 ns. This would open up the possibility for a hybrid mode with a removal of 6 out of 32 bunches in the small ring, which implies that 80% of the intensity could remain. Also, the machine operation would probably be more stable. If such a scheme could be created, it would open up for simultaneous single–bunch and high intensity instrumentation at the small ring.

**Coincidences with hemispherical analysers** – Coincidence experiments using hemispherical analysers in coincidence with eTOF instruments can benefit from the temporal properties of MAX IV – without any changes to the timing properties. Several high–resolution electron/electron coincidence experimental stations have been commissioned recently where such instruments are used [104, 134]. I have suggested the use of a similar setup at MAX IV where the 10 ns separation of light pulses is exploited. This topic is treated in Paper **V** and in more detail in Chapter 6.

## 7.3 Future development for ARTOF gating

Detector and front gating of the ARTOF is in different stages of functionality. For the detector gating (GAME) scheme, tuning the hardware and the proper gate pulse is a complex task and there is room for further improvements. For future development we should seek a deeper theoretical understanding of the signal handling in the GAME. The possibility to include a band pass filter to the MCP has not yet been studied.

We have seen that high energy contributions in the photon beam decrease the efficiency of the gate. This could be improved with a photon energy filter in the beamline. The parameters of the lens should be further optimized to account for focusing conditions at relevant gating potentials, in order to fully preserve the resolution of the instrument. This must include a full implementation of the gating scheme in the lens transfer matrices. The variability of the gating pulse should be taken into account.

The influence of the gating pulse to the detector should be studied to allow for higher gate amplitude. One option which has not yet been pursued is to introduce a signal handling scheme where gate pulse noise is filtered from the MCP response before reading in the CFD. The physical design of the mesh ensemble could possibly be

[5] Reducing rotation speed by 20% would allow selecting every third single–bunch and mimic ∼ 1 MHz repetition rate.

changed to further reduce the signal transmission from mesh to detector.

The necessity of future development should nevertheless be weighted against the practical need of a gating scheme. With the start of the BESSY–VSR project, the need for detector gating at BESSY has diminished. Its applicability to other facilities depend on the temporal structure of the bunch pattern.

The front gate concept has been less advanced, and a further development will be faced with large practical difficulties. If development of the front gate scheme is envisioned, it should be focused on a more suitable pulse generator together with a renewed gate design. For the physical design, the gate must be changed to allow a closer mount relative to the spectrometer. Simulations have shown that a close mount does not significantly disturb electron trajectories for the pre–lens. If the front–gating scheme is to be extended to other versions of the ARTOF, gate designs should be further discussed in collaboration with the manufacturer.

A setup containing a high frequency solid–state switch should be developed. As mentioned, such switches with suitable characteristics are commercially available, but will require a liquid cooling system. Further tests could be performed upon completion of the new CoESCA end–station at BESSY, which will include two ARTOF instruments of different designs. This end–station will be operational in 2016.

It has become obvious since 2011 when the front–gate plans were first laid out that MAX IV is not prepared to accept an ARTOF spectrometer in stand–alone operation at a beamline without changes to the accelerator timing, as discussed above. Therefore, accelerator and beamline adaptations are, in my view, much more promising and should be pursued rather than a further development of the front-gate scheme.

# REFERENCES


1. MAX IV Laboratory. *MAX IV Detailed Design Report*. `http://www.maxlab.lu.se/maxlab/max4/DDR_public` (2010).

2. Stråhlman C. *Electronic state dependence in dissociation of core-excited water*. `http://lup.lub.lu.se/student-papers/record/1988390` (2011).

3. Stråhlman C. *On the Challenges for Time–of–Flight Electron Spectroscopy at Storage Rings*. MAX IV Laboratory, Lund University (2014). ISBN 978-91-7623-165-4.

4. Berkowitz J. *Atomic and Molecular Photoabsorption: Partial Cross Sections*. Elsevier Science (2015). ISBN 9780128019580.

5. Piancastelli MN, Sankari R, Sorensen S, De Fanis A, Yoshida H, Kitajima M, Tanaka H, and Ueda K. *Resonant Auger decay of above-threshold core-excited $H_2O$*. Phys. Rev. A, **71**:010703 (2005). doi:10.1103/PhysRevA.71.010703.

6. Banwell CN and McCash EM. *Fundamentals of Molecular Spectroscopy*. Mcgraw-Hill, 4 edition (1994). ISBN 978-0-077-07976-5.

7. Einstein A. *Über einen die Erzeugung und Verwandlung des Lichtes betreffenden heuristischen Gesichtspunkt*. Ann. Phys., **322**(6):132–148 (1905). doi:10.1002/andp.19053220607.

8. Brundle CR and Turner DW. *High resolution molecular photoelectron spectroscopy. II. Water and deuterium oxide*. Proc. Roy. Soc. A, **307**(1488):27–36 (1968). doi:10.2307/2416184.

9. Siegbahn K. *Electron spectroscopy – an outlook*. J. Electron Spectrosc. Relat. Phenom., **5**(1):3–97 (1974). doi:10.1016/0368-2048(74)85005-X.

10. Sankari R, Ehara M, Nakatsuji H, Senba Y, Hosokawa K, Yoshida H, Fanis AD, Tamenori Y, Aksela S, and Ueda K. *Vibrationally resolved O 1s photoelectron spectrum of water*. Chem. Phys. Lett., **380**(5–6):647–653 (2003). doi:10.1016/j.cplett.2003.08.108.

11. Myneni S, Luo Y, Näslund LA, Cavalleri M, Ojamäe L et al. *Spectroscopic probing of local hydrogen-bonding structures in liquid water*. J. Phys.: Condens. Matter, **14**(8):L213 (2002). doi:10.1088/0953-8984/14/8/106.

12. Bartels-Rausch T. *Ten things we need to know about ice and snow*. Nature, **494**:27–29 (2013). doi:10.1038/494027a.

13. Bartels-Rausch T, Bergeron V, Cartwright JHE, Escribano R, Finney JL et al. *Ice structures, patterns, and processes: A view across the icefields*. Rev. Mod. Phys., **84**:885–944 (2012). doi:10.1103/RevModPhys.84.885.

14. Nilsson A and Pettersson LGM. *Perspective on the structure of liquid water*. Chem. Phys., **389**(1–3):1–34 (2011). doi:10.1016/j.chemphys.2011.07.021.

15. Nilsson A and Pettersson LGM. *The structural origin of anomalous properties of liquid water.* Nat. Comm., **6**:8998 (2015). doi:10.1038/ncomms9998.

16. Kivimäki A, de Simone M, Coreno M, Feyer V, Melero García E, Álvarez Ruiz J, Richter R, and Prince KC. *Observation of core-hole double excitations in water using fluorescence spectroscopy.* Phys. Rev. A, **75**:014503 (2007). doi:10.1103/PhysRevA.75.014503.

17. Sankari R, Ehara M, Nakatsuji H, Fanis AD, Aksela H, Sorensen S, Piancastelli M, Kukk E, and Ueda K. *High resolution O 1s photoelectron shake-up satellite spectrum of* $H_2O$. Chem. Phys. Lett., **422**(1–3):51–57 (2006). doi:10.1016/j.cplett.2006.02.018.

18. Mucke M, Eland J, Takahashi O, Linusson P, Lebrun D, Ueda K, and Feifel R. *Formation and decay of core–orbital vacancies in the water molecule.* Chem. Phys. Lett., **558**:82–87 (2013). doi:10.1016/j.cplett.2012.11.094.

19. Siegbahn H, Asplund L, and Kelfve P. *The Auger electron spectrum of water vapour.* Chem. Phys. Lett., **35**(3):330–335 (1975). doi:10.1016/0009-2614(75)85615-6.

20. Piancastelli MN, Kempgens B, Hergenhahn U, Kivimäki A, Maier K, Rüdel A, and Bradshaw AM. *Nonlinear dispersion in resonant Auger decay of* $H_2O$ *molecules.* Phys. Rev. A, **59**:1336–1340 (1999). doi:10.1103/PhysRevA.59.1336.

21. Hjelte I, Karlsson L, Svensson S, Fanis AD, Carravetta V et al. *Angular distribution of different vibrational components of the X and B states reached after resonant Auger decay of core-excited* $H_2O$*: Experiment and theory.* J. Chem. Phys., **122**(8):084306 (2005). doi:10.1063/1.1850898.

22. Nordgren J, Werme LP, Ågren H, Nordling C, and Siegbahn K. *The x-ray emission spectrum of water.* J. Phys. B: At. Mol. Phys., **8**(2):L18 (1975). doi:10.1088/0022-3700/8/2/00.

23. Kashtanov S, Augustsson A, Luo Y, Guo JH, Såthe C, Rubensson JE, Siegbahn H, Nordgren J, and Ågren H. *Local structures of liquid water studied by x-ray emission spectroscopy.* Phys. Rev. B, **69**:024201 (2004). doi:10.1103/PhysRevB.69.024201.

24. Weinhardt L, Benkert A, Meyer F, Blum M, Wilks RG, Yang W, Bär M, Reinert F, and Heske C. *Nuclear dynamics and spectator effects in resonant inelastic soft x-ray scattering of gas-phase water molecules.* J. Chem. Phys., **136**(14):144311 (2012). doi:10.1063/1.3702644.

25. Gejo T, Oura M, Kuniwake M, Honma K, and Harries JR. *Dissociation and recapture dynamics in* $H_2O$ *following O 1s inner-shell excitation.* J. Phys.: Conf. Ser., **288**:012023 (2011). doi:10.1088/1742-6596/288/1/012023.

26. Harries JR, Gejo T, Honma K, Kuniwake M, Sullivan JP, Lebech M, and Azuma Y. *Long-lived, highly excited neutral hydrogen atom production following oxygen 1s photoexcitation of gas-phase water molecules.* J. Phys. B: At., Mol. Opt. Phys., **44**(9):095101 (2011). doi:10.1088/0953-4075/44/9/095101.

27. Gejo T, Ikegami T, Honma K, Takahashi O, Shigemasa E, Hikosaka Y, and Tamenori Y. *Dynamics of oxygen Rydberg atom generation following O 1s inner-shell excitation of* $H_2O$. J. Chem. Phys., **140**(21):214310 (2014). doi:10.1063/1.4880557.

28. Norwood K, Ali A, and Ng CY. *A photoelectron–photoion coincidence study of* $H_2O$, $D_2O$, *and* $(H_2O)_2$. J. Chem. Phys., **95**(11):8029–8037 (1991). doi:10.1063/1.461334.

29. Hunniford CA, Scully SWJ, Dunn KF, and Latimer CJ. *Fragment anion spectroscopy of water in the inner and outer valence regions.* J. Phys. B: At., Mol. Opt. Phys., **40**(6):1225 (2007). doi:10.1088/0953-4075/40/6/012.

30. Piancastelli MN, Hempelmann A, Heiser F, Gessner O, Rüdel A, and Becker U. *Resonant photofragmentation of water at the oxygen K edge by high-resolution ion-yield spectroscopy.* Phys. Rev. A, **59**:300–306 (1999). doi:10.1103/PhysRevA.59.300.

31. Stolte WC, Sant'Anna MM, Öhrwall G, Dominguez-Lopez I, Piancastelli MN, and Lindle DW. *Photofragmentation dynamics of core-excited water by anion-yield spectroscopy.* Phys. Rev. A, **68**:022701 (2003). doi:10.1103/PhysRevA.68.022701.

32. Eroms M, Vendrell O, Jungen M, Meyer HD, and Cederbaum LS. *Nuclear dynamics during the resonant Auger decay of water molecules.* J. Chem. Phys., **130**(15):154307 (2009). doi:10.1063/1.3117902.

33. Hjelte I, Piancastelli M, Fink R, Björneholm O, Bässler M et al. *Evidence for ultrafast dissociation of molecular water from resonant Auger spectroscopy.* Chem. Phys. Lett., **334**(1–3):151–158 (2001). doi:10.1016/S0009-2614(00)01434-2.

34. Kato M, Odagiri T, Kodama K, Murata M, Kameta K, and Kouchi N. *Doubly excited states of water in the inner valence range.* J. Phys. B: At., Mol. Opt. Phys., **37**(15):3127 (2004). doi:10.1088/0953-4075/37/15/009.

35. Kivimäki A, Coreno M, Richter R, Álvarez Ruiz J, Melero Garcia E, de Simone M, Feyer V, Vall-llosera G, and Prince KC. *Fluorescence emission following core excitations in the water molecule.* J. Phys. B: At., Mol. Opt. Phys., **39**(5):1101 (2006). doi:10.1088/0953-4075/39/5/009.

36. Laksman J, Månsson EP, Sankari A, Céolin D, Gisselbrecht M, and Sorensen SL. *Rapid bond rearrangement in core-excited molecular water.* Phys. Chem. Chem. Phys., **15**:19322–19329 (2013). doi:10.1039/C3CP52625A.

37. Arion T and Hergenhahn U. *Coincidence spectroscopy: Past, present and perspectives.* J. Electron Spectrosc. Relat. Phenom., **200**:222–231 (2015). doi:10.1016/j.elspec.2015.06.004.

38. Arion T, Püttner R, Lupulescu C, Ovsyannikov R, Förstel M et al. *New insight into the Auger decay process in $O_2$: The coincidence perspective.* J. Electron Spectrosc. Relat. Phenom., **185**(8–9):234–243 (2012). doi:10.1016/j.elspec.2012.06.010.

39. Eland JH. *Complete double photoionisation spectra of small molecules from TOF-PEPECO measurements.* Chem. Phys., **294**(2):171–186 (2003). doi:10.1016/j.chemphys.2003.08.001.

40. Wiley WC and McLaren IH. *Time-of-flight mass spectrometer with improved resolution.* Rev. Sci. Instrum., **26**(12):1150–1157 (1955). doi:10.1063/1.1715212.

41. Sanzone G. *Energy resolution of the conventional time-of-flight mass spectrometer.* Rev. Sci. Instrum., **41**(5):741–742 (1970). doi:10.1063/1.1684631.

42. Plekan O, Coreno M, Feyer V, Moise A, Richter R, de Simone M, Sankari R, and Prince KC. *Electronic state resolved PEPICO spectroscopy of pyrimidine.* Phys. Scr., **78**(5):058105 (2008). doi:10.1088/0031-8949/78/05/058105.

43. Sankari R. Private communication (2012).

44. Chambers A, Fitch RK, and Halliday BS. *Basic Vacuum Technology.* IOP Publishing, 2 edition (1998). ISBN 0-750-30495-2.

45. Trajmar S and Hall RI. *Dissociative electron attachment in* $H_2O$ *and* $D_2O$*: energy and angular distribution of* $H^-$ *and* $D^-$ *fragments.* J. Phys. B: At. Mol. Phys., **7**(16):L458 (1974). doi:10.1088/0022-3700/7/16/009.

46. Schermann C, Cadez I, Delon P, Tronc M, and Hall RI. *A simple momentum filter for the separation of negative ions from electrons.* J. Phys. E: Sci. Instrum., **11**(8):746 (1978). doi:10.1088/0022-3735/11/8/009.

47. Moore JH, Davis CC, Coplan MA, and Greer SC. *Building Scientific Apparatus.* Cambridge University Press, 4 edition (2009). ISBN 0-521-87858-6.

48. Hikosaka Y and Eland JHD. *New results on photoion pair formation from application of the velocity imaging photoionisation coincidence technique.* Rapid Commun. Mass Spectrom., **14**(23):2305–2311 (2000). doi:10.1002/1097-0231(20001215)14:23<2305::AID-RCM167>3.0.CO;2-I.

49. Yoshida H and Mitsuke K. *Observation of doubly excited Rydberg states of* $N_2O$ *by positive ion–negative ion coincidence spectroscopy.* J. Chem. Phys., **100**(12):8817–8824 (1994). doi:10.1063/1.466736.

50. Rühl E and Flesch R. *Mechanism of anion formation in* C 1$s \rightarrow \pi^*$*–excited carbon dioxide.* J. Chem. Phys., **121**(11):5322–5327 (2004). doi:10.1063/1.1784780.

51. *SIMION.* `http://simion.com/`.

52. Hartman T, Juranić PN, Collins K, Reilly B, Makoutz E, Appathurai N, and Wehlitz R. *Photo-double-ionization mechanisms in aromatic hydrocarbons.* Phys. Rev. A, **87**:063403 (2013). doi:10.1103/PhysRevA.87.063403.

53. Kukk E, Sankari R, Huttula M, Sankari A, Aksela H, and Aksela S. *New electron-ion coincidence setup: Fragmentation of acetonitrile following N 1s core excitation.* J. Electron Spectrosc. Relat. Phenom., **155**(1–3):141–147 (2007). doi:10.1016/j.elspec.2006.10.011.

54. Huttula M, Harkoma M, Nõmmiste E, and Aksela S. *A multipurpose electron-ion spectrometer for measurements with synchrotron radiation.* Nucl. Instrum. Methods Phys. Res. A, **467–468**:1514–1518 (2001). doi:10.1016/S0168-9002(01)00741-0.

55. Eland J. *Photoelectron–photoion coincidence spectroscopy: I. Basic principles and theory.* Int. J. Mass spectrom., **8**(2):143–151 (1972). doi:10.1016/0020-7381(72)80004-4.

56. Kivimäki A, Álvarez-Ruiz J, Sergo R, and Richter R. *Production of excited H atoms at the C 1s edge of the methane molecule studied by VUV-photon–photoion and metastable-fragment–photoion coincidence experiments.* Phys. Rev. A, **88**:043412 (2013). doi:10.1103/PhysRevA.88.043412.

57. Merkt F. *Molecules in high Rydberg states.* Annu. Rev. Phys. Chem., **48**(1):675–709 (1997). doi:10.1146/annurev.physchem.48.1.675.

58. Rydberg JR. *Recherches sur la constitution des spectres d'emission des elements chimique.* Den Kungliga Svenska Vetenskapsakademiens Handlingar, **23**(11) (1889).

59. Wille K. *The Physics of Particle Accelerators: An Introduction.* Oxford University Press, USA (2001). ISBN 0-19-850549-3.

60. Andersson Å, Eriksson M, Lindgren LJ, Röjsel P, and Werin S. *The MAX II synchrotron radiation storage ring.* Nucl. Instrum. Methods Phys. Res. A, **343**(2-3):644 – 649 (1994). doi:10.1016/0168-9002(94)90248-8.

61. Sjöström M, Wallén E, Eriksson M, and Lindgren LJ. *The MAX III storage ring.* Nucl. Instrum. Methods Phys. Res. A, **601**(3):229–244 (2009). doi:10.1016/j.nima.2008.12.195.

62. Byrd JM and Georgsson M. *Lifetime increase using passive harmonic cavities in synchrotron light sources.* Phys. Rev. ST Accel. Beams, **4**:030701 (2001). doi:10.1103/PhysRevSTAB.4.030701.

63. Georgsson M. *Landau cavities in third generation synchrotron light sources.* In *Particle Accelerator Conference, 2001. PAC 2001.*, volume 4, pp. 2689–2691 vol.4 (2001). doi:10.1109/PAC.2001.987874.

64. Bassi G, Blednykh A, Krinsky S, and Rose J. *Self-consistent simulations of passive Landau cavity effects.* In *Proceedings of PAC2013, Pasadena, CA USA* (2013).

65. Hertel N and Vrønning Hoffmann S. *ASTRID2: A new Danish low-emittance SR source.* Synchrotron Radiat. News, **24**(1):19–23 (2011). doi:10.1080/08940886.2011.550553.

66. Bocchetta C, Goryl P, Królas K, Młynarczyk M, Stankiewicz MJ et al. *Project status of the Polish synchrotron radiation facility SOLARIS.* In *Proceedings of IPAC2011, San Sebastian, Spain*, p. THPC054 (2011).

67. BESSY. *BESSY II launches new filling pattern in user mode.* `http://www.helmholtz-berlin.de/forschung/oe/fg/mi-synchrotron-radiation/synchrotron/photons/x-ray-pulses/bunch/index_de.html` (2015).

68. Abo-Bakr M, Anders W, Kuske P, and Wustefeld G. *Bunch length measurements at BESSY.* In *Proceedings of the Particle Accelerator Conference, 2003. PAC 2003.*, volume 5, pp. 3020–3022 (2003). doi:10.1109/PAC.2003.1289800.

69. ALS. *ALS storage ring parameters.* `http://www-als.lbl.gov/index.php/beamlines/storage-ring-parameters.html%5D` (2014).

70. ESRF. *ESRF performance.* `http://www.esrf.eu/Accelerators/Performance/` (2014).

71. Bergeard N, Silly MG, Krizmancic D, Chauvet C, Guzzo M et al. *Time-resolved photoelectron spectroscopy using synchrotron radiation time structure.* J. Synchrotron Rad., **18**(2):245–250 (2011). doi:10.1107/S0909049510052301.

72. *SPring-8 storage ring.* `http://www.spring8.or.jp/en/facilities/accelerators/storage_ring/` (2014-05-12).

73. Milas N and Stingelin L. *Impact of filling patterns on bunch length and lifetime at the SLS.* In *Proceedings of IPAC2010, Kyoto, Japan*, p. THPE084 (2010).

74. Sun C, Portmann G, Hertlein M, Kirz J, and Robin DS. *Pseudo-single-bunch with adjustable frequency: A new operation mode for synchrotron light sources.* Phys. Rev. Lett., **109**:264801 (2012). doi:10.1103/PhysRevLett.109.264801.

75. Sun C, Portmann G, Hertlein M, Kirz J, Marcus MA, and Robin DS. *Pseudo-single-bunch with adjustable frequency.* Synchrotron Radiat. News, **26**(3):9–13 (2013). doi:10.1080/08940886.2013.791209.

76. Sun C, Robin D, Steier C, and Portman G. *Relalization of Pseudo Single Bunch operation with adjustable frequency.* In *Proceedings of IPAC2015, Richmond, VA, USA*, p. WEXB3 (2015).

77. Nadolski LS, Lavieville JP, Lebasque P, Nadji A, Ricaud JP, Silly M, and Sirotti F. *First measurements with a kicked off axis bunch for Pseudo Single Bunch mode studies at SOLEIL.* In *Proceedings of IPAC2011, San Sebastian, Spain*, p. THPC005 (2011).

78. Couprie ME, Nadolski LS, Nagaoka R, Brunelle P, Loulergue A, Tordeux MA, Lamarre JF, and Nadji A. *Versatile modes of operation to meet user needs at SOLEIL.* Synchrotron Radiat. News, **26**(3):14–18 (2013). doi:10.1080/08940886.2013.791210.

79. Holldack K, Ovsyannikov R, Kuske P, Müller R, Schälicke A et al. *Single bunch X-ray pulses on demand from a multi–bunch synchrotron radiation source.* Nat. Commun., **5**:4010 (2014). doi:10.1038/ncomms5010.

80. Sun C, Robin DS, Steier C, and Portmann G. *Characterization of pseudosingle bunch kick-and-cancel operational mode.* Phys. Rev. ST Accel. Beams, **18**:120702 (2015). doi:10.1103/PhysRevSTAB.18.120702.

81. Murphy JB. *Synchrotron light source data book.* AIP Conf. Proc., **249**(2):1939–2011 (1992). doi:10.1063/1.41969.

82. Yamamoto S and Matsuda I. *Time-resolved photoelectron spectroscopies using synchrotron radiation: Past, present, and future.* J. Phys. Soc. Jpn., **82**(2):021003 (2013). doi:10.7566/JPSJ.82.021003.

83. Müller AS. *Short-pulse operation of storage ring light sources.* In *Proceedings of IPAC2013, Shanghai, China*, p. TUXB201 (2013).

84. Abo-Bakr M, Feikes J, Holldack K, Wüstefeld G, and Hübers HW. *Steady-state far-infrared coherent synchrotron radiation detected at BESSY II.* Phys. Rev. Lett., **88**:254801 (2002). doi:10.1103/PhysRevLett.88.254801.

85. Wüstefeld G, Jankowiak A, Knobloch J, and Ries M. *Simultaneous long and short electron bunches in the BESSY II storage ring.* In *Proceedings of IPAC2011, San Sebastian, Spain*, p. THPC014 (2011).

86. Schoenlein R, Chattopadhyay S, Chong H, Glover T, Heimann P, Leemans W, Shank C, Zholents A, and Zolotorev M. *Generation of femtosecond X-ray pulses via laser–electron beam interaction.* Appl. Phys. B, **71**(1):1–10 (2000). doi:10.1007/PL00021152.

87. Khan S, Holldack K, Kachel T, Mitzner R, and Quast T. *Femtosecond undulator radiation from sliced electron bunches.* Phys. Rev. Lett., **97**:074801 (2006). doi:10.1103/PhysRevLett.97.074801.

88. Werin S, Thorin S, Eriksson M, and Larsson J. *Short pulse facility for MAX–lab.* Nucl. Instrum. Methods Phys. Res. A, **601**(1-2):98–107 (2009). doi:10.1016/j.nima.2008.12.106.

89. Husheer SLG, Cole JM, d' Almeida T, and Teat SJ. *A prototype chopper for synchrotron time-resolved crystallographic measurements.* Rev. Sci. Instrum., **81**(4):043905 (2010). doi:10.1063/1.3358939.

90. McPherson A, Lee WK, and Mills DM. *A synchronized rotating crystal x-ray beam chopper.* Rev. Sci. Instrum., **73**(8):2852–2855 (2002). doi:10.1063/1.1485780.

91. Kosciesza D and Bartunik HD. *Extraction of single bunches of synchrotron radiation from storage rings with an X-ray chopper based on a rotating mirror.* J. Synchrotron Rad., **6**(5):947–952 (1999). doi:10.1107/S0909049599003404.

92. Plogmaker S, Linusson P, Eland JHD, Baker N, Johansson EMJ, kan Rensmo H, Feifel R, and Siegbahn H. *Versatile high-repetition-rate phase-locked chopper system for fast timing experiments in the vacuum ultraviolet and x-ray spectral region.* Rev. Sci. Instrum., **83**(1):013115 (2012). doi:10.1063/1.3677329.

93. Ito K, Penent F, Hikosaka Y, Shigemasa E, Suzuki IH, Eland JHD, and Lablanquie P. *Application of a simple asynchronous mechanical light chopper to multielectron coincidence spectroscopy.* Rev. Sci. Instrum., **80**(12):123101 (2009). doi:10.1063/1.3258200.

94. Cammarata M, Eybert L, Ewald F, Reichenbach W, Wulff M et al. *Chopper system for time resolved experiments with synchrotron radiation.* Rev. Sci. Instrum., **80**(1):015101 (2009). doi:10.1063/1.3036983.

95. Gembicky M, Oss D, Fuchs R, and Coppens P. *A fast mechanical shutter for submicrosecond time-resolved synchrotron experiments.* J. Synchrotron Rad., **12**(5):665–669 (2005). doi:10.1107/S090904950501770X.

96. McPherson A, Wang J, Lee PL, and Mills DM. *A new high-speed beam chopper for time-resolved X-ray studies.* J. Synchrotron Radiat., **7**(1):1–4 (2000). doi:10.1107/S0909049599014582.

97. Förster DF, Lindenau B, Leyendecker M, Janssen F, Winkler C, Schumann FO, Kirschner J, Holldack K, and Föhlisch A. *Phase-locked MHz pulse selector for x-ray sources.* Opt. Lett., **40**(10):2265–2268 (2015). doi:10.1364/OL.40.002265.

98. Gembicky M and Coppens P. *On the design of ultrafast shutters for time-resolved synchrotron experiments.* J. Synchrotron Rad., **14**(1):133–137 (2007). doi:10.1107/S0909049506041835.

99. BESSY. *BESSY II launches new filling pattern in user mode.* `http://www.helmholtz-berlin.de/pubbin/news_seite?nid=14265;sprache=en;typoid=3228` (2016-03-02).

100. Wannberg B. *Electron optics development for photo-electron spectrometers.* Nucl. Instrum. Methods Phys. Res. A, **601**(1–2):182–194 (2009). doi:10.1016/j.nima.2008.12.156.

101. Dörner R, Mergel V, Jagutzki O, Spielberger L, Ullrich J, Moshammer R, and Schmidt-Böcking H. *Cold target recoil ion momentum spectroscopy: A "momentum microscope" to view atomic collision dynamics.* Phys. Rep., **330**(2–3):95–192 (2000). doi:10.1016/S0370-1573(99)00109-X.

102. Bachrach RZ, Brown FC, and Hagström SBM. *Photoelectron spectroscopy by time-of-flight technique using synchrotron radiation.* J. Vac. Sci. Technol., **12**(1):309–312 (1975). doi:10.1116/1.568772.

103. Hemmers O, Whitfield SB, Glans P, Wang H, Lindle DW, Wehlitz R, and Sellin IA. *High-resolution electron time-of-flight apparatus for the soft x-ray region.* Rev. Sci. Instrum., **69**(11):3809 (1998). doi:10.1063/1.1149183.

104. Ulrich V, Barth S, Lischke T, Joshi S, Arion T, Mucke M, Förstel M, Bradshaw AM, and Hergenhahn U. *Photoelectron–Auger electron coincidence spectroscopy of free molecules: New experiments.* J. Electron Spectrosc. Relat. Phenom., **183**(1–3):70–79 (2011). doi:10.1016/j.elspec.2010.03.001.

105. Bostedt C, Bozek JD, Bucksbaum PH, Coffee RN, Hastings JB et al. *Ultra-fast and ultra-intense X-ray sciences: first results from the Linac Coherent Light Source free-electron laser.* J. Phys. B: At., Mol. Opt. Phys., **46**(16):164003 (2013). doi:10.1088/0953-4075/46/16/164003.

106. Öhrwall G, Karlsson P, Wirde M, Lundqvist M, Andersson P et al. *A new energy and angle resolving electron spectrometer — First results.* J. Electron Spectrosc. Relat. Phenom., **183**(1–3):125–131 (2011). doi:10.1016/j.elspec.2010.09.009.

107. Ovsyannikov R, Karlsson P, Lundqvist M, Lupulescu C, Eberhardt W, Föhlisch A, Svensson S, and Mårtensson N. *Principles and operation of a new type of electron spectrometer - ArTOF.* J. Electron Spectrosc. Relat. Phenom., **191**:92–103 (2013). doi:10.1016/j.elspec.2013.08.005.

108. *Time of Flight spectrometers THEMIS 1000 / THEMIS 600 — Technical note.* `http://www.specs.de/cms/upload/PDFs/ApplNotes/THEMIS/TNote_THEMIS_performance_overview.pdf` (2014-04-11).

109. Eland JHD, Vieuxmaire O, Kinugawa T, Lablanquie P, Hall RI, and Penent F. *Complete two-electron spectra in double photoionization: The rare gases Ar, Kr, and Xe.* Phys. Rev. Lett., **90**:053003 (2003). doi:10.1103/PhysRevLett.90.053003.

110. Kruit P and Read FH. *Magnetic field paralleliser for $2\pi$ electron-spectrometer and electron-image magnifier.* J. Phys. E: Sci. Instrum., **16**(4):313 (1983). doi:10.1088/0022-3735/16/4/016.

111. Cha CY, Ganteför G, and Eberhardt W. *New experimental setup for photoelectron spectroscopy on cluster anions.* Rev. Sci. Instrum., **63**(12):5661–5666 (1992). doi:10.1063/1.1143397.

112. Eland J, Linusson P, Mucke M, and Feifel R. *Homonuclear site-specific photochemistry by an ion-electron multi-coincidence spectroscopy technique.* Chem. Phys. Lett., **548**:90–94 (2012). doi:10.1016/j.cplett.2012.08.018.

113. Penent F, Lablanquie P, Hall R, Palaudoux J, Ito K, Hikosaka Y, Aoto T, and Eland J. *Coincidence Auger spectroscopy.* J. Electron Spectrosc. Relat. Phenom., **144-147**:7–11 (2005). doi:10.1016/j.elspec.2005.01.187.

114. Mucke M, Förstel M, Lischke T, Arion T, Bradshaw AM, and Hergenhahn U. *Performance of a short "magnetic bottle" electron spectrometer.* Rev. Sci. Instrum., **83**(6):063106 (2012). doi:10.1063/1.4729256.

115. Mårtensson N, Baltzer P, Brühwiler P, Forsell JO, Nilsson A, Stenborg A, and Wannberg B. *A very high resolution electron spectrometer.* J. Electron Spectrosc. Relat. Phenom., **70**(2):117–128 (1994). doi:10.1016/0368-2048(94)02224-N.

116. Gelius U, Wannberg B, Baltzer P, Fellner-Feldegg H, Carlsson G, Johansson CG, Larsson J, Münger P, and Vegerfors G. *A new ESCA instrument with improved surface sensitivity, fast imaging properties and excellent energy resolution.* J. Electron Spectrosc. Relat. Phenom., **52**:747–785 (1990). doi:10.1016/0368-2048(90)85063-F.

117. King PDC, Hatch RC, Bianchi M, Ovsyannikov R, Lupulescu C et al. *Large tunable Rashba spin splitting of a two-dimensional electron gas in $Bi_2Si_3$.* Phys. Rev. Lett., **107**:096802 (2011). doi:10.1103/PhysRevLett.107.096802.

118. Vollmer A, Ovsyannikov R, Gorgoi M, Krause S, Oehzelt M et al. *Two dimensional band structure mapping of organic single crystals using the new generation electron energy analyzer ARTOF.* J. Electron Spectrosc. Relat. Phenom., **185**(3–4):55–60 (2012). doi:10.1016/j.elspec.2012.01.003.

119. Ogawa M, Yamamoto S, Kousa Y, Nakamura F, Yukawa R et al. *Development of soft x-ray time-resolved photoemission spectroscopy system with a two-dimensional angle-resolved time-of-flight analyzer at SPring-8 BL07LSU.* Rev. Sci. Instrum., **83**(2):023109 (2012). doi:10.1063/1.3687428.

120. Glover TE, Ackermann GD, Hussain Z, and Padmore HA. *Laser pump and X-ray probe surface photovoltage spectroscopy on Si(111).* J. Mod. Opt., **51**(16–18):2805–2811 (2004). doi:10.1080/09500340408231839.

121. Tanaka S, Dylan Moré S, Takahashi K, and Kamada M. *Dynamics of surface photovoltage effects on clean and negative electron affinity surfaces of p-GaAs(100).* J. Phys. Soc. Jpn., **72**(3):659–663 (2003). doi:10.1143/JPSJ.72.659.

122. Takahashi K, Kondo Y, Azuma J, and Kamada M. *Beamline for high-resolution angle-resolved photoemission at Saga Light Source.* J. Electron Spectrosc. Relat. Phenom., **144–147**:1093–1096 (2005). doi:10.1016/j.elspec.2005.01.184.

123. Takahashi K, Azuma J, Tokudomi S, and Kamada M. *Development of the experimental system for time– and angle–resolved photoemission spectroscopy.* AIP Conf. Proc., **879**(1):1218–1221 (2007). doi:10.1063/1.2436283.

124. Guilhaus M. *Special feature: Tutorial. Principles and instrumentation in time-of-flight mass spectrometry. Physical and instrumental concepts.* J. Mass Spectrom., **30**(11):1519–1532 (1995). doi:10.1002/jms.1190301102.

125. King GC. *Electron and ion optics.* In F Dunning and RG Hulet, editors, *Atomic, Molecular, and Optical Physics: Charged Particles*, volume 29, Part A of *Methods in Experimental Physics*, pp. 189 – 207. Academic Press (1995). doi:10.1016/S0076-695X(08)60656-0.

126. Kato M and Sekine T. *Spherical aberration correction of electrostatic lenses using spherical meshes.* J. Vac. Sci. Technol. A, **13**(4):2255–2260 (1995). doi:10.1116/1.579504.

127. Matsuda H, Daimon H, Kato M, and Kudo M. *Approach for simultaneous measurement of two-dimensional angular distribution of charged particles: Spherical aberration correction using an ellipsoidal mesh.* Phys. Rev. E, **71**:066503 (2005). doi:10.1103/PhysRevE.71.066503.

128. *BEHLKE FSWP 51-02 product sheet.* `http://www.behlke.com/pdf/fswp%2091-01_rs.pdf` (2012-11-27).

129. *DEI Scientific Instruments, PVM-4210.* `http://www.directedenergy.com/index.php?option=com_joomdoc&task=document.download&path=dei-scientific/datasheets/PVM-4210_Datasheet_RevB.pdf` (2014-05-27).

130. Jensen E, Bartynski RA, Hulbert SL, and Johnson ED. *Auger photoelectron coincidence spectroscopy using synchrotron radiation.* Rev. Sci. Instrum., **63**(5):3013–3026 (1992). doi:10.1063/1.1142602.

131. Bartynski RA. *Auger–photoelectron coincidence spectroscopy (APECS): Reviewing a growing field.* AIP Conf. Proc., **697**(1):111–118 (2003). doi:10.1063/1.1643686.

132. Viefhaus J, Snell G, Hentges R, Wiedenhöft M, Heiser F, Geßner O, and Becker U. *Interference effects between Auger and photoelectron studied by subnatural linewidth Auger-photoelectron coincidence spectroscopy.* Phys. Rev. Lett., **80**:1618–1621 (1998). doi:10.1103/PhysRevLett.80.1618.

133. Lablanquie P, Penent F, Hall RI, Kjeldsen H, Eland JHD, Muehleisen A, Pelicon P, Šmit Z, Žitnik M, and Koike F. *Coster-Kronig decay of the* Ar 2*s hole observed by Auger-threshold photoelectron coincidence spectroscopy.* Phys. Rev. Lett., **84**:47–50 (2000). doi:10.1103/PhysRevLett.84.47.

134. Lupulescu C, Arion T, Hergenhahn U, Ovsyannikov R, Förstel M, Gavrila G, and Eberhardt W. *iDEEAA: A novel, versatile apparatus for electron spectroscopy.* J. Electron Spectrosc. Relat. Phenom., **191**:104–111 (2013). doi:10.1016/j.elspec.2013.09.002.

135. Kugeler O, Marburger S, and Hergenhahn U. *Calculation and measurement of the time-of-flight spread in a hemispherical electron energy analyzer.* Rev. Sci. Instrum., **74**(9):3955–3961 (2003). doi:10.1063/1.1599060.

136. Ulrich V. *Untersuchung von Autoionisationsprozessen in kleinen Molekülen und Clustern mittels hochauflösender Elektronen-Koinzidenzspektroskopie.* Ph.D. thesis, Fakultät II – Mathematik und Naturwissenschaften der Technischen Universität Berlin (2007).

137. Ulrich V, Barth S, Joshi S, Lischke T, Bradshaw AM, and Hergenhahn U. *Separating the vibrationally resolved Auger decay channels for a CO core hole state.* Phys. Rev. Lett., **100**:143003 (2008). doi:10.1103/PhysRevLett.100.143003.

138. Loos E. *Design and Building of a Time-of-Flight Type Electron Spectrometer.* Department of Physical Sciences, University of Oulu, Finland (2006).

139. Bässler M, Ausmees A, Jurvansuu M, Feifel R, Forsell JO et al. *Beam line I411 at MAX II—performance and first results.* Nucl. Instrum. Methods Phys. Res. A, **469**(3):382–393 (2001). doi:10.1016/S0168-9002(01)00786-0.

140. Carroll T, Bozek J, Kukk E, Myrseth V, Sæthre L, Thomas T, and Wiesner K. *Xenon $N_{4,5}OO$ Auger spectrum—a useful calibration source.* J. Electron Spectrosc. Relat. Phenom., **125**(2):127–132 (2002).

141. Calicchia P, Lagomarsino S, Scarinci F, Martinelli C, and Formoso V. *A study on background subtraction in Auger and photoelectron time coincidence spectroscopy using third generation synchrotron radiation source.* Rev. Sci. Instrum., **70**(9):3529–3536 (1999). doi:10.1063/1.1149955.

142. Laksman J, Céolin D, Månsson EP, Sorensen SL, and Gisselbrecht M. *Development and characterization of a multiple-coincidence ion-momentum imaging spectrometer.* Rev. Sci. Instrum., **84**(12):123113 (2013). doi:10.1063/1.4853435.

143. Leemann SC, Andersson A, Eriksson M, Lindgren LJ, Wallén E, Bengtsson J, and Streun A. *Beam dynamics and expected performance of Sweden's new storage-ring light source: MAX IV.* Phys. Rev. ST Accel. Beams, **12**:120701 (2009). doi:10.1103/PhysRevSTAB.12.120701.

144. Leemann SC. *MAX-lab internal note 20120313: Updates to the MAX IV 1.5 GeV storage ring lattice.* `http://www.maxlab.lu.se/node/999/` (2012-03-13, revised 2012-06-11).

145. Leemann SC. *MAX-lab internal note 20121107: Updates to the MAX IV 3 GeV storage ring lattice.* `http://www.maxlab.lu.se/node/999/` (2012-11-07, revised 2014-01-29).

146. Leemann SC. *Interplay of Touschek scattering, intrabeam scattering, and rf cavities in ultralow-emittance storage rings.* Phys. Rev. ST Accel. Beams, **17**:050705 (2014). doi:10.1103/PhysRevSTAB.17.050705.

147. Sorensen SL, Olsson T, Stråhlman C, and Leemann SC. *Workshop on timing modes for low-emittance storage rings.* Synchrotron Radiation News, **28**(5):12–15 (2015). doi:10.1080/08940886.2015.1080062.

# COMMENTS ON THE PAPERS

I **A tandem time–of–flight spectrometer for negative–ion/positive–ion coincidence measurements with soft x-ray excitation**

This paper presents a spectrometer for mass-resolved negative–ion/positive–ion coincidence measurements of gaseous samples. First results include identification of several negative–ion/positive–ion and negative–ion/positive–ion/positive–ion coincidence channels following inner-shell photoexcitation of sulfur hexaflouride.

*I made the conceptual design of the instrument, performed the electrostatic simulations, oversaw the detailed design and production, applied for beamtime as principal investigator, led the commissioning at Elettra, performed most of the data analysis and wrote most of the paper.*

II **Negative–ion/positive–ion coincidence yields of core–excited water**

This paper presents scientific results acquired with the instrument presented in Paper **I**. The paper reports yields of mass–resolved negative ions and positive ions measured in coincidence after core–excitation of water molecules. Pathways leading to negative ion production are identified and assessed in relation to earlier studies of the fragmentation of the water molecule.

*I was the principal investigator of the project, participated in the experiment including setting up the equipment, performed the data analysis and wrote the paper.*

III **Non-radiative decay and fragmentation in water after O 1s ionization and O 1s $\rightarrow 4a_1$ excitation studied by electron-energy resolved electron-ion coincidences and ab initio calculations**

This paper reports a study on the fragmentation of water molecule by means of energy resolved Auger–electron/positive–ion coincidences after O 1s ionization and O 1s $\rightarrow 4a_1$ excitation, and quantum chemical calculations.

*I did initial studies for this project as part of my MSc Thesis in 2011, with AS as my supervisor. I participated in the experiments, performed the data analysis and participated in writing the manuscript.*

IV **Field ionization of high–Rydberg fragments produced after inner–shell photoexcitation and photoionization of the methane molecule**

This paper reports production of neutral high-Rydberg (HR) fragments from the methane molecule, studied with a novel instrument. Neutral fragments in HR states were ionized using a pulsed electric field and the resulting ions were mass-analyzed using an ion time-of-flight spectrometer. The origin of high-Rydberg fragments are discussed aided by quantum chemical calculations.

*I participated in the experiment including commissioning of the instrument, aided with some electrostatic simulations and commented on the manuscript.*

V **Preparing the MAX IV Storage Rings for Timing–based Experiments**

This paper discusses possibilities to do timing–based experiments at the MAX IV storage rings. Developments in both accelerator technology and beamline instrumentation are presented. The paper introduces some possible opportunities for MAX IV, considering the rings' unique timing properties and low emittance.

*TO and I contributed equally to the paper; TO with focus on accelerator techniques and I with focus on beamline instrumentation. Both participated in planning the paper, information gathering, simulations and wrote equal parts of the manuscript. I presented the paper at the Synchrotron Radiation Instrumentation conference.*

VI **Using Detector Gating to Operate an ArTOF Time-of-Flight Electron Spectrometer in Hybrid Mode at Storage Ring SR-Facilities**
This paper presents a method for detector gating of an angle–resolved time–of–flight electron spectrometer.
*I participated in commissioning experiments at BESSY, made an initial design for the gate circuit, did most of the data analysis and wrote parts of the manuscript.*

VII **Angle-resolved time-of-fight spectroscopy applied to multi-bunch operation at MAX-lab: a design study**
This paper presents a design for a gating scheme of an angle–resolved time–of–flight electron spectrometer. Design, materials and electronic equipment are discussed.
*I made the design, performed the simulations, wrote the manuscript and presented it at the Synchrotron Radiation Instrumentation conference. After the publication of this paper, I performed yet unpublished experiments with the proposed gating scheme.*

# Papers

# PAPER I

**A tandem time–of–flight spectrometer for negative–ion/positive–ion coincidence measurements with soft x-ray excitation**

Christian Stråhlman, Rami Sankari, Antti Kivimäki, Robert Richter, Marcello Coreno, Ralf Nyholm.

*Review of Scientific Instruments* **87**, 013109 (2016).

REVIEW OF SCIENTIFIC INSTRUMENTS 87, 013109 (2016)

# A tandem time–of–flight spectrometer for negative–ion/positive–ion coincidence measurements with soft x-ray excitation

Christian Stråhlman,[1,a)] Rami Sankari,[1] Antti Kivimäki,[2] Robert Richter,[3] Marcello Coreno,[4] and Ralf Nyholm[1]
[1]*MAX IV Laboratory, Lund University, P.O. Box 118, 22100 Lund, Sweden*
[2]*Consiglio Nazionale delle Ricerche—Istituto Officina dei Materiali, Laboratorio TASC, 34149 Trieste, Italy*
[3]*Elettra–Sincrotrone Trieste, Area Science Park, 34149 Trieste, Italy*
[4]*Consiglio Nazionale delle Ricerche—Istituto di Struttura della Materia, 34149 Trieste, Italy*

(Received 23 October 2015; accepted 11 January 2016; published online 27 January 2016)

We present a newly constructed spectrometer for negative–ion/positive–ion coincidence spectroscopy of gaseous samples. The instrument consists of two time–of–flight ion spectrometers and a magnetic momentum filter for deflection of electrons. The instrument can measure double and triple coincidences between mass–resolved negative and positive ions with high detection efficiency. First results include identification of several negative–ion/positive–ion coincidence channels following inner-shell photoexcitation of sulfur hexafluoride ($SF_6$). © *2016 AIP Publishing LLC*. [http://dx.doi.org/10.1063/1.4940425]

## I. INTRODUCTION

Studying photoinduced dissociation of molecules is of fundamental importance to chemical physics and the understanding of chemical bonds. Photoexcitation of molecules can induce a multitude of chemical processes, some of which lead to the fragmentation of the molecule. Under some circumstances, photoinduced fragmentation produces negative ions together with positive ions. Detecting and analyzing negative ions are not qualitatively different from positive ions; the same instruments can often be employed for both. Quadrupole mass filters,[1,2] time-of-flight (TOF) based instruments[3,4] and velocity map imaging (VMI)[5] have been used to measure negative-ion yields. The very same methods have been employed also in a few studies of negative and positive ions in coincidence, with TOF[6–9] and VMI[10–12] as the dominating techniques. Both approaches separate positive and negative particles by an electric field and accelerate them towards the respective detectors.

Negative–ion production from photoexcitation has received much less attention than that of positive ions. This is natural since negative–ion yields (NIY) are generally much smaller than positive–ion yields (PIY). This has to be compensated for by an increase of the transmission of the instrument and by increasing the intensity of the excitation, the latter being achievable with modern synchrotron radiation facilities. In addition, the instrument must effectively suppress the unwanted detection of electrons, which in an electrostatic instrument will follow the same paths as negative ions. An early version of an electron–deflecting filter by Schermann *et al.*[13] consisted of a small dipole electromagnet in a $\mu$-metal casing. Since electrons are very light particles with small momenta, they are quite easy to deflect. TOF–based negative–ion spectrometers have used similar solutions either with permanent magnets or electromagnets.[8–10]

Negative–ion/positive–ion coincidences (NIPICO) have mostly been studied in small molecules with VUV and/or visible light using both laboratory and accelerator based sources.[6–8,10–12] NIPICO investigations have rarely exploited x-ray radiation; we are only aware of one study. Rühl and Flesch[9] observed double and triple coincidences at the C 1$s$ $\rightarrow \pi^*$ excitation in the $CO_2$ molecule using an instrument with two identical TOF spectrometers. Extending the analysis to multiple coincidences between the fragments (NIPIPICO: negative–ion/positive–ion/positive–ion coincidence) allowed them to study the kinetic energy release and chart the complete fragmentation path of the molecule. Their instrument could distinguish between different positive ions in coincidence with negative ions; however, the $CO_2$ molecule only produce one negative ion species.

We have designed a new instrument for detecting mass–resolved negative ions in coincidence with one or several mass–resolved positive ions. The instrument can identify NIPICO and NIPIPICO channels for samples where several species of negative ions are produced. It applies the TOF–based coincidence technique, with two spectrometers working in tandem, and a momentum filter for negative particles. The negative–ion spectrometer is specifically optimised for high transmission, which increases detection efficiency for coincidences. While the main goal of current experiments is the study of core–excited states in small molecules induced by soft x-ray excitation, the instrument could equally well be used for studies of valence–excited states.

This paper describes the instrument and discusses our design considerations. Acquisition modes for coincidence and calibration measurements are presented. We demonstrate detection and assignment of double and triple coincidences with high reliability and efficiency. In particular, the continuous acquisition of detector signals, with the instrument working with a constant extraction field, increases the efficiency of the instrumental setup. The performance of the instrument is demonstrated with a study on sulfur hexafluoride ($SF_6$),

a)Electronic mail: Christian.Strahlman@maxlab.lu.se

 

which is known to produce negative ions at the S 2p and F 1s edges.[14,15]

## II. INSTRUMENT DESIGN

The setup consists of two time–of–flight ion spectrometers mounted facing each other. Both spectrometers operate under Wiley–McLaren focusing conditions[17] and share a 15 mm wide interaction region. The synchrotron light beam passes through the center of the interaction region where it crosses an effusive gas jet, which is let into the vacuum chamber through a gas needle perpendicular to the spectrometers and the light beam. An electric field in the extraction region separates positive and negative particles and accelerates them into the two spectrometers. The spectrometers are mounted at 54.7° (so called magic angle) relative to the polarization vector of the horizontally polarized light beam.

The spectrometer used for positive–ion detection was originally developed for a photoelectron/positive–ion coincidence (PEPICO) setup used at the Elettra storage ring and has been previously described in Ref. 18. The instrument consists of a 319 mm long and 40 mm wide stainless steel drift tube, preceded by two mesh holders, which create a 5 mm wide acceleration region and a 15 mm wide interaction region. Ions are detected by a Z-stacked triple MCP detector at the end of the drift tube. The tube and mesh holders are mounted on four steel rods, electrically isolated by PEEK spacers.

The negative–ion spectrometer was specifically designed to operate together with the existing positive–ion spectrometer without any changes to the latter. A second requirement was that an existing chamber be used, which put limits on the width and length of the instrument. In addition, we wanted to be able to use the new spectrometer as a stand–alone instrument, or in a PEPICO setup. To accommodate these needs, we have constructed the spectrometer with two interchangeable front parts, with and without an interaction region. In the NIPICO version, the original extraction region of the positive–ion spectrometer is used. The drift tube of the negative–ion spectrometer is docked to the grounded rods using four PEEK holders (see Fig. 1). The 5 mm long region created between the outer mesh of the interaction region and the outer drift tube mesh on the negative–ion spectrometer thus becomes the acceleration region for the negative–ion spectrometer. In the non-coincident version of the instrument, the PEEK spacers are interchanged with a complete extraction region including two holders with gold meshes (see Fig. 2).

As noted in Sec. I, the extraction of negative particles causes both negative ions and electrons to enter the negative–ion spectrometer. Since the number of electrons greatly outweighs that of the negative ions, they have to be deflected as not to saturate the detector and to improve the signal–to–noise ratio in coincidence experiments. This is most easily performed with a weak magnetic field in the drift tube. Simulations show that a magnetic field amounting to 15 G can deflect electrons with kinetic energies up to 3000 eV (electrons' high kinetic energies result from the acceleration into the drift tube), while the impact on flight paths, and associated flight times even of the lightest ions is negligible. We decided to generate the magnetic field from outside of the vacuum by mounting two small neodymium magnets on an adjustable holder on the vacuum chamber.

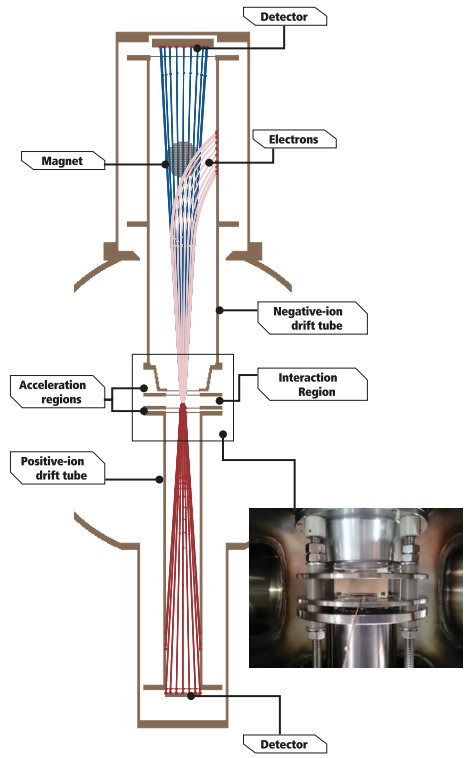


FIG. 1. Schematic drawing of the instrument setup with the negative–ion (top) and positive–ion (bottom) spectrometer. Negative ions, positive ions, and electrons are created in the interaction region and accelerated into the spectrometers. The inset depicts the interaction and acceleration regions (without needle) for the mounted spectrometer. Electrons are deflected in the negative–ion spectrometer by a weak magnetic field, provided by two small magnets outside vacuum (see also Fig. 2). The simulation shows trajectories of $H^-$ ions (blue), $H^+$ ions (red) and electrons, each with 10 eV initial kinetic energy. The 15 G magnetic field only marginally deflects even the lightest ions. The positive–ion spectrometer is narrower and collects fast ion less efficiently. Simulations were performed with the SIMION software.[16]

The drift tube was made from an aluminum tube perforated by many small holes, 4 mm in diameter. The rationale behind this design is to minimize possible effects caused by secondary electrons created when deflected electrons with energies in the keV–range hit the inside of the drift tube. By using a perforated tube, the majority of electrons leaves the tube and becomes decelerated by the potential difference between the drift tube and the grounded vacuum chamber wall.

Since NIYs are small, a high transmission in the instrument is required. Light ions, particularly hydrogen ions ($H^-$), often escape detection in narrow TOF instruments since they tend to have high kinetic energies. A wider drift tube and larger detector area give a better collection efficiency even for

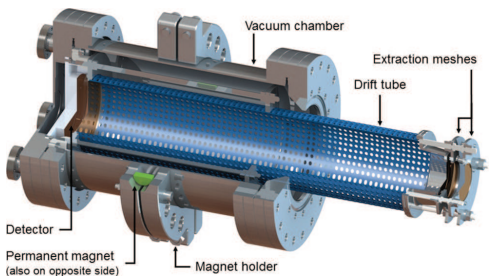


FIG. 2. Drawing of the negative–ion spectrometer in its stand-alone configuration with a separate interaction region. The magnetic field is provided by two external permanent magnets fixed by the movable magnet holder.

light ions. The detector for the negative–ion spectrometer is a commercial Hamamatsu double MCP with a circular, 77 mm in diameter, active area, and a single anode readout. Response time is 2 ns as stated by the manufacturer. Due to the detector design, the potential on the anode could not exceed +2800 V, referenced to ground potential. To achieve a suitable gain over the MCP stack, while avoiding a deceleration field between the MCP front and the drift tube end, the MCP front potential was limited to only +900 V. This defined the upper limit for the negative–ion spectrometer drift tube potential. In the experiments presented in this paper, the following potentials were used: extractor meshes ±92 V, negative–ion drift tube +854 V, positive–ion drift tube −740 V. In present settings, simulations performed with the SIMION software[16] showed that the negative–ion spectrometer accepts $H^-$ ions with initial velocities perpendicular to the spectrometer axis corresponding to kinetic energies up to 5 eV. However, in the present coincidence setup, the total transmission is limited by the narrower positive–ion spectrometer.

The output pulses from the detectors were amplified and, after passing through a discriminator, read by a time-to-digital converter (TDC, model AM-GPX, manufactured by ACAM Messelectronic) with 80 ps time resolution. This system has been described in Ref. 18. The intensity of the light reaching the sample was monitored using a photodiode at the downstream exit of the chamber.

## III. EXPERIMENTAL

The experiments were performed at the Gas Phase Photoemission beamline of the Elettra synchrotron radiation laboratory (Trieste, Italy). The beamline has been described in detail before.[19,20] Briefly, it uses an undulator as a light source and a spherical grating monochromator for the selection of the photon energy. The photon energy range of the beamline is 13.5–900 eV. High resolving power ($>10^4$) can be achieved at most energies thanks to five interchangeable gratings.

The light beam was centered in the interaction region by moving the frame of the spectrometer chamber. The effusive gas jet is let into the chamber through a gas needle controlled by a leak valve. The position of the needle was adjusted so that the photon beam crossed the gas jet in the interaction region. When the gas was introduced to the chamber, the pressure increased from the $3 \times 10^{-8}$ mbar base pressure to $5 \times 10^{-7}$ mbar, but it was estimated to be 10–50 times higher in the interaction region.

Having the permanent magnets mounted outside vacuum allowed us to quickly remove the magnetic field for testing the spectrometer performance. The position of the permanent magnets was optimized in several steps. Electrostatic simulations showed that there is a non-negligible probability that deflected electrons are focused back into the perforated drift tube and subsequently hit the detector. We indeed observed that some electrons were recorded in all acquisitions even after optimization. After optimizing the magnet positions in order to minimize the electron signal, we switched the polarity of the negative–ion spectrometer to measure positive ions instead. We could see that the measured flight times for ions matched simulations. We found that we had the most efficient reduction of electron signal when the magnets were positioned very close to the interaction region.

## IV. PERFORMANCE AND FIRST RESULTS

To demonstrate the capabilities of the spectrometer and the NIPICO and NIPIPICO analysis, we have performed measurements of the $SF_6$ molecule. $SF_6$ is a well-known sample, and its photoexcitation properties have been investigated in several studies. NIYs and PIYs from photo-exited $SF_6$ have been measured in the inner-valence,[14] S 2p,[14,15] and F 1s regions.[15] The S 2p excitation spectrum of $SF_6$ displays several strong absorption resonances. The $6a_{1g}$ resonance lies below the 2p ionization threshold, while two shape resonances ($2t_{2g}$ and $4e_g$) are present above the ionization potential.[21] Several negative (and positive) ion channels have been identified. The molecule is therefore well suited for instrument testing.

The instrument can be operated in two different acquisition modes, where the first mode is aimed at flight time calibration and acquisition of mass resolved PIY and NIY, while the second is aimed at NIPICO and NIPIPICO analysis.

Calibration is performed in the pulsed extraction mode. An extraction field is produced by a pulsed high-voltage supply. We used an instrument from Directed Energy, Inc., model PVM 4210, controlled by a pulse generator (Stanford Research DG535) to produce two identical square pulses of opposite polarity with 92 V amplitude, 22 $\mu$s length, and 10 kHz repetition rate. The amplitude is determined by the Wiley–McLaren space focusing conditions.[17] The pulse trigger signal is used as the start trigger for the TOF measurement. This mode produces positive and negative TOF spectra independently and can therefore be used to measure the flight times of individual fragments. We measured positive–ion mass spectra with both spectrometers. The positive–ion spectrum measured by the negative–ion spectrometer was acquired by changing the polarity of all electrostatic potentials. The flight times of positive ions are identical to those of negative ions for opposite polarities. All measured flight times have an excellent match with SIMION simulations.

While it is in principle possible to deduce NIPICO events from the pulsed mode, in practice, the efficiency of the instrument is too low for this to be a feasible method. Because

the pulse is not correlated to the ionization process, many ions, even with low kinetic energies, have sufficient time to escape the interaction region before the pulse is applied. The pulsed operation therefore favors the detection of slow and heavy ions. In addition, due to the movements of the ions, the effective source size seen by the spectrometer spans the whole 15 mm wide interaction region. This causes a significant broadening of mass peaks (several 100 ns) compared to a PEPICO measurement where the ion is extracted almost immediately following its creation. This is particularly true with the present low-voltage settings.

The efficiency of the instrument is significantly increased by continuous extraction of positive and negative ions. Static electric fields are used to extract ions from the interaction region. Flight–time differences of two fragments can be constructed from the hits of ions on the two detectors. Combined with flight times measured in the pulsed mode and aided by simulations of flight times for all possible negative and positive ionic fragments, each flight–time difference can be assigned to a coincidence between a specific negative ion and a specific positive ion.

Signals can be recorded in two ways. In the first analysis scheme (*negative ion trigger*), a detection of a negative ion provides a start signal for the timing electronics, while a subsequent detection of a positive ion gives a stop. The positive–ion signal is delayed electronically to ensure that it arrives after the corresponding start signal. (Typically the delay should be slightly larger than the difference between expected flight times of the slowest negative ion and the fastest positive ion.) While this scheme is the most efficient way to record coincidences between two fragments (NIPICO) the detection of three or more coincident fragments is inhibited. The second analysis scheme (*continuous trigger*) records all hits at both detectors continuously. The coincidence events are established afterwards in the computer analysis. In principle, coincidences between several negative and several positive fragments can be recorded. In our analysis, we have restricted ourselves to coincidences between one negative and (up to) three positive fragments.

NIPICO spectra were measured with negative ion triggering at the main resonances in the S 2p region. Each acquisition lasted 120 min and the positive ions were recorded with a 8000 ns delay. Fig. 3 shows complete TOF spectra acquired at four photon energies. The spectra display a multitude of peaks and features among which only few are true NIPICO events. Positions for the main coincidence channels are indicated. These peaks have been identified to be true NIPICO peaks by comparing with spectra where the drift tube potential on the negative–ion spectrometer was increased by 45 V. The measured TOFs of NIPICO peaks are expected to shift towards longer times, while PEPICO peaks should not display any significant shift. Only the indicated NIPICO peaks, corresponding to $SF^-/F^+$, $S^-/F^+$, $F^-/F^+$, and $F^-/S^+$ coincidences, did shift. The $S^-/F^+$ and $F^-/F^+$ peaks show a pronounced splitting due to kinetic energy release in the fragmentation. Towards longer flight times, several PEPICO channels are present. These arise from electrons which are not completely removed by the deflection in the negative–ion spectrometer. Their expected positions can be simulated and can serve as calibration peaks since all pairs of PEPICO and NIPICO peaks with identical positive ion participants should be equally distanced from each other.

The sharp peak at $t = 0$ marks events where the two detectors recorded hits almost simultaneously. The probable explanation for these events is spurious crosstalk between the two detectors, possibly caused by the power supply. Due to hardware errors in the TDC card, additional sharp features can be seen in the spectra—both positive peaks (e.g., the large peak at −1100 ns and several smaller peaks below −4000 ns) and negative peaks (at −3000 ns and repeated every 5000 ns). These are not related to any true process, as verified by comparing spectra recorded with slightly increased drift tube potentials of the two spectrometers, one at a time. Only true NIPICO and PEPICO peaks were observed to shift their

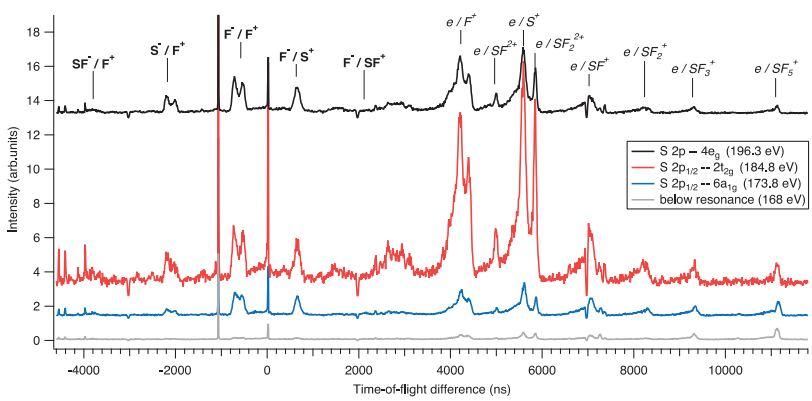


FIG. 3. Complete NIPICO spectra for three resonances in the S 2p region of $SF_6$ (black, red, and blue), together with a reference spectrum below resonances (gray). Each spectrum was acquired for 120 min. The intensity has been normalized to the beam intensity, as measured by the photodiode. Five NIPICO channels have been marked. All peaks in the 3500–12 000 ns region belong to the PEPICO spectrum created from residual electrons in the negative–ion spectrometer. The origin of other false peaks is discussed in the text.

positions in accordance with calculated flight times for the increased potentials. The two broad features at 1500 ns and 2700 ns cannot be assigned to any PEPICO channel, but they appear to shift when changing the drift tube potential of the positive–ion spectrometer. It is plausible that these features arise from the detection of secondary electrons in coincidence with positive ions. Their positions match coincidences triggered from electrons that are created when positive ions hit meshes in the positive–ion spectrometer during flight.

Core–excited states predominantly decay by emission of Auger electrons. Thus, a fragmentation process including one negative ion is likely to produce several positive ions. Fig. 4 shows the results from a continuous trigger measurement at the F 1s $\rightarrow 6t_{1u}$ excitation ($h\nu$ = 693.5 eV). From the map we can identify four triple–coincidence channels involving one negative and two positive fragments. It should be noted that the $F^-/SF^+/F^+$ channel is clearly visible in the NIPIPICO map, while the $F^-/SF^+$ channel hardly shows up in the NIPICO spectrum. This is indeed expected since the detection of a fast $F^+$ fragment in the negative ion trigger scheme inhibits the subsequent detection of a slower $SF^+$ fragment. While our instrument is capable of measuring even higher order coincidence channels, such as NIPIPIPICO, no such events could be identified in the current dataset.

Some general observations can be made regarding the acquisition modes. In the continuous extraction mode, the identity of the complete negative–ion/positive–ion pairs is determined by the flight–time difference of the two fragments. In simple molecules with few possible fragments this is straightforward since the possible combinations of positive and negative ions are few. In more complicated molecules, such as $SF_6$, there are more combinations, and also an increasing risk for a temporal overlap between several pairs. In addition, since electron counts cannot be completely avoided, there is also a risk of a temporal overlap between electron/positive–ion and negative–ion/positive–ion coincidences. To avoid temporal overlaps between these processes, we have used simulations to adapt the flight times of all possible ion and electron combinations in order to find a combination of voltages that produces no overlaps. In the case of $SF_6$, only pairs of the lightest negative ions in coincidence with the heaviest positive ions overlap in part with electron/medium-heavy–positive–ion coincidences. For a definite measurement of these channels, pulsed mode coincidence measurements has to be performed. As the expected yield of these coincidences is very low, we have not performed such time–consuming measurements.

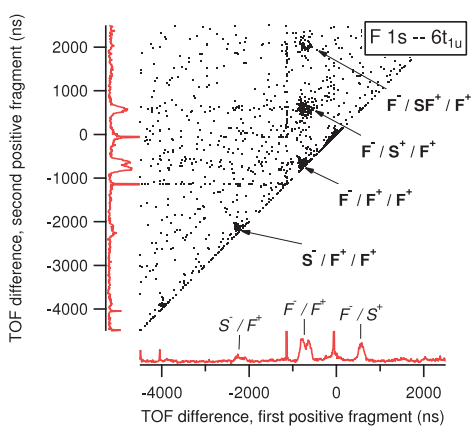


FIG. 4. NIPIPICO map measured at the F 1s $\rightarrow 6t_{1u}$ excitation ($h\nu$ = 693.5 eV) of $SF_6$. The map was acquired during 60 min. The bottom axis displays the time–of–flight difference between the first positive fragment and the negative fragment (as in Fig. 3), while the left axis shows the time-of-flight difference between the second positive fragment and the (same) negative fragment. The map thus shows the triple–coincidence between one negative and two positive fragments. Four triple–coincidence channels can be identified in this map. The increased yield at $t_1 = 0/t_2 = 0$ can be attributed to spurious crosstalk between detectors (see text).

## V. DISCUSSION

In this section, we briefly discuss scientific results that can be extracted from the presented data. While a complete analysis is beyond the scope of this paper, some initial results are outlined in order to illustrate the capabilities of the technique. While new insights into the negative ion formation from $SF_6$ can be extracted from the NIPICO data, a more comprehensive analysis of the dissociation pathways would greatly benefit from complete NIPIPICO yields. Additional such data at the S 2p edge will be collected in subsequent experiments.

Our NIPICO measurements (Fig. 3) show three clear coincidence channels, $S^-/F^+$, $F^-/F^+$, and $F^-/S^+$, at all three resonances. Their relative intensities can be compared to the valence–subtracted photoionization cross sections at these resonances. We estimate from the data of Ref. 22 that ionization at the S $2p_{1/2} \rightarrow 2t_{2g}$ shape resonance occurs with ~3.5 times higher probability than at the S $2p_{1/2} \rightarrow 6a_{1g}$ excitation and with ~2.3 times higher probability than at S $2p \rightarrow 4e_g$ shape resonance. When compared to ionization cross sections, we observe higher relative yields of $F^-/F^+$ and $F^-/S^+$ coincidences at the $6a_{1g}$ excitation than at the $2t_{2g}$ shape resonance. The $2t_{2g}$ shape resonance represents a temporary trapping of the S $2p$ photoelectron by a barrier in the molecular potential,[23] after which it is considered to decay so that the trapped electron tunnels into the continuum. The result is a S $2p$ ionized state, which typically decays via Auger transitions to doubly charged final states. Instead, at the S $2p_{1/2} \rightarrow 6a_{1g}$ excitation, the core-excited state is neutral and the final states after decay via electron emission (resonant Auger decay) are mostly singly ionized valence–excited states. Our coincidence spectra therefore show that the production of $F^-/F^+$ and $F^-/S^+$ ion pairs is more likely after core excitation than core ionization. The trend is understandable, since negative ions could obviously be released more easily if dissociating valence states after (resonant) Auger decay are less positively charged.

We also observe that all the negative-ion/positive-ion coincidence peaks are more intense at the $4e_g$ shape resonance than at the S $2p_{1/2} \rightarrow 2t_{2g}$ shape resonance, when normalized to the photoionization cross section. This can be explained by the multielectron character of the $4e_g$ shape resonance. Ferrett *et al.*[23] observed that a shake-up satellite of the S $2p$ photoelectron line is hugely enhanced at the $4e_g$ shape

resonance, gaining an intensity of even 30% of those of the S $2p$ main lines. The electron configuration of the satellite is of type S $2p^{-1}val^{-1}virt^{1}$, where $val$ is a valence orbital and $virt$ is an orbital that is unoccupied in the molecular ground state. When these core hole states decay via Auger transitions, they produce mostly excited states of the doubly charged parent ion, as the electron in the $virt$ orbital more likely acts as a spectator than participates in the decay. It is not yet known whether the presence of such an electron in the final states increases the production of negative ions or not. However, the S $2p$ shake-up states may also decay with small probability via S $2p$ fluorescence emission. This decay channel populates excited final states of the singly ionized molecule, similarly to resonant Auger decay at the S $2p_{1/2} \rightarrow 6a_{1g}$ excitation below the S $2p$ ionization potential. Radiative decay channel of the shake-up states is therefore expected to contribute to the production of negative ions. Also core-valence double excitations (to S $2p^{-1}val^{-1}virt^{1}_{1}virt^{1}_{2}$ core-excited states) may occur at the $4e_g$ shape resonance.[23] Their resonant Auger decay would also lead to excited states of the singly ionized molecular ion, and after dissociation reactions to negative ions. In summary, among multielectron transitions, both the S $2p$ shake-up ionization and core-valence double excitations can increase the production of negative ions.

While it has been suggested previously that NIY is a sensitive tool to assign above–threshold resonances in diatomic and triatomic molecules,[24] it is not the case for a larger molecule such as $SF_6$.[15] It has been argued that a larger molecular system is able to dissipate many positive charges over several smaller fragments. Indeed, the dominance of negative and positive F, S, and SF ions generally in the NIPICO and NIPIPICO spectra suggests that production of negative ions from core-excited $SF_6$ is a process where the molecule breaks into many small fragments. So far, none of our measured resonances at the S 2p or F 1s edge have displayed a coincidence channel involving any ionic fragment heavier than $SF^{\pm}$. NIY from valence excitation,[2] in contrast, has a significant contribution from the heavy $SF_5^-$ fragment as well as the lighter $F_2^-$. This observation further strengthens the rationale for a complete NIPIPICO study to unfold the dissociation pathways in core-excited $SF_6$, including the contribution of radiative decay in negative ion production.

## VI. CONCLUSIONS AND OUTLOOK

We have constructed and commissioned a new instrument to measure negative–ion/positive–ion coincidences from gas phase molecules. The instrument is able to measure coincidences between one negative and several positive fragments originating from a single fragmentation event. The instrument builds on well understood TOF techniques together with magnetic deflection of unwanted electrons. The NIPICO and NIPIPICO technique provides a tool to further increase the understanding of the molecular fragmentation process, particularly with the new abilities to study negative ion production.

We foresee some changes that will improve the performance of the instrument. Rebuilding the detector holder would allow us to run the negative–ion spectrometer in a larger range of acceleration potentials, thus avoiding temporal overlaps between coincidence channels. An increased MCP gain can also increase the detection efficiency for heavier ions. Increasing the drift tube potential also increases temporal resolution and transmission for high-energy ions. Second, the magnetic deflection needs to be improved in order to provide a more localized magnetic field in the drift tube. This is essential to properly steer the deflected electrons and further reduce electron counts on the negative–ion detector, thus increasing the purity of the spectra. A possible future development of the instrument to include position sensitive detectors for both negative and positive ions would increase the amount of information rendered from the experiment, especially to chart in more detail the dissociation dynamics in negative–ion producing channels. Further scientific studies on small organic molecules are planned for the coming year.

## ACKNOWLEDGMENTS

The authors acknowledge E. S. El Afifi and the staff at the workshop at MAX IV Laboratory for their assistance with the design and production of the negative-ion spectrometer. We thank D. Benedetti (CNR–IOM) for assistance in designing the support for the TOF spectrometers as well as M. Barnaba and G. Bortoletto (Elettra–Sincrotrone Trieste) for the construction of new pieces for the support. J. Winqvist has assisted with graphical design of figures in this article. We acknowledge Elettra–Sincrotrone for providing beamtime (Proposal No. 20145053) and the staff at Elettra for their assistance during commissioning. The research leading to these results has received funding from the European Community's Seventh Framework Programme (FP7/2007-2013) under Grant Agreement No. 312284.

[1]K. Mitsuke, S. Suzuki, T. Imamura, and I. Koyano, J. Chem. Phys. **92**, 6556 (1990).
[2]M. J. Simpson and R. P. Tuckett, Int. Rev. Phys. Chem. **30**, 197 (2011).
[3]Q. Feng, S.-X. Tian, Y.-J. Zhao, F.-Y. Liu, X.-B. Shan, and L.-S. Sheng, Chin. Phys. Lett. **26**, 053402 (2009).
[4]E. Rühl and H.-W. Jochims, Z. Phys. Chem. **195**, 137 (1996).
[5]Y. Hikosaka and E. Shigemasa, J. Electron Spectrosc. Relat. Phenom. **148**, 5 (2005).
[6]K. Mitsuke, H. Yoshida, and H. Hattori, Z. Phys. D **27**, 267 (1993).
[7]H. Yoshida and K. Mitsuke, J. Electron Spectrosc. Relat. Phenom. **79**, 487 (1996).
[8]H. Yoshida and K. Mitsuke, J. Chem. Phys. **100**, 8817 (1994).
[9]E. Rühl and R. Flesch, J. Chem. Phys. **121**, 5322 (2004).
[10]Y. Hikosaka and J. H. D. Eland, Rapid Commun. Mass Spectrom. **14**, 2305 (2000).
[11]S. Marggi Poullain, K. Veyrinas, P. Billaud, M. Lebech, Y. J. Picard, R. R. Lucchese, and D. Dowek, J. Chem. Phys. **139**, 044311 (2013).
[12]C. Elkharrat, Y. J. Picard, P. Billaud, C. Cornaggia, D. Garzella, M. Perdrix, J. C. Houver, R. R. Lucchese, and D. Dowek, J. Phys. Chem. A **114**, 9902 (2010).
[13]C. Schermann, I. Cadez, P. Delon, M. Tronc, and R. I. Hall, J. Phys. E: Sci. Instrum. **11**, 746 (1978).
[14]S. W. J. Scully, R. A. Mackie, R. Browning, K. F. Dunn, and C. J. Latimer, J. Phys. B: At., Mol. Opt. Phys. **35**, 2703 (2002).
[15]M. N. Piancastelli, W. C. Stolte, R. Guillemin, A. Wolska, S.-W. Yu, M. M. Sant'Anna, and D. W. Lindle, J. Chem. Phys. **122**, 094312 (2005).
[16]See http://simion.com/ for SIMION.
[17]W. C. Wiley and I. H. McLaren, Rev. Sci. Instrum. **26**, 1150 (1955).
[18]O. Plekan, M. Coreno, V. Feyer, A. Moise, R. Richter, M. de Simone, R. Sankari, and K. C. Prince, Phys. Scr. **78**, 058105 (2008).

[19]R. Blyth, R. Delaunay, M. Zitnik, J. Krempasky, R. Krempaska, J. Slezak, K. Prince, R. Richter, M. Vondracek, R. Camilloni, L. Avaldi, M. Coreno, G. Stefani, C. Furlani, M. de Simone, S. Stranges, and M.-Y. Adam, J. Electron Spectrosc. Relat. Phenom. **101-103**, 959 (1999).
[20]K. C. Prince, R. R. Blyth, R. Delaunay, M. Zitnik, J. Krempasky, J. Slezak, R. Camilloni, L. Avaldi, M. Coreno, G. Stefani, C. Furlani, M. de Simone, and S. Stranges, J. Synchrotron Radiat. **5**, 565 (1998).
[21]E. Hudson, D. A. Shirley, M. Domke, G. Remmers, A. Puschmann, T. Mandel, C. Xue, and G. Kaindl, Phys. Rev. A **47**, 361 (1993).
[22]M. Stener, P. Bolognesi, M. Coreno, P. O'Keeffe, V. Feyer, G. Fronzoni, P. Decleva, L. Avaldi, and A. Kivimäki, J. Chem. Phys. **134**, 174311 (2011).
[23]T. A. Ferrett, D. W. Lindle, P. A. Heimann, M. N. Piancastelli, P. H. Kobrin, H. G. Kerkhoff, U. Becker, W. D. Brewer, and D. A. Shirley, J. Chem. Phys. **89**, 4726 (1988).
[24]W. C. Stolte, D. L. Hansen, M. N. Piancastelli, I. Dominguez Lopez, A. Rizvi, O. Hemmers, H. Wang, A. S. Schlachter, M. S. Lubell, and D. W. Lindle, Phys. Rev. Lett. **86**, 4504 (2001).

# Paper II

**Negative–ion/positive–ion coincidence yields of core–excited water**

Christian Stråhlman, Antti Kivimäki, Robert Richter, Rami Sankari.
*manuscript*, in preparation.

# PAPER III

**Non-radiative decay and fragmentation in water after O 1s ionization and O 1s $\rightarrow 4a_1$ excitation studied by electron-energy resolved electron-ion coincidences and ab initio calculations**

Anna Sankari, Christian Stråhlman, J. Antti Kettunen, Rami Sankari, Leena Partanen, Joakim Laksman, Ignacio Fernández Galván, Roland Lindh, Per–Åke Malmqvist, Stacey L. Sörensen.

*manuscript*, in preparation.

# PAPER IV

**Field ionization of high–Rydberg fragments produced after inner–shell photoexcitation and photoionization of the methane molecule**

Antti Kivimäki, Anna Sankari, J. Antti Kettunen, Christian Stråhlman, Jesús Álvarez Ruiz, Robert Richter.

*The Journal of Chemical Physics* **143**, 114305 (2015).

THE JOURNAL OF CHEMICAL PHYSICS **143**, 114305 (2015)

# Field ionization of high-Rydberg fragments produced after inner-shell photoexcitation and photoionization of the methane molecule

A. Kivimäki,[1,a)] A. Sankari,[2] J. A. Kettunen,[3] C. Stråhlman,[4] J. Álvarez Ruiz,[5] and R. Richter[6]

[1]*Consiglio Nazionale delle Ricerche–Istituto Officina dei Materiali, Laboratorio TASC, 34149 Trieste, Italy*
[2]*Department of Physics, Lund University, P.O. Box 118, 22100 Lund, Sweden*
[3]*Department of Physics, University of Oulu, P.O. Box 3000, 90014 Oulu, Finland*
[4]*MAX IV Laboratory, Lund University, P.O. Box 118, 22100 Lund, Sweden*
[5]*Colegio Los Naranjos, Fuenlabrada, 28941 Madrid, Spain*
[6]*Elettra-Sincrotrone Trieste, Area Science Park Basovizza, 34149 Trieste, Italy*

(Received 9 June 2015; accepted 3 September 2015; published online 17 September 2015)

We have studied the production of neutral high-Rydberg (HR) fragments from the $CH_4$ molecule at the C 1s → 3p excitation and at the C 1s ionization threshold. Neutral fragments in HR states were ionized using a pulsed electric field and the resulting ions were mass-analyzed using an ion time-of-flight spectrometer. The atomic fragments C(HR) and H(HR) dominated the spectra, but molecular fragments $CH_x$(HR), x = 1-3, and $H_2$(HR) were also observed. The production of HR fragments is attributed to dissociation of $CH_4^+$ and $CH_4^{2+}$ ions in HR states. Just above the C 1s ionization threshold, such molecular ionic states are created when the C 1s photoelectron is recaptured after single or double Auger decay. Similar HR states may be reached directly following resonant Auger decay at the C 1s → 3p resonance. The energies and geometries of the parent and fragment ions have been calculated in order to gain insight into relevant dissociation pathways. © *2015 AIP Publishing LLC.* [http://dx.doi.org/10.1063/1.4931105]

## I. INTRODUCTION

A small molecule like $CH_4$ usually fragments if one of its inner-shell (or core) electrons is promoted to an unoccupied molecular or Rydberg orbital or is completely removed from the molecule. This is because electronic states with an inner-shell hole are highly excited, and typically decay through Auger transitions, where one valence electron fills the core hole and another valence electron is emitted. Resulting electronic states with two holes in valence orbitals are unstable in most molecules; for instance, stable or metastable $CH_4^{2+}$ cations have not been observed.[1] The energy needed to induce inner-shell electron transitions can be delivered by charged particles such as electrons and fast ions or by soft x-ray photons. Since in an x-ray photoabsorption process a photon loses all its energy to the molecule, this excitation method allows one to prepare core-excited molecules in well-defined electronic states and to study their subsequent fragmentation in more detail.

The electron configuration of the methane molecule in the ground state is $1a_1^2\,2a_1^2\,1t_2^6$, where the $1a_1$ orbital derives from the atomic C 1s orbital. Fragmentation of methane has been the subject of numerous studies in both the valence and core-level regions.[2] The Auger spectrum of methane measured just above the C 1s ionization potential (IP) shows three broad features which have been attributed to the $2a_1^{-2}$, $2a_1^{-1}\,1t_2^{-1}$, and $1t_2^{-2}$ final states in the order of increasing kinetic energy and intensity.[3,4] The fragmentation of these final states to positively charged fragments has been studied using Auger electron-ion coincidence spectroscopy by Kukk *et al.*[5] and Auger electron-ion-ion coincidence spectroscopy by Flammini *et al.*[6]

The observed pairs of ionic fragments[6] imply that also neutral fragments are created in dissociation of $CH_4^{2+}$ ions. Their detection is usually more difficult than of the charged fragments. However, if neutral fragments are created in excited states, their presence can be observed using ultraviolet-visible fluorescence spectroscopy or even through the direct detection of these particles, in the case that they have long lifetimes. Thus, Lyman-α and Balmer radiation from excited H atoms has been observed at the C 1s-to-Rydberg excitations of the methane molecule.[7] Additionally, some of us have recently investigated the neutral fragment production at the C 1s edge of $CH_4$ by observing coincidences between neutral particles and positive ions.[8] In that work, the neutral particles included both excited H atoms and vacuum ultraviolet (VUV) photons, but no heavier neutral fragments were detected. Some of the excited H atoms were shown to be in rather high Rydberg (HR) states (n ≥ 21; n is the principal quantum number of the Rydberg orbital) because they could be ionized with an electric field.

The production of neutral HR fragments at a core edge of a molecule was first detected in the $N_2$ molecule[9] and has later been reported in some other small molecules such as HCl,[10] $H_2O$,[11] CO,[12] and $CO_2$.[13] The peaks observed just above the inner-shell ionization potentials have been attributed to recapture processes that occur in the context of

a)Author to whom correspondence should be addressed. Electronic mail: kivimaki@iom.cnr.it

 

the so-called post-collision interaction (PCI).[14] Classically, a slow photoelectron experiences a change in the field of the molecular ion core (from +1 to +2), when a subsequently emitted faster Auger electron passes it. The two electrons can exchange energy in the field of the ion, as a result of which the photoelectron may even be recaptured to a HR orbital of the molecular ion. The ion thus ends up in a $val^{-2}$-$HR^1$ state. Upon dissociation, the Rydberg electron can be transferred to a HR orbital of a fragment. HR fragments have also been observed at photon energies corresponding to the excitation of inner-shell electrons to unoccupied valence and Rydberg orbitals. Resulting neutral core-excited states usually decay by electron emission, which in this case is called resonant Auger decay. Some resonant Auger transitions can populate final states which generate neutral HR fragments during dissociation.

In the 1980s, high-resolution studies of valence electron transitions experienced significant progress with the development of zero-kinetic energy photoelectron (ZEKE-PE) spectroscopy.[15,16] In the original scheme of ZEKE-PE spectroscopy,[15] the tunable photon energy obtained from a laser system was used to ionize a sample gas in (nearly) field-free conditions and electrons ejected with $E_{kin} \approx 0$ meV could be separated from other electrons with the aid of a delayed pulsed field. The experimental observation of long-lived HR states near ionization thresholds led to the development of another ZEKE detection scheme: pulsed field ionization (PFI) of HR states. HR states converging to the first ionization energy of a molecule have long lifetimes, which are proportional to $n^3$. An electric field, F, lowers the ionization potential of a species approximately by the amount of $\Delta E = 6\sqrt{F}$, where E is given in $cm^{-1}$ and F in V/cm.[17] When scanning the photon energy, HR states that are separated from the IP by less than $\Delta E$ become visible in the ZEKE spectrum measured with PFI. Pulsed fields used in these measurements are small, typically < 1 V/cm. A variant of this technique, mass-analyzed threshold ionization (MATI) spectroscopy,[18] has also been developed. It is closely related to ZEKE-PE spectroscopy, but it detects ions — instead of electrons — produced by pulsed field ionization. These ions can be identified based on their flight times in a time-of-flight (TOF) spectrometer. The main difficulty of MATI spectroscopy consists of detecting only ions produced by PFI of long-lived HR states while avoiding the detection of ions produced directly during the exciting laser pulse.[19] As far as we know, MATI spectroscopy has not been used in studies of inner-shell processes.

In the present study, we have developed an experimental technique that combines PFI with soft x-ray excitation. It allows us to determine which neutral fragments are created in HR states after core excitation processes in molecules. The experiment exploits PFI with high electric fields (of the order of kV/cm). A special feature of our apparatus is that field ionization of HR fragments occurs in a region that is separated from their place of creation. This allows us to perform measurements in the usual multi-bunch operation mode of a synchrotron light source. Here, we present first results obtained at the C 1s edge of the $CH_4$ molecule and interpret them with the aid of the previous coincidence studies and quantum chemical calculations.

## II. EXPERIMENTAL METHOD

The experiments were performed at the Gas Phase Photoemission beam line of the Elettra synchrotron radiation laboratory (Trieste, Italy). The beam line has been described in detail before.[20] Briefly, it uses an undulator as a light source and a spherical grating monochromator for the selection of the photon energy. The photon energy range of the beam line is 13.5-900 eV, and the radiation is linearly polarized. High resolving power ($>10^4$) can be achieved at most energies, thanks to five interchangeable gratings.

The basic idea of the experiment is as follows. The photon beam from the beam line crosses a molecular beam of sample gas in the interaction region. Let us assume that this interaction produces neutral fragments in HR states and that some of them move towards a TOF spectrometer, while positive ions are blocked by a suitable arrangement of potentials. When a HR fragment enters the first stage of the TOF spectrometer, it can be ionized by a pulsed electric field. The voltage pulse, thus, gives a reference time for the formation of a positive ion, created from the HR fragment. The flight time of this ion in the TOF spectrometer allows us to identify the original neutral HR fragment.

In order to measure the flight times of field-ionized species, we have modified the existing Wiley-McLaren TOF spectrometer[21] which has previously been used to detect neutral-particle–photoion coincidences.[8,13] The scheme of the modified experimental setup is shown in Fig. 1. A pulsed field ionization region (P in Fig. 1) was added between the interaction region (I) and acceleration region (A). Region P was kept as short as possible (2 mm), because it acts as a source of ions in the present experiment and its length affects mass resolution. The shape of the electrode between regions P and A was determined by construction requirements; in the following, we call it the "hat" electrode because of its shape. Another modification was the extension of the field-free drift tube from 105 mm to 203 mm in order to achieve a higher mass resolution for field-ionized fragments.

Before construction, numerical simulations using the SIMION software package were performed in order to estimate the potentials of the electrodes of the TOF spectrometer for optimum mass resolution. An iterative script was written for the simulations. The chosen grid potential was changed stepwise, while other potentials were kept fixed. At each step, thousands of ions of chosen masses and kinetic energy distributions were created in the entire field ionization region (P) and their arrival times were recorded at the detector plane. The value of the potential for the experiment was selected based on the resolution of the calculated TOF spectrum. The simulations suggested that the electric fields in regions A and P should have a ratio of ~8.3. This condition is fulfilled when the drift tube is set at −2.5 kV, the hat electrode is at ground, and a voltage pulse with amplitude of +300 V is applied. When the voltage pulse is off, the entrance mesh is at ground potential. Note that the modified TOF spectrometer still operates on the space focusing principles that Wiley and McLaren presented 60 yr ago.[21]

A potential of −100 V was applied to the mesh opposite to the ion TOF spectrometer in order to extract all positive ions

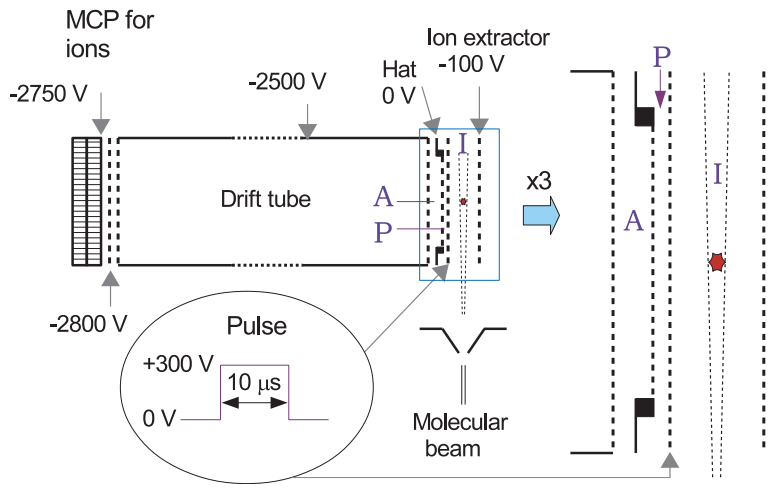


FIG. 1. The scheme of the experimental setup. HR fragments created in the interaction region (I) can enter the time-of-flight spectrometer. A positive pulsed potential (frequency 10 kHz) is applied to the electrode on the left side of interaction region; thus, it can field ionize HR fragments in region P. At the same time, ions created in region I are prevented from entering the instrument. The rising edge of the voltage pulse is used as a start signal for the flight time measurement, while ions hitting the microchannel plate (MCP) detector provide stop pulses. The width of the interaction region is 11 mm, the distance between the pulsed and hat electrodes is 2 mm, and the distance between the hat electrode and the drift tube is 5 mm along the central axis of the TOF spectrometer. The length of the drift tube is 203 mm. The drawing on the right side shows a magnification of regions A, P, and I.

created in the interaction region. Electrons and negative ions were repelled by a high negative potential of the drift tube. In this configuration, only photons and neutral fragments can enter the TOF spectrometer; the latter need to have an initial velocity — obtained in dissociation — directed towards the TOF spectrometer. The electric field in the field ionization region P was about 1.5 kV/cm, which can ionize H(n) atoms with $n \geq 22$ and C atoms below the first IP in the nd states with $n \geq 20$.[22] (C atoms in other nl states can be field ionized as well, but their energies are not given in Ref. 22.) As mentioned above, the rising edges of the pulsed voltage are used as start signal for time-of-flight measurements, while particles detected by the MCP detector of the TOF spectrometer provide stop signals. These signals were fed into a time-to-digital converter system (ATMD-GPX from ACAM Messelectronic GmBH).

Fragments in HR states that are in region P when the high voltage pulse arrives can be field ionized, accelerated towards the detector, and they can create time-correlated events. The MCP detector of the TOF spectrometer can detect other neutral particles (listed below) which do not give rise to peaks in the TOF spectra but contribute to the background. First, HR fragments can be field ionized in the acceleration region (A in Fig. 1), where there is a high static electric field. The resulting positive ions are accelerated towards the MCP detector and detected but are not time-correlated with the start pulses. Second, a typical MCP detector can directly detect neutral long-lived fragments, i.e., without conversion to ions, if their internal energy is higher than about 9 eV. In the present study, neutral fragments in Rydberg states with $n \approx 10$-15 belong to this category. Third, the detector can also detect VUV and soft x-ray photons. Photon emission is not correlated with the voltage pulses, but even if it were, it would lead to a sharp and well-isolated peak in the TOF spectrum. During the experiment, we saw no evidence of any contamination from ions created in region I in the MCP signal, when the potentials indicated in Fig. 1 were applied.

We finally note that by switching off the voltage pulsing we can record a sum of HR fragments, VUV, and soft x-ray photons as a function of photon energy. In such spectra, field ionization of HR fragments occurs in region A, but the resulting ions are not mass analyzed.

Methane used in the experiment was obtained from SIAD S.p.A. with stated purity of 99.95% and was used as delivered. It was introduced into the interaction region (I) as a molecular beam, using a stagnation pressure of 0.2 bars, expanded into vacuum through a 50 $\mu$m orifice. The background pressure of the chamber was $\sim 2 \times 10^{-7}$ mbars, rising to $1.6 \times 10^{-6}$ mbars with the molecular beam on. The molecular beam passes the interaction region without hitting the electrodes of the TOF spectrometer. The incident photon beam was almost circular in shape and had a diameter of about 300 $\mu$m. Measuring conditions remained stable during the measurements; in particular, the Elettra storage ring operated in the top-up mode with a practically constant electron current. Field ionization TOF spectra were recorded by repeating scans of 15 or 30 min for total measuring times of several hours. All data were used in the analysis, as they were similar within statistical fluctuations.

## III. EXPERIMENTAL RESULTS

The sum of HR fragments and energetic photons was measured by scanning the photon energy across the C 1s

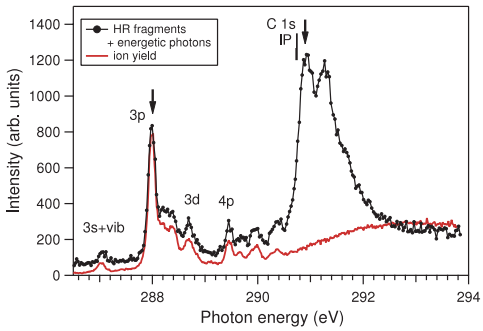


FIG. 2. The spectrum containing the sum of HR fragments, VUV, and soft x-ray photons at the C 1s edge of $CH_4$ in comparison with the ion yield. The curves have been normalized to the photodiode current and scaled at the 3p resonance. The photon energy resolution was about 120 meV. The arrows indicate the photon energies where the spectra of Fig. 3 were measured.

edge with the entrance mesh of the TOF spectrometer kept at ground and a static electric field of ∼5 kV/cm applied in region A (see Fig. 1). In this field, H(n) atoms with n ≥ 16 or so can be ionized.[22] The result obtained with an acquisition time of 10 s/energy point is shown in Fig. 2 (black dots). It is compared to the spectrum measured with the same setup and 1 s/point acquisition time, after changing the potential on the ion extractor mesh from −100 V to −3 V (lighter solid curve in Fig. 2). The potential of −3 V was set in order not to saturate the MCP detector. While the potential of −100 V in the ion extractor prevented all ions from entering the TOF spectrometer, the smaller potential of −3 V allowed some fast ions (with kinetic energy higher than ∼1.5 eV) to be detected. In this way, we could measure an ion yield spectrum of methane using the same photon resolution. The intensities of the two curves in Fig. 2 have been scaled to their peak heights at the C 1s → 3p transition located at 288.00 eV.[23] The sum of HR fragments and energetic photons shows a higher background than the ion yield measured with the same detector. This is mostly due to detection of VUV photons (in particular, Lyman emission in H atoms) produced by valence ionization processes and to a small extent also to the longer acquisition time needed to record the spectrum.

The curves in Fig. 2 show the well-known C 1s-to-Rydberg resonances between the photon energies of 287 and ∼290.7 eV, see, e.g., Refs. 23 and 24. In the neutral particle spectrum (black curve), an additional, distinct double-peak feature appears around 291 eV, i.e., just above the C 1s IP of 290.735 eV.[24] The curve resembles the H(HR)–$H^+$ coincidence yield presented in the previous study (Fig. 4 in Ref. 8) but displays higher statistics. The peaks observed just above the C 1s IP arise from HR fragments that are produced when a slow C 1s photoelectron is recaptured after Auger decay, and the resulting molecular ion in a HR state dissociates. The fine structure is due to the vibrational structure of the C $1s^{-1}$ state.[8] Such features were not observed in the Lyman-α or visible photon fluorescence yield spectra recorded at the C 1s edge.[7] To our knowledge, the x-ray fluorescence yield spectrum of methane at the C 1s edge has not been published, but, similarly to the x-ray fluorescence yield spectra of other small molecules,[25] we do not expect strong features appearing just above the core IP. In addition, the x-ray emission intensity at the carbon 1s edge is very weak. Apart from single-hole C 1s ionization, no new resonant or direct ionization channels open in the energy region of 291-293 eV: single core excitations are all located below the C 1s IP, next higher energy resonant transitions are core-valence double excitations located around 303 eV,[4] and there is no shape resonance in the C 1s ionization continuum of methane.[26]

In the following, we estimate the relative importance of the production of HR fragments at the C 1s IP. According to Flammini *et al.*,[6] $CH_x^+$ ions (x = 0-3) originating from dissociation after Auger decay have average kinetic energies below 1 eV; hence, we can assume that the fast ions detected in the lighter curve of Fig. 2 were predominantly $H^+$, with only marginal contributions from $H_2^+$ or heavier ions. The ion yield curve also contains a portion from HR fragments and energetic photons, which were not affected by the change of the potentials in the ion extraction region. The count rate of all HR fragments at the maximum of the black curve was about 100 Hz. In the "fast ion" yield, about 870 counts/s were detected at the same photon energy, including ∼100 initially neutral HR fragments. We thus obtain a branching ratio of 11.5% for HR fragments at the C 1s IP. However, we should consider the collection efficiency of $H^+$ ions. Kinetic energy release distributions have been reported for different fragmentation channels of the doubly charged methane.[6,27] The results of different studies show quite large variations. As an average, we assume for $H^+$ ions a Gaussian kinetic energy distribution with the maximum at 3.5 eV and full width at half maximum of 3.0 eV. Assuming additionally an isotropic angular distribution, we simulated using the SIMION software package the trajectories of $H^+$ ions in the TOF spectrometer in the experimental conditions of the "fast ion" yield (the lighter curve in Fig. 2). We calculate a transmission of ∼13% for all $H^+$ ions. More importantly, for comparison with the HR fragment yield, we estimate that about 60% of those $H^+$ ions that are ejected within the acceptance angle of the TOF spectrometer become detected. Finally, at 300 eV photon energy, 52.6% of all ions are $H^+$.[2] This very crude estimate suggests that neutral HR fragment production amounts to ∼4% of the positive ion yield just above the C 1s IP, a result which is similar to the ∼3% found for the intensity ratio between neutral HR fragments and ionic fragments just above the N 1s IP for the $N_2$ molecule.[9] These numbers indicate that the production of neutral HR fragments is a minor, but not negligible fragmentation channel in photoionization experiments performed just above core IPs. At the C 1s → 3p resonance of $CH_4$, the branching ratio of all HR fragments drops by one order of magnitude with respect to the one just above the C 1s IP.

TOF spectra of HR fragments created by photoionization of methane molecules were measured using pulsed field ionization at the C 1s → 3p resonance and just above the C 1s IP, where the most intense production of HR fragments was expected based on the black curve in Fig. 2. The spectrum recorded above the C 1s IP is shown in Fig. 3(a); its intensities were obtained by binning the arrival times within 4 ns wide windows. The detection window opened 440 ns after each start

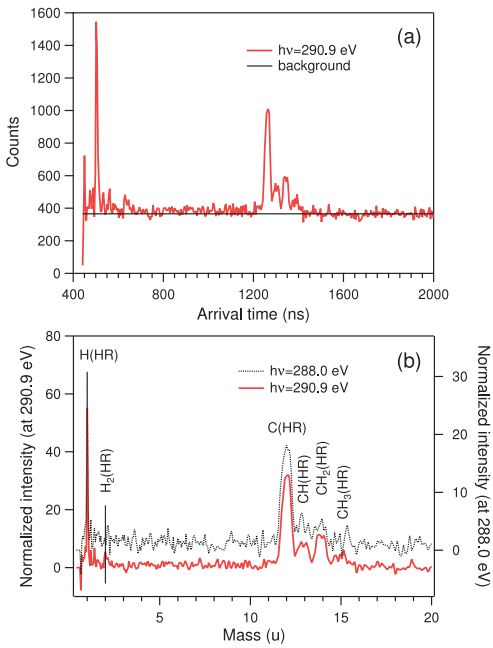


FIG. 3. (a) The solid curve shows the time-of-flight spectrum of field-ionized HR fragments of the $CH_4$ molecule measured at the photon energy of 290.9 eV (just above the C 1s IP). The black horizontal line shows the constant background subtracted from the spectrum before its conversion to a mass scale. (b) The background-subtracted TOF spectra shown on a mass scale. The measuring times were 6 and 12.5 h at the photon energies of 288.0 and 290.9 eV, respectively. The intensities of the two spectra have been normalized to the photodiode current and measuring time. A vertical line shows the expected position of the $H_2$(HR) fragment.

signal in order to avoid noise from the high-voltage pulses. Some artifact signals still remain around 500 ns, close to the highest peak of the TOF spectrum. Fig. 3(b) shows the data on a mass scale (after background subtraction), assigning the two most intense peaks to H(HR) and C(HR) atoms. The assignment of the second highest peak to C(HR) was confirmed by similar measurements of the $CO_2$ molecule.

At the photon energy just above the C 1s IP (lower curve in Fig. 3(b)), we attribute the production of HR fragments to recapture processes and subsequent dissociation of the parent ions. This is in agreement with the earlier studies of the neutral HR fragment production in small molecules, e.g., Refs. 8, 9, and 13. We observe that such processes in methane can yield different HR fragments; in fact, all possible neutral HR fragments appear in the spectrum. ($CH_4$(HR) molecules are not expected to be detected, since they cannot have a substantial velocity component in the direction perpendicular to the molecular beam.) Their branching ratios, as obtained from a Gaussian fit to the background-subtracted TOF spectrum of Fig. 3(a), are presented in Table I. The $H_2$(HR) peak is weak but appears exactly in the correct position in the lower spectrum of Fig. 3(b). In contrast, the $H_2$(HR) peak does not rise above the noise level in the upper spectrum of Fig. 3(b). The error

TABLE I. Branching ratios of the neutral HR fragments at 290.9 eV photon energy (this work), singly charged positive ions created with 300 eV photons[2] (above C 1s edge), and ions observed in coincidence with Auger electrons.[5]

| | This work | | Reference 2 | Reference 5 |
|---|---|---|---|---|
| H(HR) | $23^{+1}_{-3}$ | $H^+$ | 52.6 | 42.9 |
| $H_2$(HR) | $3^{+1}_{-3}$ | $H_2^+$ | 2.3 | 4.6 |
| C(HR) | 42 ± 1 | $C^+$ | 9.7 | 11.5 |
| CH(HR) | 11 ± 1 | $CH^+$ | 14.4 | 16.5 |
| $CH_2$(HR) | 15 ± 1 | $CH_2^+$ | 15.4 | 18.7 |
| $CH_3$ (HR) | 7 ± 1 | $CH_3^+$ | 4.4 | 5.8 |
| ... | ... | $CH_4^+$ | 1.2 | ... |

limits given in Table I contain a statistical fitting error of ±1%. The total errors in the H(HR) and $H_2$(HR) intensities are larger because of the noise caused by the high-voltage pulse which appears near the arrival times of the lightest fragments.

The branching ratios of neutral HR fragments observed in the present work (see Table I) are completely different from those of the corresponding ions observed with mass spectroscopy at the photon energy of 300 eV.[2] They also differ from the branching ratios obtained by fitting the Auger electron-photoion coincidence spectrum from Ref. 5 (last column in Table I), where some fast $H^+$ ions escaped detection. H(HR) fragments have previously been detected in neutral-particle–photoion coincidence experiments,[8] while the $CH_4$(HR) molecule and molecular $CH_x$(HR) (x = 1-3) fragments have been detected after 60 eV electron impact on methane.[28]

The field-ionization mass spectrum measured at the C 1s → 3p excitation (Fig. 3(b), upper curve) has worse statistics, making the changes in the relative peak intensities between the resonance and the C 1s threshold uncertain. However, also the spectrum measured at the resonance is clearly dominated by the C(HR) and H(HR) fragments. The normalized intensities of the peaks indicate that the production of HR fragments is about two times more probable just above the C 1s threshold compared to the C 1s → 3p resonance. As the intensity ratio of the peaks is about 1.5 (instead of 2) in Fig. 2, we estimate that VUV and soft x-ray emission contribute with about 25% to the intensity of the C 1s → 3p peak in the sum of HR fragments and energetic photons spectrum. If we take into account the photoabsorption cross section, which is ~10 times larger at the C 1s → 3p resonance than just above the C 1s threshold,[24] we get an order-of-magnitude estimate that, per absorbed incident soft x-ray photon, C 1s photoionization just above the core IP is about 20 times more likely to produce HR fragments than the C 1s → 3p resonant excitation.

The angular distributions of ejected neutral HR fragments influence the results obtained with the present setup. Such effects are, however, expected to be very weak in the present case. Kosugi has reported angle-resolved fragment ion yields at the C 1s edge of methane.[29] Slightly different intensities at 0° and 90° were observed at most excitation energies, but not at the C $1s^{-1}$ → 3p, ν = 0 resonance. Geometric distortion in the core-excited state of the $CH_4$ molecule through vibronic coupling was shown to be essential for

anisotropic fragmentation. As vibronic coupling does not play a role in the transitions to the vibrationless electronic states C $1s^{-1}$ $3p^1$ and C $1s^{-1}$, we expect that angular effects have not modified the intensity ratios of the HR fragment peaks in the measured field ionization mass spectra (Fig. 3). The situation would be different, for instance, in core-excited linear molecules that are preferentially oriented either parallel or perpendicular to the electric vector of the linearly polarized incident light and keep that orientation until dissociation (in the so-called axial recoil approximation). An instrument that is suitable for the measurement of angle-integrated intensity ratios of HR fragments in any molecules could be constructed by installing a present-type TOF spectrometer at the so-called magic angle (54.7°). Alternatively, a setup of two TOF spectrometers mounted at 0° and 90° could be used, which would allow the determination of the angular asymmetry parameters of neutral HR fragments.

## IV. THEORETICAL METHODS AND RESULTS

The *ab initio* calculations performed in this work were based on the following assumptions: neutral fragments with a HR electron (i.e., the HR fragments observed in our experiment) have a molecular ion core with the high-Rydberg electron at a large distance ($\langle r \rangle \propto n^2$) having no effect on bonding in the molecular core (the core ion model used in Ref. 30); molecular dissociation can take place just as if the HR electron were not present. We have also assumed that the energies of the neutral HR fragments $CH_x$(HR) (x = 0-4), H(HR), and $H_2$(HR) are similar to the energies of the corresponding ions $CH_x^+$ (x = 0-4), $H^+$, and $H_2^+$.

Core ionization and the following single or double Auger decay will result in the production of $CH_4$ dications or trications (parent ion), which have not been observed. In the model, the HR electron stays in the vicinity of the parent ion, but in the calculations, the HR electron has been ignored. In order to study energetically possible fragmentation channels after parent ion creation, the energies of the dication (trication) as well as the energies of created ions were calculated at the multiconfigurational second-order perturbation (CASPT2) level of theory with a basis set of valence double zeta accuracy with polarization functions (ANO-L-VDZP) using the Molcas 7 package.[31] The experimental ground state geometry, i.e., tetrahedral symmetry with the C–H bond length of 1.089 Å, was taken as the starting point. Using this geometry, the vertical ionization energies of the parent ion(s) were calculated. For dissociation fragments $CH_x^+$ (x = 1-3), the geometry was optimized. The resulting geometries are shown in Fig. 4.

The calculated energies of the $CH_4$ dication and $CH_x^+$ (x = 0-3) ions with corresponding H-based fragments are summarized in Fig. 4. Energies are given in eV with respect to the calculated vertical double ionization energy (38.65 eV) of the lowest singlet state, $^1$E. The energies calculated here are slightly lower than those given in Ref. 1, but the ordering of the levels is the same. Vertical triple ionization energy was calculated to be 35.68 eV above the vertical double ionization energy and it is, therefore, well above the energy needed for complete atomization of the methane molecule.

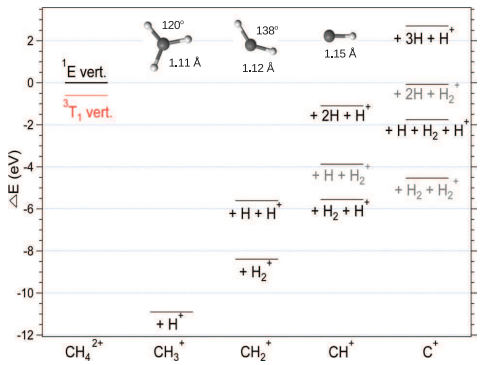


FIG. 4. Energies for different ion pairs after $CH_4$ dication fragmentation and relaxation. On the left, vertical double ionization energies for the lowest singlet ($^1$E) and triplet ($^3T_1$) states of the $CH_4$ dication are given. $H_2^+$ has only been observed in coincidence with $CH_2^+$ ions;[6,32] hence, other fragmentation channels with $H_2^+$ are displayed in gray.

The observed HR fragments have long life times and so have many states of the molecular fragment ions calculated in this study. This was investigated by calculating the potential energy curves (PECs) for the ions $CH_x^+$ (x = 1-3) along one of the C–H bonds at the same level of theory, while optimizing geometry at each bond length. PECs for all three $CH_x^+$ ions showed a similar behavior with at least one non-dissociative state. In addition, we followed the dynamics of the parent dication/trication on their ground state potential energy surface by following the Minimum Energy Path (MEP), where the geometry of the next step is chosen according to the lowest energy. Our MEP calculations do not take into account the vibrational motion observed in the core ionized state.[33]

## V. DISCUSSION

### A. Above the C 1s threshold

Very recently, recapture processes to Rydberg states up to n = 15-18 were *directly* observed in a high-resolution photoelectron spectrum of Xe, measured 0.02 eV above the Xe $4d_{5/2}$ photoionization threshold.[34] Even higher Rydberg orbitals were populated, but those transitions formed an unresolved spectral feature. Similar observations do not exist for molecules. Their spectra would be more difficult to interpret because more electronic states are available and vibrations would also complicate the situation. However, the PCI effect is conceptually the same for atoms and molecules, and there is absolutely no reason why recapture processes should not take place in molecules. In fact, they have been used to explain the enhanced production of HR fragments in just-above-threshold core-level photoionization of small molecules,[8–13] as mentioned in the Introduction.

The photoelectron recapture is an ultrafast process which occurs before the dissociation of the molecular ion. More formally, one should treat the photoelectron emission, Auger decay, and photoelectron recapture as a one-step scattering process.[35] It is, therefore, actually incorrect to say that the

photoelectron recapture takes place after the Auger decay. We nevertheless use the two-step picture, because it is conceptually easy to follow and it can explain the major features of the experimental results. HR fragments are thought to arise when molecular ions in HR states dissociate. An electron in a distant HR orbital interacts very weakly with the electrons in valence orbitals; hence, it is not expected to affect how the doubly charged molecular core dissociates after Auger decay. After dissociation, the HR electron can attach, at least in principle, to any ionic fragment, forming also neutral fragments in HR states.

Next we consider what information can be obtained by comparing the ionic fragmentation after Auger decay[5,6] to our field ionization mass spectra of HR fragments. If the recaptured electrons attached with equal probability to any ionic fragment after dissociation, our field-ionized mass spectra of HR fragments would show similar relative intensities as the ion spectra integrated over all the final states of Auger decay. In practice, some fast $H^+$ ions escaped detection in the coincidence measurements,[5,6] so the relative intensity of $H^+$ appeared too low in the spectra. The branching ratio of $H^+$ after Auger decay is probably above 50%, as was found in non-coincidence measurements[2] at the photon energy 300 eV (see the fourth column in Table I), where C 1s single-hole ionization is the most likely process. The relative intensities of the other singly charged ions produced after Auger decay are given in Table I and they increase in the following order: $H_2^+$, $CH_3^+$, $C^+$, $CH^+$, and $CH_2^+$.[5] We directly see that the order is not the same as in the field-ionization mass spectrum shown in Fig. 3(b) (lower curve), where the C(HR) peak displays by far the greatest intensity, being almost three times higher than $CH_2$(HR). The intensities of the molecular fragments $CH_x$(HR) (x = 1-3) follow the same order in the present work and in Ref. 5, although with somewhat different intensity ratios.

Calculation of potential energy curves of the $CH_x^+$ (x = 1-3) ions shows that each of these ions can form stable and possibly also metastable states, which is confirmed by their detection in mass spectroscopic studies where flight times are usually in the microsecond range. The calculated PECs of different ions (not shown) do not explain why a particular $CH_x$(HR) (x = 1-3) fragment should be favored. Here, only a few lowest energy curves should be of importance since higher electronically excited states would either dissociate or autoionize to the continuum of a lower ionic state before detection. Calculated energies depicted in Fig. 4 show that vertical double ionization to the lowest dication states will enable, on purely energetic grounds, fragmentation to all $CH_x^+$ (x = 0-3) ions. According to these energies, two-step processes suggested by Flammini *et al.*[6] should occur via intermediate $CH_3^+$ ions having considerable internal energy, since it is not energetically possible for the relaxed $CH_3^+$ ion in the ground state to fragment further.

Kukk *et al.*[5] found that the production of the $CH_3^+$ ion seems to be uniquely correlated with the population of the $1t_2^{-2}$ ($^1$E) final state in Auger decay. In other words, $CH_4^{2+} \rightarrow CH_3^+ + H^+$ dissociation is not observed to occur after any other Auger transitions. If this is true, when the $CH_4^{2+}$ ion in this particular electronic state recaptures the photoelectron in a HR orbital, subsequent dissociation should be the only channel that produces $CH_3$(HR) fragments. Similarly, the fragmentation $CH_4^{2+} \rightarrow CH_2^+ + H_2^+$ only takes place after Auger decay to the $1t_2^{-2}$ ($^1T_2$) final states.[5] This is also supported by results in Refs. 6 and 32, where $H_2^+$ was detected in coincidence with $CH_2^+$ ions only. If the $CH_4^{2+}$ in this final state recaptures the C 1s photoelectron, the subsequent dissociation provides the predominant channel to obtain $H_2$(HR) fragments. The observation of the $CH_3$(HR) and $H_2$(HR) fragments indicates that in the dissociation of the $CH_4^+$(HR) ions, either a heavy or light fragment can retain the electron in the HR orbital. For energetically higher final states of Auger decay, second step dissociation channels are open and higher internal energy of the ion can lead to further fragmentation.

Thus, the presence of the $CH_3$(HR) fragment strongly implies that some of the observed HR fragments are produced after single Auger decay, when the slow C 1s electron is recaptured. If $CH_3$(HR) acts as an intermediate, as suggested by Flammini *et al.*,[6] this could explain the reduced intensity ratios of the CH(HR) and $CH_2$(HR) fragments when compared with the corresponding ions after Auger decay (Table I). This could be rationalized if in the subsequent dissociation step the electron in the HR orbital can be transferred to either a $CH_x^+$ ion or to a proton. However, this scheme of sequential dissociations after Auger decay does not explain the large intensity of the C(HR) peak in our spectrum (Fig. 3) and thus the single Auger decay cannot be the only source of HR fragments.

We note that the relative intensity of the $C^+$ ion created after Auger decay surpasses those of $CH^+$ and $CH_2^+$ if one considers Auger decay to the final states $2a_1^{-2}$ and it still increases when going to lower kinetic energies (or higher binding energies).[5] The final states located in that lowest kinetic energy part of the Auger spectrum have general electron configurations of type $(2a_1 1\,t_2)^{-3}\,virt^1$ and they arise from correlation effects.[36] The calculated energy for vertical triple ionization is 35.68 eV above the vertical double ionization threshold, so a second-step (participator) Auger decay is possible for higher electronic states of $CH_4^{2+}$, which would lead to emission of slow electrons and the creation of triply charged states of $CH_4$. C 1s ionization in methane initiates a symmetric stretch vibrational mode and this nuclear motion continues after Auger decay. Our MEP calculations for both the dication and trication ground states did not account for any initial motion of the nuclei. Nonetheless, according to our calculations, direct double/triple ionization from the neutral ground state resulted in lengthening of all bonds before the charge localization and resulting charge separation. For higher electronic states, the greater internal energy available for nuclear dynamics (most probably initiated already in the core-ionized state) results in a more complete fragmentation even if the proton left the parent ion slightly before neutral hydrogen atoms.

Triple ionized states can also be reached in double Auger transitions, where two electrons are emitted simultaneously. In that case, they can share the available energy in a continuous manner. Using a magnetic bottle time-of-flight spectrometer, Eland *et al.*[37] have studied processes that lead to triple ionization of methane after the removal of a C 1s electron.

They determined that the energies of the triply ionized states begin from ~67 eV above the ground state of the $CH_4$ molecule and they form clear maxima around 76.4 (±0.2) eV for the $1t_2^{-3}$ states and 86.2 (±0.2) eV for the $2a_1^{-1}\,1t_2^{-2}$ states. Taking into account the C 1s IP of 290.375 eV,[24] spectral intensity due to double Auger decay is then located below the kinetic energy of 223 eV. The relative ion yields of Ref. 5 did not extend to such low kinetic energies, but one could extrapolate that — within the series $CH_x^+$ (x = 0-3) — the $C^+$ ion is the most probable dissociation product following double Auger decay. A study of multiply ionized methane created in collisions with swift $Xe^{21+}$ ions also indicates that $CH_4^{3+}$ most likely fragments to $C^+ + H^+ + H^+ + 2H$.[38] Eland *et al.*[37] determined that the energy distributions of electrons resulting from emission of two Auger electrons display increased intensity towards zero kinetic energy. The intensity ratio of triple ionization (double Auger) to double ionization (normal Auger) was found to be approximately 0.035:1 at 296 eV.

We believe that double Auger decay is mainly responsible for the large intensity of C(HR) fragments in our field-ionization spectrum measured above the C 1s IP. Sheinerman *et al.*[39] have studied experimentally and theoretically the post-collision interaction effect in the context of double Auger decay from the $2p^{-1}$ states of Ar. They found that the PCI distortion of the photoelectron line profile is clearly larger for double Auger decay than for single Auger decay, if the photoelectron is slower than both the Auger electrons (see Fig. 3 in Ref. 39). This is because the ionic field experienced by the photoelectron changes by two charge units in such double Auger decay, Z: +1 → +3. The larger energy shift towards lower kinetic energies and the larger width of the photoelectron line also imply, in our opinion, that recapture of the photoelectron becomes more likely in double Auger decay than in single Auger decay. On the other hand, there is not much difference in PCI distortion between the double and single Auger decay, if the photoelectron is faster than one of the Auger electrons emitted in double Auger decay.[39] A similar result was also obtained when the second Auger electron is emitted sequentially (in Auger cascade).

We can illustrate the suggested pathway to the production of C(HR) fragments by writing the intermediate steps in the context of double Auger decay,

$$\begin{aligned}
CH_4 + h\nu &\rightarrow CH_4^+(C\ 1s^{-1}) + e_{ph} && \text{(C 1s ionization)}\\
&\rightarrow CH_4^{3+}(Val^{-3}) + e_{ph} + e_{A1} + e_{A2} && \text{(double Auger decay)}\\
&\rightarrow CH_4^{2+}(Val^{-3}\text{-HR}) + e_{A1} + e_{A2} && \text{(recapture to HR orbital)}\\
&\rightarrow C(HR) + 2H^+ + 2H + e_{A1} + e_{A2} && \text{(dissociation).}
\end{aligned}$$

Here, $e_{ph}$ is a C 1s photoelectron and $e_{A1}$, $e_{A2}$ are two Auger electrons. The protons and H atoms in the last step could, in principle, also appear as molecular species ($H_2$, $H_2^+$); however, $H_2^+$ has not been observed in coincidence with $C^+$.[6,32] Dissociation in the last step could also produce H(HR) fragments, but C(HR) seems to be the preferred outcome. A reason for this could be that the overlap of the wavefunctions of the occupied HR orbital before dissociation (i.e., in the $CH_4^{2+}(Val^{-3}\text{-HR})$ ion) and after dissociation (in C(HR) or H(HR)) should be larger, when a C(HR) fragment rather than a H(HR) fragment is formed. This can be expressed in another way: a HR orbital of C(HR) should be very similar to the corresponding HR orbital of $CH_4^{2+}$(HR), since the latter is also built around the central C atom, and this should favor the formation of C(HR) fragments after recapture processes in the context of double Auger decay.

### B. At the C 1s → 3p resonance

The intensity of HR fragments is surprisingly high at the C 1s → 3p resonance, considering that the well-established mechanism for their production — recapture following core photoelectron emission — cannot play a role here because no photoelectron is emitted. Thus, there must be other processes that populate HR states of $CH_4^+$ and $CH_4^{2+}$ ions, which upon dissociation yield HR fragments. The simplest processes that can create $CH_4^+$(HR) ions at the C 1s → 3p resonance are shake-up transitions during resonant Auger decay: when a resonant Auger electron is emitted, the spectator electron in the 3p orbital may shake up simultaneously to a higher np orbital. Armen[40] has calculated shake-up and shake-off probabilities for an electron in a hydrogenic nl orbital in light atoms, when the (apparent) central charge suddenly changes from Z to Z + 1. He found that the probability $P_{n,m}$ for an nl → ml shake-up transition approaches $m^{-3}$, when m ≫ n. In the present experiments, m is of the order of 20-30 (for the HR fragments), so $P_{n,m}$ would be in the range of $10^{-5}$-$10^{-4}$.

Another mechanism that could produce $CH_4^+$(HR) ions is resonant double Auger decay (or resonant Auger shake-off decay, a term used in Ref. 41) followed by electron recapture. If two electrons are emitted in a resonant double Auger process, their kinetic energy distribution may follow the pattern of asymmetric energy sharing observed in double Auger decay of Ar atoms:[42] one electron tends to retain most of the available energy while the other electron is slow. Hints of such a trend were observed also in methane.[37] The situation resembles that in recapture processes above core ionization threshold: a fast electron and a slow electron are in the vicinity of a doubly charged molecular core, whereby the slow electron could be recaptured in a Rydberg orbital of the molecular ion. Armen[40] calculated for light atoms that the recapture probability can be quite large for an electron in the continuum; it can, in

fact, be much larger than the shake-off probability in resonant Auger decay. Since the latter was predicted to be in the range of $10^{-3}$-$10^{-2}$ for Z = 5 (and by extrapolation also for carbon, Z = 6), a slow electron emitted in resonant double Auger decay may produce HR states of the parent ion more efficiently than shake-up transitions during usual resonant Auger decay. The two channels cannot be resolved experimentally, and their division may not even be conceptually necessary.

We may also consider sequential emission of two electrons in the de-excitation of a core-excited state. These processes happen when the final state of the first-step resonant Auger decay is so highly excited that it can decay further by emitting a second electron. However, in this scenario, the first emitted resonant Auger electron is fast; hence, the second emitted electron cannot overtake it. Even if the lifetime of the valence excited state were in the femtosecond range, it is questionable whether the two electrons can exchange energy so that the slower electron could be recaptured.

As in the case of core-ionization just above threshold, the production of $CH_4^+$(HR) ions is not sufficient to explain the large intensity of the C(HR) peak at the C 1s → 3p resonance (Fig. 3(b)). According to our energy-level calculations, some of the $2a_1^{-2}\,1t_2^{-1}$ nl final states of resonant double Auger decay are located above the lowest triple ionization threshold, but second-step Auger decay to the corresponding $1t_2^{-3}$ states is not expected to occur; hence, $CH_4^{2+}$(HR) ions may not be produced in this way. In the isoelectronic Ne atom, $Ne^{3+}$ ions have been observed at the 1s → 3p resonance.[41] They were attributed to direct emission of three electrons, $Ne(1s^{-1}\,3p^1) \rightarrow Ne^{3+} + 3e^-$, since there are no suitable intermediate states available for these ions to be produced in sequential Auger transitions. The branching ratio of that channel, which could be called resonant triple Auger decay, was ∼3% of all resonant Auger channels. This value is surprisingly large. Coincidence measurements between $Ne^{3+}$ ions and threshold electrons[41] showed that these ions can be produced together with very slow electrons. Similar processes should happen also in methane, even though likely with a lower probability. We, therefore, expect that the decay $CH_4(C\,1s^{-1}\,3p^1) \rightarrow CH_4^{3+} + 3e^-$ occurs and that some of the emitted electrons have very low kinetic energies. The recapture of the slowest Auger electron in a HR orbital would lead to the creation of $CH_4^{2+}$(HR) ions. We can also consider that the $CH_4^{2+}$(HR) ions may be directly created in resonant Auger decay processes. There should be no sharp step in the energy distribution of the complete system, composed of the molecular ion and three electrons, above and below any ionization potential. Therefore, we can imagine that for Auger transitions $CH_4(C\,1s^{-1}\,3p^1) \rightarrow CH_4^{3+} + 3e^-$ with one very slow electron, there are also such transitions where the third electron does not make it into the continuum but ends up in a HR orbital of the $CH_4^{2+}$ ion. When created by this or any other mechanism at the C 1s → 3p resonance, the dissociation of $CH_4^{2+}$(HR) ions mostly yields C(HR) fragments.

## VI. CONCLUSION

We have observed HR fragments at the C 1s edge of the methane molecule by exploiting pulsed field ionization. The sum of the yields of HR fragments and VUV and soft x-ray photons shows all core-to-Rydberg excitations, but only HR fragments contribute to the most intense features that appear just above the C 1s IP. The pulsed-field ionization mass spectrum measured at the C 1s threshold revealed that the HR fragment signal is composed of all possible neutral species: $CH_3$(HR), $CH_2$(HR), CH(HR), C(HR), $H_2$(HR), and H(HR), among which the atomic fragments display the highest intensities. The production of HR fragments is attributed to dissociation of $CH_4^+$ and $CH_4^{2+}$ ions in HR states. At the C 1s threshold, such ionic states can be populated by recapture processes, in which the slow photoelectron loses energy and returns to a HR orbital of the molecular ion, while the fast Auger electron gets even more kinetic energy. The large intensity of the C(HR) fragments can be explained by recapture processes occurring in the context of double Auger decay. Even though double Auger decay is far less likely than single Auger decay, the higher recapture probability of the slow photoelectron after double Auger decay enhances the contribution of this decay channel in the production of HR fragments. However, $CH_3$(HR) and $H_2$(HR) should mostly be created in recapture processes after single Auger decay.

The field-ionization mass spectrum measured at the C 1s → 3p resonance appears similar to the spectrum taken above the C 1s threshold. We, therefore, suggest that the same $CH_4^+$(HR) and $CH_4^{2+}$(HR) states are responsible for the production of the HR fragments both at the C 1s → 3p resonance and just above the C 1s ionization threshold. The probability for the production is considerably smaller, by a factor of ∼20, at the C 1s → 3p resonance. The HR fragment production at the resonance may follow direct resonant multiple Auger transitions to the $CH_4^+$(HR) and $CH_4^{2+}$(HR) states, which subsequently dissociate. Alternatively, one may consider that such ionic states become populated, when the slowest of two or three Auger electrons emitted in resonant double or triple Auger decay, respectively, is recaptured by the molecular ion. The experimental method described in this work can also be used in valence ionization studies.

## ACKNOWLEDGMENTS

We are grateful to A. Stolfa for the construction of new pieces for the ion TOF spectrometer and to E. Kukk for providing us with the coincidence ion data from Ref. 5. We thank K. C. Prince for critical reading of the manuscript. A.S. acknowledges funding from the Swedish Research Council and from the Academy of Finland's Research Council for Natural Sciences and Engineering. J.A.K. acknowledges funding from the Finnish Academy of Science and Letters and from the Vilho, Yrjö, and Kalle Väisälä Foundation. The research leading to these results has received funding from the European Community's Seventh Framework Programme (No. FP7/2007-2013) under Grant Agreement No. 312284.

[1]G. Dujardin, D. Winkoun, and S. Leach, Phys. Rev. A **31**, 3027 (1985).
[2]W. Wolff, L. Sigaud, E. C. Montenegro, V. L. B. de Jesus, R. L. Cavasso Filho, S. Pilling, and A. C. F. Santos, J. Phys. Chem. A **117**, 56 (2012), and references therein.
[3]K. Ueda, M. Okunishi, H. Chiba, Y. Shimizu, K. Ohmori, Y. Sato, E. Shigemasa, and N. Kosugi, Chem. Phys. Lett. **236**, 311 (1995).

[4]A. Kivimäki, M. Neeb, B. Kempgens, H. M. Köppe, and A. M. Bradshaw, J. Phys. B: At., Mol. Opt. Phys. **29**, 2701 (1996).
[5]E. Kukk, G. Prümper, R. Sankari, M. Hoshino, C. Makochekanwa, M. Kitajima, H. Tanaka, H. Yoshida, Y. Tamenori, E. Rachlew, and K. Ueda, J. Phys. B: At., Mol. Opt. Phys. **40**, 3677 (2007).
[6]R. Flammini, M. Satta, E. Fainelli, G. Alberti, F. Maracci, and L. Avaldi, New J. Phys. **11**, 083006 (2009).
[7]K. Jakubowska, G. Vall-llosera, A. Kivimäki, M. Coreno, E. Melero Garcia, M. Stankiewicz, and E. Rachlew, J. Phys. B: At., Mol. Opt. Phys. **40**, 1489 (2007).
[8]A. Kivimäki, J. Álvarez-Ruiz, R. Sergo, and R. Richter, Phys. Rev. A **88**, 043412 (2013).
[9]Y. Hikosaka, P. Lablanquie, and E. Shigemasa, J. Phys. B: At., Mol. Opt. Phys. **38**, 3597 (2005).
[10]Y. Hikosaka, T. Kaneyasu, and E. Shigemasa, J. Korean Phys. Soc. **53**, 3798 (2008).
[11]J. R. Harries, T. Gejo, K. Honma, M. Kuniwake, J. P. Sullivan, M. Lebech, and Y. Azuma, J. Phys. B: At., Mol. Opt. Phys. **44**, 095101 (2011).
[12]T. Gejo, T. Tamura, K. Honma, E. Shigemasa, Y. Hikosaka, and Y. Tamenori, J. Chem. Phys. **136**, 054201 (2012).
[13]A. Kivimäki, M. Alagia, and R. Richter, J. Phys. B: At., Mol. Opt. Phys. **47**, 155101 (2014).
[14]M. Yu, S. A. Kuchiev, and Sheinerman, Sov. Phys. Usp. **32**, 569 (1989).
[15]K. Müller-Dethlefs, M. Sander, and E. W. Schlag, Chem. Phys. Lett. **112**, 291 (1984).
[16]K. Müller-Dethlefs and E. W. Schlag, Annu. Rev. Phys. Chem. **42**, 109 (1991).
[17]F. Merkt, A. Osterwalder, R. Seiler, R. Signorell, H. Palm, H. Schitz, and R. Gunzinger, J. Phys. B: At., Mol. Opt. Phys. **31**, 1705 (1998).
[18]L. Zhu and P. Johnson, J. Chem. Phys. **94**, 5769 (1991).
[19]F. Merkt, Annu. Rev. Phys. Chem. **48**, 675 (1997).
[20]K. C. Prince *et al.*, J. Synchrotron Radiat. **5**, 565 (1998).
[21]W. C. Wiley and I. H. McLaren, Rev. Sci. Instrum. **26**, 1150 (1955).
[22]A. Kramida, Yu. Ralchenko, J. Reader, and NIST ASD Team, NIST Atomic Spectra Database version 5.2, National Institute of Standards and Technology, Gaithersburg, MD, 2014, available at http://physics.nist.gov/asd.
[23]M. Tronc, G. C. King, R. C. Bradford, and F. H. Read, J. Phys. B: At., Mol. Opt. Phys. **9**, L555 (1976).
[24]M. de Simone, M. Coreno, M. Alagia, R. Richter, and K. C. Prince, J. Phys. B: At., Mol. Opt. Phys. **35**, 61 (2002).
[25]M. Alagia *et al.*, Phys. Rev. A **71**, 012506 (2005).
[26]H. M. Köppe, B. S. Itchkawitz, A. L. D. Kilcoyne, J. Feldhaus, B. Kempgens, A. Kivimäki, M. Neeb, and A. M. Bradshaw, Phys. Rev. A **53**, 4120 (1996).
[27]B. Wei, Y. Zhang, X. Wang, D. Lu, G. C. Lu, B. H. Zhang, Y. J. Tang, R. Hutton, and Y. Zhou, J. Chem. Phys. **140**, 124303 (2014), and references therein.
[28]K. Furuya, K. Ishikawa, and T. Ogawa, Chem. Phys. Lett. **319**, 335 (2000).
[29]N. Kosugi, J. Electron Spectrosc. Relat. Phenom. **79**, 351 (1996).
[30]R. S. Freund, S. M. Tarr, and J. A. Schiavone, J. Chem. Phys. **79**, 213 (1983).
[31]F. Aquilante, L. De Vico, N. Ferré, G. Ghigo, P.-Å. Malmqvist, P. Neogrády, T. B. Pedersen, M. Pitonak, M. Reiher, B. O. Roos, L. Serrano-Andrés, M. Urban, V. Veryazov, and R. Lindh, J. Comput. Chem. **31**, 224 (2010).
[32]E. Fainelli, G. Alberti, R. Flammini, F. Maracci, P. Bolognesi, M. Mastropietro, and L. Avaldi, J. Electron Spectrosc. Relat. Phenom. **161**, 51 (2007).
[33]T. X. Carroll, N. Berrah, J. Bozek, J. Hahne, E. Kukk, L. J. Saethre, and T. D. Thomas, Phys. Rev. A **59**, 3386 (1999).
[34]S. Kosugi, M. Iizawa, Y. Kawarai, Y. Kuriyama, A. L. D. Kilcoyne, F. Koike, N. Kuze, D. S. Slaughter, and Y. Azuma, J. Phys. B: At., Mol. Opt. Phys. **48**, 115003 (2015).
[35]H. Aksela, M. Kivilompolo, E. Nõmmiste, and S. Aksela, Phys. Rev. Lett. **79**, 4970 (1997).
[36]O. M. Kvalheim, Chem. Phys. Lett. **86**, 159 (1982).
[37]J. H. D. Eland, P. Linusson, L. Hedin, E. Andersson, J.-E. Rubensson, and R. Feifel, Chem. Phys. Lett. **485**, 21 (2010).
[38]B. Siegmann, U. Werner, and R. Mann, Nucl. Instrum. Methods Phys. Res., Sect. B **233**, 182 (2005).
[39]S. Sheinerman, P. Lablanquie, F. Penent, Y. Hikosaka, T. Kaneyasu, E. Shigemasa, and K. Ito, J. Phys. B: At., Mol. Opt. Phys. **43**, 115001 (2010).
[40]G. B. Armen, J. Phys. B: At., Mol. Opt. Phys. **29**, 677 (1996).
[41]T. Hayaishi, E. Murakami, Y. Morioka, E. Shigemasa, A. Yagishita, and F. Koike, J. Phys. B: At., Mol. Opt. Phys. **28**, 1411 (1995).
[42]J. Viefhaus, S. Cvejanović, B. Langer, T. Lischke, G. Prümper, D. Rolles, A. V. Golovin, A. N. Grum-Grzhimailo, N. Kabachnik, and U. Becker, Phys Rev Lett **92**, 083001 (2004).

# Paper V

**Preparing the MAX IV Storage Rings for Timing–based Experiments**

Christian Stråhlman, Teresia Olsson, Simon C. Leemann, Rami Sankari, Stacey L. Sörensen.

*AIP Conference Series* **in press**, (2016).

# Preparing the MAX IV Storage Rings for Timing-based Experiments

C. Stråhlman[1,a)], T. Olsson[1,b)], S. C. Leemann[1], R. Sankari[1] and S. L. Sorensen[2]

[1]*MAX IV Laboratory, Lund University, P.O. Box 118, 221 00 Lund, Sweden.*
[2]*Department of Physics, Lund University, P.O. Box 118, 221 00 Lund, Sweden.*

[a)]Corresponding author: Christian.Strahlman@maxlab.lu.se
[b)]Corresponding author: Teresia.Olsson@maxlab.lu.se

**Abstract.** Time-resolved experimental techniques are increasingly abundant at storage ring facilities. Recent developments in accelerator technology and beamline instrumentation allow for simultaneous operation of high-intensity and timing-based experiments. The MAX IV facility is a state-of-the-art synchrotron light source in Lund, Sweden, that will come into operation in 2016. As many storage ring facilities are pursuing upgrade programs employing strong-focusing multibend achromats and passive harmonic cavities (HCs) in high-current operation, it is of broad interest to study the accelerator and instrumentation developments required to enable timing-based experiments at such machines. In particular, the use of hybrid filling modes combined with pulse picking by resonant excitation or pseudo single bunch has shown promising results. These methods can be combined with novel beamline instrumentation, such as choppers and instrument gating. In this paper we discuss how these techniques can be implemented and employed at MAX IV.

## INTRODUCTION

The MAX IV facility consists of a linac and two storage rings (operated at 1.5 GeV and 3 GeV). The linac serves as an injector to the rings and to a short pulse facility (SPF) [1]. Since the completion of the MAX IV Detailed Design Report [2], a discussion on timing modes has been initiated by the user community. Several research areas have been identified where users would benefit from other repetition rates and/or pulse lengths than the ones available in the MAX IV baseline design [3]. While there is no established timing user community at the current MAX I-III rings, several users from Nordic countries perform such experiments at other facilities. These cases include pump-probe techniques for imaging and spectroscopy, application of novel instrumentation for electron and ion time-of-flight spectroscopy, and studies of slow relaxation processes. The demands span several energy ranges and repetition rates. Evidently, no individual proposed timing solution would satisfy all user cases. However, we have concluded that a more urgent and wider interest exists for modification of the photon repetition rate provided by the MAX IV storage rings than for shorter photon pulses, especially since the facility already includes the SPF. Our current priority is therefore to identify methods and techniques to broaden the repetition rates at the MAX IV storage rings.

The 1.5 GeV storage ring is aimed towards producing VUV and soft X-rays. The ring has a circumference of 96 m and employs a double-bend achromat lattice to produce an emittance of 6 nm rad. The 3 GeV storage ring on the other hand is aimed towards ultralow emittance to generate high brilliance hard X-rays. The design of the 3 GeV storage ring includes many novel technologies such as a multibend achromat lattice and a compact, fully-integrated magnet design. This results in a circumference of 528 m and an emittance as low as 0.2 nm rad with insertions devices [4]. Both MAX IV storage rings have a 100 MHz main RF system, a design current of 500 mA [5], and will be operated with a uniform, multibunch filling pattern with 5 nC per bunch [2]. Also, both rings employ harmonic cavities (HCs) [5] to damp instabilities and increase the Touschek lifetime by elongating the bunches [4]. For the 3 GeV ring the HCs are also essential for conserving the ultralow emittance at high bunch charge [6]. Simulations of collective effects for the 3 GeV ring have shown that sufficient bunch lengthening is of great importance to be able to achieve the design current of the machine [7]. The HCs operate in passive mode [4], hence the bunch lengthening depends on both the tuning of the cavities and the filling pattern of the machine.

For timing-based experiments, three temporal properties are of special interest: the repetition rate, the bunch interval and the bunch length. The requirements for these properties are dictated by the user needs for pulse separation and pulse length. The time structures of the MAX IV storage rings and SPF are displayed in Table 1. The repetition rates that can be achieved at the storage rings are four orders of magnitude greater than what can be achieved at the SPF. On the other hand, the pulse lengths produced at the SPF are three orders of magnitude shorter than the pulse lengths produced at the storage rings.

**TABLE 1.** Time structure for the MAX IV storage rings and SPF.

| | Single-bunch repetition rate [Revolution time] | Bunch interval | Bunch length (bare lattice at maximum main cavity voltage) |
|---|---|---|---|
| SPF | 100 Hz | $10^7$ ns | 0.1 ps (FWHM) |
| 1.5 GeV ring | 3.13 MHz [0.32 $\mu$s] | 10 ns | ~49 ps (RMS) (w/o HCs) to ~213 ps (RMS) (HCs) |
| 3 GeV ring | 0.57 MHz [1.76 $\mu$s] | 10 ns | ~29 ps (RMS) (w/o HCs) to ~165 ps (RMS) (HCs) |

## ACCELERATOR ISSUES

Many synchrotron radiation storage rings nowadays run with several filling patterns to be able to serve different user groups. We have initiated studies to evaluate the performance of our machines for other filling patterns than the uniform multibunch pattern specified in the MAX IV baseline design. Studies performed for other machines operating with passive HCs show that a gap in the filling pattern gives rise to transient beam loading effects that decrease the average bunch lengthening [8]. Considering the previously highlighted importance of the performance of the HCs for the operation of the MAX IV storage rings this could be a serious issue. An initial study of filling patterns with gaps for the MAX IV 3 GeV storage ring is displayed in Fig. 1. The studies were performed with a tracking code developed by Milas [9] using the model described in [8]. These studies show that the bunch lengthening caused by the passive HCs decreases when introducing a gap in the filling pattern. They also show that the effect is greater for longer gaps. It is therefore desirable to develop methods for timing-based experiments at the MAX IV storage rings that require a small, or preferably, no gap in the filling pattern.

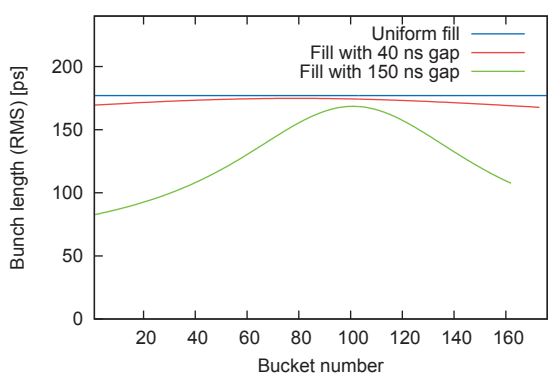


**FIGURE 1.** Bunch length for a uniform fill, a 40 ns gap and a 150 ns gap in the filling pattern for the MAX IV 3 GeV storage ring. The bunch current is 2.84 mA (5 nC) for all filling patterns. For the main cavities a total voltage of 1.4 MV maximizing the lifetime [6], a shunt impedance of $6 \times 1.715$ MOhm and a Q factor of 20400 were used [10]. The detuning of the main cavities was optimized for maximum bunch lengthening. For the HCs a Q factor of 20800 [10] and shunt impedance and detuning according to the flat potential conditions described in [8, 11] were used. Intrabeam scattering and the beam profile form factor have not been taken into account so far. The natural bunch length without bunch-lengthening HCs is 34 ps RMS. For a uniform fill, a bunch length of 177 ps RMS can be achieved by tuning the HCs, but for a gap of 40 ps the mean bunch length is reduced to 172 ps RMS and for a gap of 150 ps to 130 ps RMS.

Pulse picking by resonant excitation (PPRE) [12] and pseudo single bunch (PSB) [13] are two methods that have been developed to enable storage rings to serve both high-intensity experiments and timing-based experiments simultaneously. In PPRE the emittance of one bunch in the train is increased by excitation and an aperture in the beamline ensures that only light from the excited bunch is accepted. In PSB one bunch in the train is kicked onto another orbit for a few turns and the light from this bunch can then be separated by an aperture. In both methods, single-bunch light is created in one (or several) beamlines while all other beamlines receive multibunch light. The PSB method relies on the performance of the kicker magnet. At ALS a 40 ns 1 kV pulse at a maximum repetition rate of 1.5 MHz has been achieved so far [14]. The pulse length of the kicker sets the gap length requirement between the camshaft bunch and neighboring bunches.

## BEAMLINE INSTRUMENTATION

Choppers are another way to transmit only a single light pulse from a storage ring. If the chopper is used in hybrid filling mode, the opening time of the chopper has to be shorter than the gap in the filling pattern (hybrid window). For single-bunch operation and PPRE, the use of choppers is necessary if the single-bunch repetition rate needs to be further reduced. The high-speed chopper system at the ID09B beamline at ESRF [15] creates a 300 ns opening window with 3 kHz frequency. A chopper of this kind could possibly be implemented at the MAX IV 3 GeV ring, provided a sufficient hybrid window is available. Another solution is the MHz light chopper developed for use at BESSY II [16], which to this day is the only chopper providing individual light pulses with MHz repetition rate. At BESSY II, it can extract light from a single bunch residing in a 200 ns window with 1.25 MHz. General concerns with high-speed choppers are substantial mechanical complexity, high cost and the need to have a beamline with a suitable intermediate focus where the chopper can be placed. As tolerances are tight, the beam must be small at the point where the chopper is installed. A large beam reduces both transmission of the single pulse, and purity since neighboring pulses can leak through. Choppers are good solutions for facilities with a limited number of dedicated beamlines with strict temporal demands. In particular, this applies to beamlines which host instruments with pre-determined analysis rates (e.g. pulse lasers, TOF instruments and detectors with specified dead-times). The joint operation of PPRE or PSB and choppers can serve several purposes. Choppers can serve as background suppressors [17], but the combination can also further increase the versatility of the timing scheme.

Implementing gating schemes for X-ray detectors can enable timing-based experiments without choppers. Successful operation of a gating scheme has been reported at the 24-bunch filling mode at APS, with 153 ns bunch separation [18]. The gated PILATUS detector requires a bunch separation of at least 130 ns to ensure detection of a given X-ray pulse. The possibility of a gated electron detector in a time-of-flight-based electron spectrometer (ARTOF) has been studied in [19]. A weak pulsed electric field is introduced in front of the MCP and delay-line detector in the ARTOF spectrometer. When the instrument is used in the standard hybrid mode at BESSY II, only the electrons created by the camshaft bunch are resolvable and all other electrons have to be disregarded. The gate deflects unresolvable electrons and prevents them from saturating the detector. The required size of the gap in the filling pattern is dictated by the properties of the instrument, but can be approximated to 100 ns.

For some instruments, coincidence detection can solve timing needs. It has been shown how the ARTOF electron spectrometer can be used to achieve high transmission in a coincidence experiment, while retaining high energy resolution [20]. The detection of an electron in the hemispherical analyser is used as a start trigger for the ARTOF instrument. The measurement uncertainty is determined by the temporal dispersion of the detected electrons, which is ~6 ns for 200 eV pass energy [20]. This uncertainty accounts for half of the total temporal error. At a storage ring with 2 ns pulse separation it is not possible to eliminate this error by assigning electrons to specific light pulses. However, MAX IV makes this possible as the temporal broadening in the hemispherical analyser is less than 10 ns. In a recent experiment at the I411 beamline at MAX II we have verified that 10 ns pulse separation can indeed be used to reference electron detection to specific light pulses. The resolution of the coincident detection then equals the stand-alone resolution of the TOF instrument. It is suggested that the pass energy of the hemispherical analyser can be set below 20 eV before time dispersion exceeds 10 ns [21]. Put into practice, this electron coincidence scheme would provide the MAX IV storage rings with the highest resolution achievable at any storage ring in the world.

## CONCLUSIONS

Discussions with the user community reveal a broad interest from timing users for light with lower repetition rates than the baseline 100 MHz provided by the MAX IV storage rings, but several orders of magnitude higher than the 100 Hz provided by the SPF. Novel developments in accelerator technology and beamline instrumentation, such as hybrid modes in combination with PPRE, PSB, choppers and/or gated detectors, open new possibilities to host such timing-based experiments at MAX IV.

The 10 ns bunch interval of the MAX IV storage ring is an advantage when employing many of these methods since it relaxes parameters of the kickers and/or choppers, but also on the hybrid window. This implies the operation of timing modes might not have to compromise other parameters, such as the stored current. We believe that both PPRE and PSB are of great interest for MAX IV. For the PPRE method the 10 ns bunch interval should give sufficient separation to apply the excitation to one bunch within the multibunch train without a hybrid window. If the intensity of the individual PPRE photon pulse and the pulse length are acceptable, the technique can directly serve potential users. PSB would serve a wider range of timing users, but the method implies several technical challenges, e.g. implementation of a hybrid mode and kicker development. In the coming years, kicker performance is expected to increase since several machine upgrades include injections schemes that require ultrafast kickers. This is promising since it could make PSB achievable at MAX IV using only a small hybrid window or perhaps no window at all.

We aim to continue our work to present a science case and prepare the MAX IV storage rings for timing-based experiments. This work has to involve users as well as beamline and accelerator staff. As we have found many exciting and promising solutions to enable timing-based experiments at the MAX IV storage rings, we urge the community to pursue this discussion to ensure that timing-based experiments will also be present in future ultralow-emittance storage rings.

## REFERENCES


[1] M. Eriksson *et al.*, The MAX IV synchrotron light source, in *Proceedings of IPAC2011, San Sebastian, Spain*, p. THPC058, 2011.

[2] MAX IV Detailed Design Report, `http://www.maxlab.lu.se/maxlab/max4/DDR_public`, 2010.

[3] S. L. Sorensen, Timing modes at the MAX IV storage rings (report), `https://indico.maxlab.lu.se/event/60/material/0/0.pdf`, 2015.

[4] P. F. Tavares, S. C. Leemann, M. Sjöström, and Å. Andersson, J. Synchrotron Rad. **21**, 862 (2014).

[5] Å. Andersson *et al.*, The 100 MHz RF system for the MAX IV storage rings, in *Proceedings of IPAC2011, San Sebastian, Spain*, p. MOPC051, 2011.

[6] S. C. Leemann, Phys. Rev. ST Accel. Beams **17**, 050705 (2014).

[7] G. Skripka, P. F. Tavares, M. Klein, and R. Nagaoka, Transverse instabilities in the MAX IV 3 GeV ring, in *Proceedings of IPAC2014, Dresden, Germany*, p. TUPRI053, 2014.

[8] J. M. Byrd, S. De Santis, J. Jacob, and V. Serriere, Phys. Rev. ST Accel. Beams **5**, 092001 (2002).

[9] N. Milas and L. Stingelin, Impact of filling patterns on bunch length and lifetime at the SLS, in *Proceedings of IPAC2010, Kyoto, Japan*, p. THPE084, 2010.

[10] A. Andersson, Private communication, 2015.

[11] P. F. Tavares, A. Andersson, A. Hansson, and J. Breunlin, Phys. Rev. ST Accel. Beams **17**, 064401 (2014).

[12] K. Holldack *et al.*, Nat. Commun. **5**, 4010 (2014).

[13] C. Sun, G. Portmann, M. Hertlein, J. Kirz, and D. S. Robin, Phys. Rev. Lett. **109**, 264801 (2012).

[14] S. Kwiatkowski *et al.*, "Camshaft" bunch kicker design for the ALS storage ring, in *Proceedings of EPAC 2006, Edinburgh, Scotland*, p. THPLS114, 2006.

[15] M. Cammarata *et al.*, Rev. Sci. Instrum. **80**, 015101 (2009).

[16] D. F. Förster *et al.*, Opt. Lett. **40**, 2265 (2015).

[17] M. P. Hertlein *et al.*, J. Synchrotron Rad. **22**, 729 (2015).

[18] T. Ejdrup *et al.*, J. Synchrotron Rad. **16**, 387 (2009).

[19] R. Ovsyannikov *et al.*, Using detector gating to operate an ArTOF time–of–flight electron spectrometer in hybrid mode at storage ring SR-facilities, in *On the Challenges for Time-of-Flight Electron Spectroscopy at Storage Rings*, edited by C. Stråhlman, Licentiate Thesis, Lund University, 2014.

[20] C. Lupulescu *et al.*, J. Electron Spectrosc. Relat. Phenom. **191**, 104 (2013).

[21] O. Kugeler, S. Marburger, and U. Hergenhahn, Rev. Sci. Instrum. **74**, 3955 (2003).

# Paper VI

**Using Detector Gating to Operate an ArTOF Time-of-Flight Electron Spectrometer in Hybrid Mode at Storage Ring SR-Facilities**

Torsten Leitner, Christian Stråhlman, Ruslan Ovsyannikov, Patrik Karlsson, Måns Lundqvist, Mihaela Gorgoi, Rami Sankari, Svante Svensson, Nils Mårtensson, Alexander Föhlisch.

*submitted to Journal of Electron Spectroscopy and Related Phenomena*, (2015).

# PAPER VII

**Angle-resolved time-of-fight spectroscopy applied to multi-bunch operation at MAX-lab: a design study**

Christian Stråhlman, Rami Sankari, Måns Lundqvist, Gunnar Öhrwall, Ruslan Ovsyannikov, Svante Svensson, Nils Mårtensson, Ralf Nyholm.

*Journal of Physics: Conference Series* **425**, 092011 (2013).

11th International Conference on Synchrotron Radiation Instrumentation (SRI 2012) IOP Publishing
Journal of Physics: Conference Series **425** (2013) 092011 doi:10.1088/1742-6596/425/9/092011

# Angle-resolved time-of-flight spectroscopy applied to multi-bunch operation at MAX-lab: a design study

**C Stråhlman[1], R Sankari[1], M Lundqvist[2], G Öhrwall[1], R Ovsyannikov[3], S Svensson[3,4], N Mårtensson[4], R Nyholm[1]**

[1] MAX IV Laboratory, Lund University, P.O. Box 118, SE-22100 Lund, Sweden
[2] VG Scienta AB, P.O. Box 15120, SE-750 15 Uppsala, Sweden
[3] Helmholtz–Zentrum Berlin, Albert-Einstein-Straße 15, D-12489 Berlin, Germany
[4] Dept. of Physics and Astronomy, Uppsala University, P.O. Box 521, SE-75121 Uppsala, Sweden

E-mail: Christian.Strahlman@maxlab.lu.se

**Abstract.** Angle-resolved time-of-flight (ARTOF) spectrometers have found use in a number of applications, including ARPES. However, the fundamental requirement of an external start trigger matching the read-out time of the instrument limits its usability at many storage rings. Hitherto all reported experiments have been performed at storage rings capable of running in single-bunch mode. To eliminate this restriction, we propose a method where a pulsed electronic gate is introduced to allow for ARTOF usage at normal multi-bunch operation of the MAX II storage ring. This paper will show the working principle and outline the design for this technique.

## 1. Introduction

Angular resolved photoelectron spectroscopy (ARPES) has become a powerful tool in many applications. In the field of band–mapping of materials, the technique has had particular impact. The dominating instrument for such experiments has been the hemispherical deflector electron energy analyzer (HDA). Recent development of electron time-of-flight (TOF) type analyzers have made them cover ground in this area [1]. Both types have proven high energy resolution, thus allowing detailed studies of electronic structure. A significant trend has been the extension to simultaneous measurements of all momentum components of the electron, via the energy and angular distribution. In this spirit, a new energy and angle resolving electron spectrometer, the Scienta ARTOF 10k, has been recently developed based on angle-resolved electron time-of-flight (ARTOF) [2]. The principles behind this detection system have been described in detail by Wannberg [1]. The ARTOF spectrometer consists of a many-element electron lens and a position–sensitive detector. With the aid of simulations, the lens can be set up so that each combination of TOF and hit position can be determined to correspond to a point in 3D momentum space.

ARTOF instruments have so far been designed to operate at pulsed sources of X-rays and VUV–radiation with a pulse frequency in the order of 1 MHz, corresponding to 1 $\mu$s spacing between light pulses. This prerequisite poses a fundamental restriction compared to the HDA, namely that the start trigger must be external [1]. So far the use of electron TOF at synchrotrons has been restricted to facilities with single–bunch operation. Still, multi–bunch operation

 

11th International Conference on Synchrotron Radiation Instrumentation (SRI 2012) IOP Publishing
Journal of Physics: Conference Series **425** (2013) 092011 doi:10.1088/1742-6596/425/9/092011

is far more common at synchrotron radiation facilities, as most users exploit the light as a high intensity quasi-continuous beam. Following demands for time resolved experiments, some facilities are able to operate in more exotic modes, such as single–bunch and hybrid modes (see e.g. BESSY II [3]). The availability of single–bunch operations is however quite limited. To enable for increased use of TOF-based techniques, it is necessary to develop a method where the ARTOF spectrometer can be used under normal multi–bunch operation. The most common approach to decrease the undesired repetition rates in storage rings has been mechanical choppers which filter out a certain fraction of the light pulses (see e.g. [4]). However, no chopping setup has been fast enough to filter out single pulses from the multi–bunch light pulse pattern.

We propose instead a method where an electronic gate is implemented to protect the spectrometer from undesired electrons. The setup should allow for the electrons originating from one single light pulse to reach the spectrometer and propagate undisturbed to the spectrometer detector. All other electrons should be deflected. In the following we shall show that an electronic gate can mimic single–bunch temporal structure under normal multi–bunch operation.

## 2. 100 MHz multi–bunch operation at MAX II

The MAX II storage ring has been in operation since 1997. Since 2002, it has operated on a 100 MHz RF system [5]. The filling pattern of MAX II today is homogeneous with equal and equidistant electron bunches (10 ns). The 100 MHz concept has been preserved for the new MAX IV synchrotron light facility, which is now been built in Lund, Sweden. The MAX IV project will utilize a time structure in normal operation equal to that of MAX II [6]. The operating frequency of MAX II (and MAX IV) provides us with an advantage compared to storage rings with 500 MHz RF systems since we have a relatively long 10 ns intermediate time between light pulses.

## 3. Design considerations

The conceptual design of our gate is showed in Fig. 1. In simulations we have used the ARTOF 10k [2] as a reference instrument, although the principle stands for all electron spectrometers with timing constraints. For this spectrometer, the focal distance of the lens is 40 mm. Our proposed gate consists of two consecutive high transmission meshes placed in front of the first lens element. A sufficient negative potential is applied to the mesh closest to the sample. The purpose of this gating potential is to deflect all electrons away from the lens when the gate is 'closed'. Simulations performed with the SIMION software [7] predict a required gating potential given by $V_{\mathrm{gate}}[\mathrm{V}] = 1.3 \cdot E_{\mathrm{elec,max}}[\mathrm{eV}]$, where $E_{\mathrm{elec,max}}$ is the highest expected electron kinetic energy. The second mesh, which is grounded, has two functions: Firstly, it protects the spectrometer from the gating potential, whereas otherwise the gating potential would leak into the lens and disturb the focus. Secondly, as shall be shown, it increases the available ramp-up time of the gating potential. When the gate is closed, no electrons from the interaction region are able to reach the spectrometer. To open the gate, the potential is reduced to zero, thus allowing for undisturbed passage of electrons.

The optimal timing scheme of the gate depends heavily on the electron energy to be measured. With the 100 MHz pulsing of light, energetic electrons are ejected from the sample every 10 ns. The distance traveled by a non-relativistic electron in free space is given by the equation $d[\mathrm{mm}] = 0.59 \cdot t[\mathrm{ns}] \cdot \sqrt{E_{\mathrm{elec}}[\mathrm{eV}]}$. Fig. 2 show the restrictions on gate timing. The maximum fall time equals the pulse separation 10 ns, while the rise time depend mainly on the energies of the electrons. Fast electrons (>100 eV) will pass the gate quickly and the available rise time is 9 ns. For 10 eV electrons, the required passing time is longer and available rise time is reduced to 7 ns. Hence, spectroscopy with low electron energies put a tougher constraint on the rise time than higher energies. At the same time, lower electron energies require lower shielding potential, which is easier to reach in shorter time.

11th International Conference on Synchrotron Radiation Instrumentation (SRI 2012) IOP Publishing
Journal of Physics: Conference Series **425** (2013) 092011 doi:10.1088/1742-6596/425/9/092011

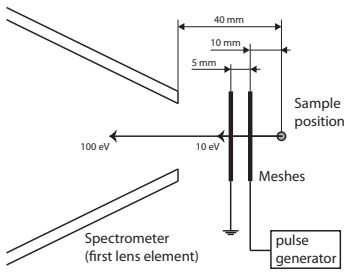


**Figure 1.** The conceptual design of the electronic gate for ARTOF 10k focusing conditions. The mesh closest to the sample is fed by fast pulse generation. The second mesh shields the entrance to the spectrometer from the gating potential. We have indicated the distance traveled by a 10 eV and a 100 eV electron in 10 ns.

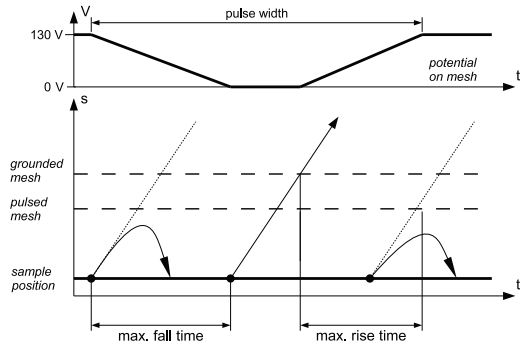


**Figure 2.** Timing principle for the gate in a 2D time-space-diagram together with required gating potential. The tilted lines indicate propagation of mono-energetic electrons through the gate. The first and third electron should be deflected, while the second should pass the gate. Mesh potential is given for 100 eV electrons.

There is a practical lower limit for the electron energies which can be gated. Below 10 eV, temporal overlapping of adjacent electron bursts start to become an issue. For MAX II standard operation the practical lower limit should thus be slightly below 10 eV. One should in this case make use of the ARTOF 10k low energy cut-off, which will filter out low-energy electrons and any secondary electron which would reside in the chamber [2].

In present simulations the gating meshes are separated by 5mm, whereas the pulsed mesh is placed 10 mm from the sample. It is preferential to put the gate as close to the sample as possible. The first reason for this is that a wider energy range of electrons is allowed, since the time separation of electrons are smaller. This is particularly relevant for low energy electrons. The second reason is that the usability of electron spectrometers, and particular ARTOF spectrometers, fully relies on our ability to predict the electron trajectories through the lens. The inclusion of the second mesh constitutes a disturbance to the lens focus which decreases with increasing distance.

## 4. Pulse generation

The use of pulse generators to gate electrons and ions is very common in spectroscopy. However, they are normally operated in the kHz regime. Here, we should operate in 1 MHz frequency, addressing the dead time of the ARTOF (1 $\mu$s), required fall and rise times and the overall pulse width (Fig. 2). To maintain good focus of the lens, it is necessary to avoid disturbances from the gating mesh while the gate is open. Ideally, we would have a zero gating potential during the time the electron passes. The signal from the system must thus be sufficiently free from ringing.

High demands are put on the electronic switches. Switches with rise/fall-times down to a few ns sustaining 1 kV and 1 MHz repetition rate are commercially available (see e.g. [8]). The difficulty is to find a device which can provide pulse lengths <20 ns, which is a demand of our setup. We have therefore explored a solution where two parallel switches are deployed, as seen in Fig. 3. Each switch is set up to provide a pulse every 2 $\mu$s. This frequency is

11th International Conference on Synchrotron Radiation Instrumentation (SRI 2012) IOP Publishing
Journal of Physics: Conference Series **425** (2013) 092011 doi:10.1088/1742-6596/425/9/092011

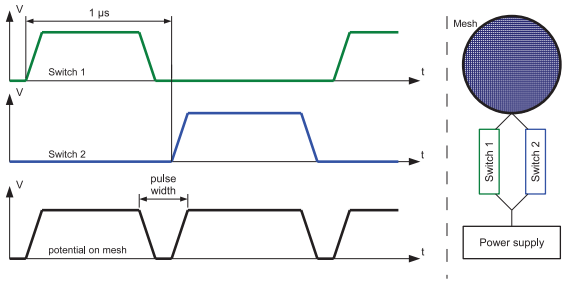


**Figure 3.** Two parallel switches feed the pulser mesh. Each blocking pulse is started by an external trigger determined by the ring frequency. The pulse is set to end after a predetermined time, just before the start of the next blocking pulse. (Graphs are not to scale.)

synchronized to the frequency of the light pulses, which can be extracted with a photo-diode in the experimental chamber, or obtained from a bunch marker from the ring. The switch is set up to close after a predetermined time just long enough to create the <20 ns time-window needed for the application. With this solution, a short time-window can be created without reducing the pulse length of the switch.

Our calculations have shown that the capacitance of the system can be kept below 10 pF when short wiring is utilized. Considering a maximum 500 V gating potential achieved in 3 ns, the peak current is 2 A, which can be well transferred by available feedthroughs. Considerations must also be given to the potential fall of the device to minimize ringing during the time which the gate is open. The length of the blocking pulse must be defined within a few ns margin of error.

## 5. Conclusions

We have in this paper shown how an electronic gate can be constructed to allow for time-resolving spectrometers to be used at multi-bunch storage rings. We have discussed how one can mimic single-bunch operation not only by chopping light, but also by blocking ejected electrons from reaching the spectrometer. A setup with a mesh with an applied pulsed blocking potential, in conjunction with a second shielding mesh, have been studied in electrostatic simulations. We have further suggested an electronic setup with two fast switches to overcome inherent restrictions in terms of achieving very short electronic pulses.

## References

[1] B. Wannberg, Nucl. Instrum. Methods Phys. Res. A **601**, 182 (2009).
[2] G. Öhrwall *et al.*, J. Electron Spectrosc. Relat. Phenom. **183**, 125 (2011).
[3] *Operating Modi BESSY II* (`http://www.helmholtz-berlin.de/forschung/grossgeraete/betrieb-beschleuniger/betriebsmodi_en.html`).
[4] S. Plogmaker *et al.*, Rev. Sci. Instrum. **83**, 013115 (2012).
[5] Å. Andersson, M. Bergqvist, M. Eriksson, L. Malmgren, and L. Thånell, The 100 mhz rf system for max-ii and max-iii, in *Proceedings of the 8th European Particle Accelerator Conference*, pp. 2118–2120, European Physical Society Interdivisional Group on Accelerators (EPS-IGA) and CERN, 2002.
[6] *Detailed Design Report on the MAX IV Facility*, 1 ed. (`https://www.maxlab.lu.se/node/1136`, 2012).
[7] `http://simion.com/`.
[8] *BEHLKE FSWP 51-02 product sheet* (`http://www.behlke.com/pdf/fswp%2091-01_rs.pdf`, 2012-11-27).